LIQUID CELL ELECTRON MICROSCOPY

MICROCELL FABRICATION AND RESOLUTION ENHANCEMENT
FOR
IN SITU LIQUID CELL ELECTRON MICROSCOPY

By

ERIC DAIGLE, B.Eng.

A Thesis Submitted to the School of Graduate Studies
in Partial Fulfilment of the Requirements
for the Degree Master of Applied Science

McMaster University
© Copyright by Eric Daigle, January 2019

MASTER OF APPLIED SCIENCE (2019)
(Materials Science and Engineering)

MCMASTER UNIVERSITY
Hamilton, Ontario, Canada

TITLE: Microcell fabrication and resolution enhancement for *in situ* liquid cell electron microscopy

AUTHOR: Eric Daigle, B.Eng.

SUPERVISOR: Dr. Gianluigi A. Botton and Dr. Leyla Soleymani

NUMBER OF PAGES: Xii, 126

Lay Abstract

Characterization of nanomaterials has been available for several decades and has aided in the improvement of material design, such as steel strength and corrosion resistance, electrical systems such as those involved in computers and smartphones, and biological sensing and detection. Observation of dynamic process which occur at the interface between solid and liquid phases, or purely within liquid layers, has always been a challenging topic due to the difficulty of finding a stable environment for both solids and liquids to exist at the nano scale within a measurement device. *In situ* liquid cell electron microscopy offers the ability to image this interface with real-time data acquisition for recording of dynamics and kinetics at the nano scale. Previous work has shown the liquid cell to provide high spatial and temporal resolution of systems in an environment which mimics their native operating conditions.

This thesis addresses current developments for *in situ* systems and works to develop a custom liquid cell to further the applications of the liquid cell and provide improved control over experimental conditions. The work then aims to improve on current technology by increasing the spatial resolution obtainable. Finally, the technique is applied to study the structural changes of nanocrystals under various etching conditions as a demonstration of its' capabilities.

Abstract

Liquid cell electron microscopy has been proven to provide high spatial and temporal resolution for studying liquid layers and the solid-liquid interface at the micro and nano scale. The *in situ* environment allows for spatial and spectral characterization and quantification of the dynamics and kinetics involved with structural and chemical changes of nanostructures, which has seen application is fields of materials science, electrochemistry, corrosion, biomaterials, and nanophysics. The rapid growth of *in situ* liquid cell electron microscopy has motivated the fabrication of a custom liquid cell for improved control over the experimental conditions, including cell dimensions and materials. In this work, the process flow and micro-fabrication of a custom liquid cell system are proposed and executed, with proof of operation through the *in situ* imaging of suspended gold nanoparticles and electrochemical characterization. The *in situ* TEM system is improved upon by forming 1μm diameter holes through the viewing membranes, removing the background noise contribution from imaging electrons through the windows. This allows for high resolution liquid cell imaging. This improved system is used to study the oxidative etching conditions for palladium nanocrystals, which are commonly used as catalysis for hydrogen fuel cells. The dendritic etching is studied through native etching under exposure to hydrochloric acid without the presence of oxidizing species, followed by the radiolytic generation of oxidizing radicals via the microscope electron beam, and finally by the application of electrical biasing.

Acknowledgments

I would like to thank my supervisors Dr. Gianluigi Botton and Dr. Leyla Soleymani for their constant enthusiasm and mentorship through this project. They have shown me the world of academia and inspired my work from the first day they introduced me to nanotechnology. They have supported all my ideas and experiments while guiding this project and research.

Much of this work would not have been possible without the training and troubleshooting provided by Doris Stevanovic for cleanroom processing, Shahram Tavakoli for plasma etching and physical sputtering, and Dr. Carmen Andrei for training and operation of the many TEMs available at McMaster. All three of you and sat through countless experiments and questions with nothing but enthusiasm and help for my research, and for that you have my sincere gratitude.

Thank you to the Canadian Centre for Electron Microscopy for providing a high-end facility for scientific research, with special mention to Andy Duft for his constant maintenance and patience with my questions, and Travis Casagrande for his operation of the FIB.

Thank you to both of my research groups for making this project as fun as it can be, through jokes told in the labs and life philosophy debates at weekly tea times, it has been a blast. A special thanks to Dr. Jie Yang for her expertise with the liquid cell system and to Alex Profelski and Isobel Bicket for their expertise on electron microscopy. Thank you to Viktor Kapetanovic and Yuting Chan for being amazing housemates, lab partners, and office buddies.

I am grateful to my family for continuously reminding me that I am a nerd.

My final and biggest thanks is to Patricia Nguyen for emotional support, and caring for my mental and physical health through this work. I couldn't have done this without you.

Table of Contents

Lay Abstract ... iv
Abstract ... v
Acknowledgments ... vi
Table of Contents ... vii
List of Figures and Tables ... ix
List of Abbreviations ... xi
Declaration of Academic Achievement ... xii

1 Introduction ... 1
1.1 Introduction ... 1
1.2 Background ... 2
1.2.1 Characterization of liquid media at the micro and nanoscale ... 2
1.2.2 Liquids in electron microscopy ... 3
1.2.3 Liquid cell electron microscopy ... 5
1.3 Objective of thesis ... 8
1.4 Motivation ... 9
1.5 Thesis overview ... 10

2 Background ... 11
2.1 Chapter introduction ... 11
2.2 Electron Microscopy ... 11
2.2.1 Microscopy – what is it ... 11
2.2.2 Imaging with electrons ... 13
2.3 Liquid cell electron microscopy: electron-sample interactions ... 14
2.3.1 Image formation: Theory of spatial resolution ... 14
2.3.2 Electron-water interactions and solution chemistry ... 20
2.4 Liquid cell electron microscopy: putting liquids in a vacuum ... 24
2.4.1 Alternative liquid cell designs and systems ... 24
2.4.2 Window bulging ... 27
2.4.3 Applications for the liquid cell ... 29
2.4.4 The holey liquid cell ... 33
2.5 Microfabrication ... 41
2.5.1 Photolithography ... 42
2.5.2 Wet chemical etching ... 48
2.5.3 Wet etching of Silicon ... 52
2.5.4 Dry chemical etching ... 56
2.5.5 Growth and deposition methods ... 59
2.5.6 Bulk processing: wafer cleaving ... 64
2.6 Focused Ion Beam ... 65
2.7 Electrochemistry ... 67
2.7.1 Basics: 2 and 3 electrode systems ... 67
2.7.2 Physical methods: CA and CV ... 68

2.7.3 Physical Electrochemistry: Electrode Specifications 71
2.8 Chapter conclusions 74

3 Experimental Methods 75
3.1 Chapter introduction 75
3.2 Fabrication process flow 75
3.2.1 Windows 75
3.2.2 Electrodes 81
3.2.3 Multi-material electrodes 84
3.2.4 Isolation layer 85
3.2.5 Wafer Cleaving 87
3.2.6 Final process flow 88
3.2.7 Microfabrication characterization methods 89
3.3 In situ experiments 90
3.3.1 FIB samples 90
3.3.2 Electrodeposition of Pd structures 91
3.3.3 Beam induced etching of Pd 91
3.3.4 Imaging of gold nanoparticles 92
3.4 Chapter conclusions 93

4 Results and discussion 94
4.1 Custom liquid cell fabrication 94
4.1.1 Microfabrication 94
4.1.2 Characterization 101
4.2 Resolution improvement via in situ study of oxidative palladium etching 105
4.3 Chapter Conclusions 112

5 Conclusions 113
5.1 Thesis summary 113
5.2 Thesis conclusion 114
5.3 Contribution to the field 115
5.4 Future work 115

6 References 117

7 Appendix: MEMS Processing 124

List of Figures and Tables

Figures

Figure 1-1 Schematic of first and second closed liquid cell,. 6
Figure 2-1 Simplified ray diagrams of microscopes 12
Figure 2-2 2D Airy disk patterns. 13
Figure 2-3 Relationship between electron dose and maximum resolution for LCEM 18
Figure 2-4 The resolution as a function of liquid layer thickness 19
Figure 2-5 LCEM spatial resolution dependence on liquid layer thickness 20
Figure 2-6 Three stages of water radioloysis, and dominant reactions in each stage 21
Figure 2-7 Concept design of a microwell liquid cell system. 26
Figure 2-8 Membrane bulging as a function of membrane width 28
Figure 2-9 Evaporative cooling from the surface of the aperature 39
Figure 2-10 Process flow for photolithography 42
Figure 2-11 Force balance during spin coating, and edge bead removal. 45
Figure 2-12 (Left) Contact-mask exposure. (Right) Proximity- mask exposure 46
Figure 2-13 Anisotropic vs isotropic etching 49
Figure 2-14 Chemical structure and suface binding for OH based etching of Si crystal planes. . 52
Figure 2-15 Crystal plane wet etching of Si 53
Figure 2-16 Concentration profiles during various stages of a CV cycle 71
Figure 3-1 Si etching and masking options 76
Figure 3-2 Window fabrication process flow 78
Figure 3-3 Mask design for windows in liquid cell chips 78
Figure 3-4 Reflux lid for KOH etching 80
Figure 3-5 Initial electrode design 82
Figure 3-6 Showing final layout of mask for electrodes 82
Figure 3-7 Electrode masks for replacing the working electrode 84
Figure 3-8 Film thickness curves for SU-8 3000 series and 2000 series 86
Figure 3-9 Mask design for isolation layer 87
Figure 3-10 Complete fabrication process flow. See text for annotations for A-E 88
Figure 3-11 Cross section view of the fabricated device 89

Figure 4-1 Light microscopy image of SiN wafer after 1 min RIE 95
Figure 4-2 KOH etch rate over time 95
Figure 4-3 Post- KOH etching of several SiN windows 96
Figure 4-4 Lithographic patterning and etching of electrodes. 97
Figure 4-5 Diulted SU-8 3005 resist as an isolation layer. 98
Figure 4-6 Fabrication of isolation layer from SU-8. 99
Figure 4-7 Laser and physical cleaving of individual chips from the bulk wafer. 100
Figure 4-8 Light microscope images of fabrication of a carbon working electrodes 101
Figure 4-9 In situ TEM images of 12 nm gold nanoparticles 102
Figure 4-10 Time tracking showing the motion of particles.. 103
Figure 4-11 CV scans in 2mM RuHex solution and 100mM KCl. 104
Figure 4-12 Peak currents vs scan rate for in situ CV using carbon working electrodes 105
Figure 4-13 Custom electrodes shown pre- and post- electrochemical cleaning....................... 105
Figure 4-14 SEM images of palladium dendrites electrodeposited *ex situ* on gold electrodes .. 106
Figure 4-15 FIB hole geometries 107
Figure 4-16 SEM Images of palladium dendrites around the FIB milled holes 107
Figure 4-17 In situ STEM imaging and oxidative etching of palladium dendrites 109
Figure 4-18 Post-situ SEM images of the palladium dendrites. 111

Tables

Table 2-1 Solution chemistry and electron beam effects on LCEM. 23
Table 2-2 Etch rates in nm/hr for various etchants. 51
Table 2-3 Approximate etch rate selectivities for common Si etchants. 53
Table 2-4 Typical deposition methods of common micorfrabrication materials......................... 63

List of Abbreviations

ADF	Annular Dark Field Detector
AFM	Atomic Force Microscopy
AMI	Acetone/ Methanol/ Isopropanol
APCVD	Atmospheric Pressure Chemical Vapour Deposition
CA	Chronoamperometry
CCEM	Canadian Centre for Electron Microscopy
CE	Counter Electrode
CEDT	Centre for Emerging Device Technologies
CV	Cyclic Voltammetry
EDX, EDS	Energy Dispersive X-ray Spectroscopy
EELS	Electron Energy Loss Spectroscopy
EM	Electron Microscopy
FIB	Focused Ion Beam
IPA	Isopropanol
LCEM	Liquid Cell Electron Microscopy
LPCVD	Low Pressure Chemical Vapour Deposition
MEMS	Micro- Electro- Mechanical Systems
PECVD	Plasma Enhanced Chemical Vapor Deposition
PL	Photolithography
PR	Photoresist
RE	Reference Electrode
RIE	Reactive Ion Etching
RuHex	Hexammineruthinnium (III) chloride
SEM	Scanning Electron Microscopy
SIMS	Secondary Ion Mass Spectrometry
STEM	Scanning Transmission Electron Microscopy
TEM	Transmission Electron Microscopy
WE	Working Electrode

Declaration of Academic Achievement

The author is the first author and main contributor of the written work included in this thesis with consultation from Dr. Gianluigi A. Botton and Dr. Leyla Soleymani.

In situ experimentation was aided by Carmen M. Andrei for TEM imaging, and Jie Yang for operation of the liquid cell holder. SEM imaging was performed by Yuting Chan. FIB operation was performed by Travis Casagrande.

1 Introduction

1.1 Introduction

In elementary chemistry classes, a simple galvanic electrochemical cell is often presented containing a metal anode and cathode electrically connected and placed in an electrolytic solution. Through electrochemical oxidation and reduction, metal ions are deposited onto the cathode, while simultaneously being stripped from the anode due to the flow of charges from an external source. Although this experiment may seem simple, it is interesting to note that until very recently[1] it has been impossible to directly observe this process. Observation of this experiment at the nanoscale is considered an '*in situ*', or 'in place' experiment, where a characterization technique is applied throughout the duration of the experiment, in its' native environment.

In all fields of research, one of the most important and complicated processes is the design of experiments that show the *in situ* operation of a system, in contrast to an experiment characterized at the beginning and end of operation, where the dynamics that occur in the middle are lost.

This is especially true for characterization of dynamics and kinetics which happen within soft matter at the micro and nano scale. One of the prime nano scale characterization techniques, electron microscopy, provides chemical and structural information from the millimeter to the atomic scale. For both Scanning Electron Microscopy (SEM) and Transmission Electron Microscopy (TEM), the samples must be solid objects which are stable under the vacuum of the microscope. Returning to the above example, electron microscopes are not compatible with the liquid samples required for electrochemistry and many other fields of research.

Since the invention of the TEM, it has been known that imaging and characterization of liquid systems would be challenging. The solution to this problem was immediately proposed, although the technology required for its application took time to catch up. Using microfabrication techniques, a thin microfluidic channel is constructed separating the high vapor pressure liquids from the vacuum environment of the microscope. The microfluidic channel required very thin membranes to allow the transmission of electrons through the system with reasonable resolution. This approach, named '*in situ* liquid cell electron microscopy', or often simply 'liquid cell electron microscopy' (LCEM) has since been refined and applied to the fields of corrosion, physical electrochemistry, bubble physics, radiation, biology, and much more.

LCEM not only provides a characterization tool for micro and nanoscale effects, it is a new experimental approach to studying physics at the nanoscale by providing a platform which records the dynamics of electron interaction with aqueous media. The high energy electrons from the electron microscope generate radiolytic species within the liquid, providing a new means to study radiation and electron induced interactions.

1.2 Background

In this background section, a general overview of the development of *in situ* characterization methods from the micro to nano scale is briefly addressed, starting with more classical approaches of recording dynamic changes within liquids and volatile media, followed by a discussion of techniques used within electron microscopes to image and characterize liquids. Finally, the development and scope of the *in situ* liquid cell electron microscopy technique is presented.

1.2.1 Characterization of liquid media at the micro and nanoscale

In all fields of study, characterization of dynamic processes without sacrificing the native operating environment of the processes is a significant challenge, and liquid media chemical reactions are no different. Classically, dynamic processes within liquids are characterized using optical spectroscopic approaches such as X-ray dispersive spectroscopy, X-ray diffraction, surface enhanced Raman spectroscopy, X-ray photoelectron spectroscopy and many others. Microscopy approaches including optical microscopy, fluorescent imaging, and scanning probe microscopy may be used, and more recently electron microscopy techniques have been applied. A major problem with these approaches is that the dynamic chemical processes typically occur in an incompatible environment to the characterisation platform, which is circumvented by 'pausing' the chemical reaction at various stages of development through drying or freezing, followed by characterization of each stage.

The freeze-drying approach has shown significant advances in chemistry, biology, and other related fields but it has many limitations: the process of freeze drying may alter the state of the reaction, yielding characterization of a unrepresentative state; fast dynamics may be difficult to capture due to a time delay with the freezing process; further sample preparation of each frozen stage may damage the samples, such as oxygen corrosion or surface etching from sample cleaning; and finally, the variability of the samples. Since it is not a single sample being studied through all phases of the reaction, sample variability plays a significant role in the uncertainty of the results.

Through these limitations researchers have developed *in situ* approaches using many of the same instruments, along with several other approaches. The term *in situ* is Latin for 'in place' in 'in position' and is used to refer to experiments where the dynamics occur inside the characterization system, allowing continuous temporal and spatial data to be collected. The simplest approach to this would be *in situ* optical microscopy; however, due to the large wavelengths of visible and x-ray imaging, spatial resolution is limited to 100 nm or larger, as further discussed in chapter 2.

Scanning Probe Microscopy (SPM) methods such as Atomic Force Microscopy (AFM) and Scanning Tunnelling Microscopy (STM) have achieved atomic level resolution and atomic level *in situ* characterization[2–5] of dynamic processes; however, they are serial techniques. A probe must traverse across the substrate to record information, resulting in a trade off between spatial resolution, temporal resolution, and field of view. For reference, in air the practical lateral scanning speed of an AFM is limited to 0.1 μ/s[6]. Scanning an area 100x100 μm would take approximately 10 minutes on a standard instrument, significantly slower than chemical dynamics. Surface-liquid interfaces are regularly studied to determine structural change with no information acquired of chemical compositions and phase changes. Additionally, suspended species such as nanoparticles cannot be studied, and the probe may interact with the systems altering the results. To this end, electron microscopy techniques were applied to improve the ratio of temporal to spatial resolution obtainable and to provide x-ray and electron spectroscopic information for determining chemical compositions and phases, allowing for a wider array of applications.

1.2.2 Liquids in electron microscopy

Electron microscopy (EM) is generally broken into three types, Scanning Electron Microscopy (SEM), Transmission Electron Microscopy (TEM), and Scanning TEM (STEM). Electron microscopes accelerate electrons to high velocity through high applied potential coils, and use a system of electromagnetic lenses to control an electron beam to interact with the sample. Electrons surpass the diffraction limitations of photons, with typical acceleration voltage between 1 kV-30 kV for SEM and 80-300 kV for TEM and STEM modes yielding a relativistic de Broglie wavelength of 1.9-40 pm. For the high energy electrons to be stable long enough to study the sample, the EM is under high vacuum (10^{-6} torr) during operation.

For SEM setups, the lower energy electrons interact with the sample surface where several interactions may occur: auger electrons caused by inner core electrons being knocked out of

position, a second valence electron replacing the inner core, and the transition energy ejecting an outer valence electron; secondary electrons which are inelastically knocked out from an outer valence shell; backscattered electrons which are caused by the primary electron beam elastically scattering back out of the sample; and x-rays which are generated from recombination effects after inner shell electrons are knocked out by the electron beam. Capturing each output from freeze dried samples yields structural and/or chemical and atomic information regarding the sample surface at superior spatial and spectral resolution to optical methods, but still suffers the same limitations imposed by freeze drying intermediate stages of a dynamic process.

TEM and STEM setups form images by transmitting the electrons through a sample 10-100 nm thick and projecting the transmitted electrons onto a screen or detector. Contrast is realized by either absorption, or inelastic and elastic electron scattering causing trajectory deflections to wide angles. Placing detectors to capture either the electrons scattered to high angles or the central non-scattered electrons provides Dark Field (DF) or Bright Field imaging modes, respectively. The electron sample interactions generate x-rays similarly to SEM providing spectral information in a technique known as Energy Dispersive X-ray Spectroscopy (EDX or EDS). Inelastic electron scattering reduces the energy of the primary electron beam by a characteristic amount to specific chemical phases, and detecting this loss is the principal of Electron Energy Loss Spectroscopy (EELS), yielding further spectroscopic information about the sample. As with SEM imaging, conventional TEM imaging is performed within a vacuum chamber, limiting its applications to thin, frozen or dried samples; however, TEM provides superior spatial, temporal and spectral information to SEM and optical methods.

The challenge of incorporating liquid phase materials into vacuum columns for SEM and TEM was approached in many ways. Some very low vapor pressure ionic liquids are stable within the microscope vacuum and may be studied directly, but the majority of applications require water as the primary solvent which has a high vapour pressure and readily evaporates. Environmental microscopes employ a differential pumping system to allow gas pressures typically below 3 kPa[7] to exist in a localized area to the sample, while maintaining high vacuum near the electron beam generation and optics. The vapour pressure of water is 2.3 kPa, allowing aqueous samples to be studied in an open system. Environmental systems are not without their disadvantages: the electron beam is partially absorbed and scattered by the vapours surrounding the sample, reducing the

Signal-to-Noise Ratio (SNR) at the detector and reducing the achievable spatial and spectral resolution in comparison to standard EM setups; gas vapours interact with the sample chamber, preventing use of corrosive gasses or solvents; solvents modify the vapor pressure of water, limiting the type and concentration of solvents available.

Another type of environmental system applicable to both gasses and liquids is an enclosed cell formed of ultra thin membranes, containing the volatile samples under pressure while isolating them from the EM vacuum. This system, referred to as Liquid Cell Electron Microscopy (LCEM), will be the focus of this thesis, and its development is explained in the following section.

1.2.3 Liquid cell electron microscopy

The first truly 'liquid cell' approach to incorporate liquids into electron microscopy was performed in 2003 by M. J. Williamson et al.[1] in the USA which employed two Si chips each coated with 100 nm of Si_3N_4, and selectively back etched to form two 100x100 µm free supported membranes, one per chip, as displayed in Figure 1-1. One chip was fashioned with a SiO_2 ring to act as a spacer, holding the two chips 0.5-1 µm apart from each other. The upper chip includes 2 large holes of millimeter scale, above which are placed glass slides 1 mm thick with an equal sized hole to the chip and sealed with heat curing epoxy. The depth of the glass slides act as a reservoir. One glass reservoir is filled with a solution of interest, which then fills the space between the chips through capillary action to the other reservoir. Both glass holes are then capped by a sapphire sheet and sealed with UV curing epoxy. To add to the functionality, the bottom chip was also fashioned with a thick Au electrode, which passes through a via to an external contact on the underside of the chip. A Au wire is placed inside one reservoir to act as a counter electrode, and a Cu wire in the other as a reference electrode.

Using this cell, the researchers only had access to two of the electrodes within the microscope due to the available TEM holders, however all three electrodes could be contacted *ex situ* to allow for electrochemical work. Using a 0.2 M $CuSO_4$ solution, Cu nanoparticles were galvanostatically deposited on the gold electrode while being observed by a 300 kV TEM providing a frame size of ~5 µm. Higher magnification achieved a maximum spatial resolution of 5 nm, which is limited by the thick gold electrode, Si_3N_4 windows, and bulk liquid thickness.

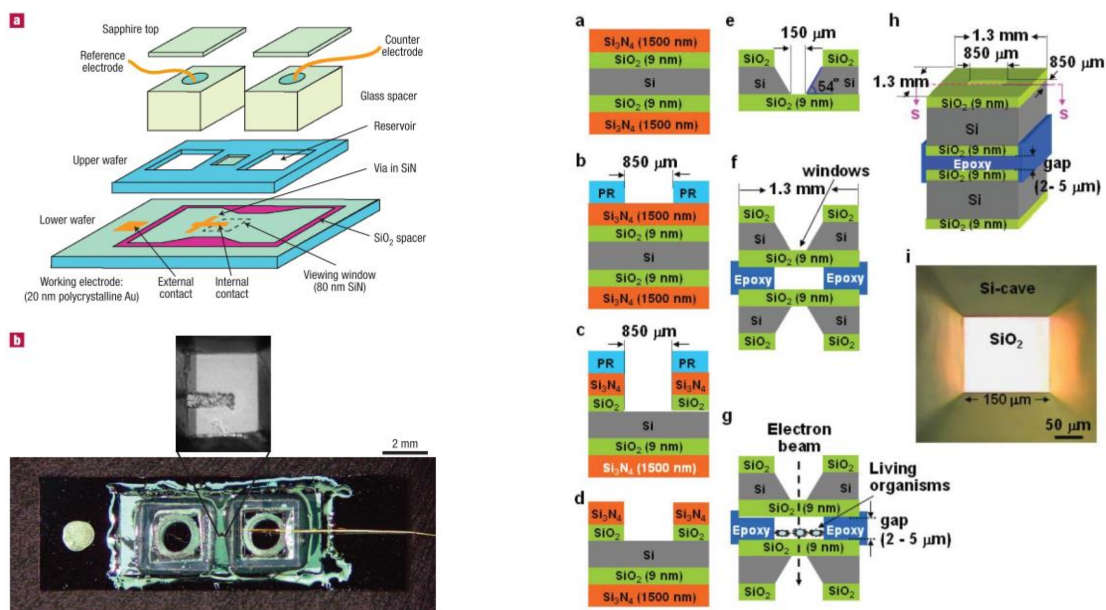

Figure 1-1 (Left) Image reproduced with permission from[1]. Schematic of first closed liquid cell, showing its fabrication in A, and an optical image of the working electrode on the electron transparent membranes and the assembled chip in B. (Right) Image reproduced with permission from[8]. The second closed microchip design, the K-kit, showing its construction from bulk Si, and SiO_2 and SiN_x thin films. (i) is an optical view of the cavity formed in bulk Si, with the free membrane illuminated.

Although this initial liquid cell design was very novel, it immediately showed potential for improvement and sparked a new field of research devoted to improvements of the technique. The most prominent concerns are: lack of access to the three electrodes within the microscope, allowing only galvanostatic (2 electrode) *in situ* work; and difficulty in assembly, due to many fabrication steps. This is a significant problem because the cell is single-use and must be individually reconstructed for each experiment. Other issues include: not utilizing common bulk micromanufacturing processes; impossibility of post-characterization of the internal cell and electrodes, including SEM studies of the deposited nanostructures; very poor resolution relative to that achievable from a modern (S)TEM; bulky reservoirs physically shield spectroscopic detectors; the reservoir limits total electrolyte volume, and there is no way to replace electrolytes around the working environment during long electrochemical experiments.

Despite these limitations, the researchers quantified the nucleation and growth dynamics of the electrodeposited copper nanstructures[9] and further studies of the growth kinetics of individual nanoclusters, showing detailed spatial and electrochemical data exploring two different regimes of short and long time growths[10].

After this initial cell, a second sealed liquid cell was not presented in literature until 2008 by Kuo-Liang Liu et al.[8] in Taiwan. As depicted in Figure 1-1, the K-kit followed a similar approach by

forming a thin membrane supported by Si chips. The membrane was constructed from SiO_2, with SiN_x used as a masking material for the required chemical etches. The K-kit's 2 chips were sealed 2-5 μm apart from each other using an epoxy mixed with 1 μm polystyrene beads, and the entire assembly was mounted on a standard TEM imaging grid for universal microscope compatibility. The K-kit was not designed with electrode contacts, as its primary purpose was for imaging soft biological matter, which also explains the large spacer between the windows. In these chips, the benefit of the thinner SiO_2 membrane allowed for fluorescent optical imaging of the dyed bacteria in the cell, for a cross study to be completed on the same samples.

This second liquid cell addressed one major problem with the first design, which is the difficulty in assembly. Removing the electrodes and the reservoir significantly decreased the number of fabrication steps and allowed construction of 115 chips simultaneously on a Si wafer. For the experiments presented, the limitations of liquid volume, lack of electrochemistry, and inability to refresh the solution were not a concern. The resolution was limited by the thick liquid layer, but for the large bacterial cells that were imaged this was not as significant of an issue compared to the nanocrystals from the original group.

At this stage of development, Zheng et al. showed improved resolution imaging of 1 nm in 2009[11] by modifying the cells demonstrated by Williamson et al. to have thinner SiN_x membranes, from 100 nm to 25 nm, and the spacers for the liquid layer to 100 nm. To compensate for the thinner membranes, the viewing area was reduced to ~50x10 μm, from the initial 100x100 μm, decreasing the pressure on the membranes such that they would not break inside the microscope.

Within the next year more customized approaches started appearing, including work by Diana Peckys in 2009 from USA[12] who replaced the K-kits' membranes with SiN_x, and used SU-8 as a spacer material for greater spacing control and smaller liquid layers. There were still no electrode contacts or electrolyte flow capabilities. Other inspired work includes that by Eugenii U. Donev and J. Todd Hastings from University of Kentucky in 2009, who sealed chloroplatinic acid solution within a capsule, and capped one side with a 150 nm polymide membrane[13]. Using this device in an SEM, they were able to show the first electron beam induced growth of palladium nanocrystals in a liquid environment.

Other work by Niels Jonge and Diana Peckys in 2009[14] demonstrated the first cited liquid cell with flow capabilities and the first cited work of *in situ* liquid cells' leading companies, Hummingbird

Scientific and Protochips Inc. The cell itself has a very similar appearance to the previous one mentioned by this group, however in place of a conformal sealing epoxy around the chip perimeter to hold the liquid between the chips, the edges remained unsealed and the sandwich structure was formed using 4 pillars, on each corner, of a 10 μm polystyrene-epoxy mix. The chips themselves were designed and fabricated by Protochips Inc. A custom TEM/STEM compatible holder was created featuring 2 fluid lines through the shaft leading to the assembled chips at the holder tip. The top and bottom of the chips were sealed against the edges of the holder using o-rings, and the 2 fluid lines acted as a 'via' through the sample holder to an external microfluidic syringe pump. In this manner, the pump was able to flow liquid into the microscope through the holder, between the 2 chips and over the viewing window, and back outside the microscope for disposal. This is the first LCEM holder reported, and was designed and fabricated by Hummingbird Scientific.

The custom holder provided the answers to many of the problems listed above. By sealing the liquid from the microscope with a dedicated holder and vacuum tight o-rings in a sandwich configuration, chips are manufactured more easily with a reduced risk of leaking into the vacuum of the microscope. The chips are not glued together, allowing for additional characterization after the *in situ* study, such as *post situ* SEM images of deposited and corroded structures, Raman Spectroscopy, Atomic Force Microscopy (AFM) and other surface characterization. Flowing the electrolyte allows for time-dependent reactions to be studied, electrolytes to be replenished for long experiments, and removal of radiolytic species.

Protochips shortly developed a custom holder compatible with most TEM systems, and both companies began to include a three-electrode system and second fluid input line to the holders, followed by further expansions including on-chip heating systems and gas based cells. Commercially available systems now offer a selection of electrode materials from carbon, gold and platinum, with various electrode, window, and liquid layer thickness geometries.

1.3 Objective of thesis

Objective 1: The first objective of this thesis is the design and fabrication of customizable *in situ* liquid cell chips, to be compatible with the commercially available 'Poseidon' liquid cell holder as distributed by Protochips Inc. The fabrication method should be compatible with common microfabrication techniques available at McMaster University, and should be scalable for high volume production of the liquid cells, to allow for cheaper, more frequent *in situ* experiments. The

process flow should allow for customization of the liquid cells, to allow for modification of materials and dimensions. The chips will be characterized for electrochemical comparability and applied for an *in situ* study.

Objective 2: Alongside the production of the liquid cells, there is motivation to improve the performance of LCEM. There are many experimental challenges that limit the scope and application of LCEM, including spatial and temporal resolution, window bulging, electrode materials, and electron beam damage. This work will focus on an approach to improve the spatial resolution of the system through selective material removal of the supporting membranes.

Objective 3: As with most characterization techniques, it is appropriate to conclude the development of the technique with examples of its application and use. In this work, LCEM is used to study the interactions of the high energy electron beam with the liquid media, and the resulting effect of the radiolytic species that are generated. As investigated by past members of the research group, palladium dendrites will be oxidatively etched *in situ* under various conditions to further understand the etching mechanisms.

1.4 Motivation

LCEM is a very rapidly growing technique, with applications in a wide variety of fields as listed previously. Utilization of a TEM offers superior spatial and temporal resolution for studying the solid-liquid interface to traditional characterization methods, while also providing a platform to study systems with spatial and spectral information simultaneously without risk of missing intermediate kinetics and dynamics. LCEM has been used as a nano-characterization technique for studying the structural evolution of materials under electrical, thermal, chemical, and radiolytic conditions, offering an application in a wide array of scientific studies.

As with any innovative technology, it has several of its own shortcomings to be improved upon. The current commercial standard offers limited customization of dimensions and materials, reducing the range of applications for the liquid cell. Additionally, the LCEM does not take full advantage of the sub-atomic resolution achievable in TEM systems, motivating modification of the liquid cell design for improved spatial resolution. The *in situ* technique will be applied to study the structural evolution of oxidative etching at the nanoscale to showcase the power of LCEM.

1.5 Thesis overview

Chapter 1 is an introduction to the goals of this project, and the introduction of the liquid cell for electron microscopy.

In chapter 2, the background physics of the existing technology is presented. This chapter provides quantitative motivation to improve commercial liquid cells by improved resolution, and electrode material customization. The physics for the experimental techniques to be used is derived, with important experimental and fabrication parameters highlighted. A background to the oxidative growth mechanisms of palladium nanostructures is also presented.

Chapter 3 addresses many of the decisions made in the optimization of the fabrication processes. Here the information derived in the background is applied to generate a process flow for microfabrication, characterization of the custom devices, and *in situ* experimental methods to demonstrate the proposed objectives. As design is an iterative process, multiple approaches will be presented.

Chapter 4 addresses the results and discussion surrounding the microfabrication and *in situ* experimentation presented from chapter 3. The discussion addresses how the fabrication steps were updated for improved performance and yield. The resolution enhancement technique was investigated through the *in situ* oxidative etching of palladium dendrites, with the results and conclusions presented here.

Finally, in chapter 5 we conclude the thesis by presenting further work to improve the results and understanding of this thesis, as well as experimental opportunities which become available as a result of the presented work.

2 Background

2.1 Chapter introduction

In this chapter a literature review is presented on the background theory and valuable information required to meet the proposed objectives. The topics covered will attempt to present the information from a broad scope, to a narrower picture specific to the objectives. By starting with the operation of an electron microscope, a discussion regarding how image formation is achieved within the liquid cell, and notes on how this is different from standard microscope operation logically follows. After this, it is important to address typical designs of liquid cells, and the experiments they are used for within the microscope. This presents the motivation for creating custom liquid cells, and the microfabrication technology required. Finally, several of the characterization methods and *in situ* experiments proposed are electrochemically based, which concludes the background.

2.2 Electron Microscopy

2.2.1 Microscopy – what is it

Microscopy itself is simply the use of a microscope, typically to study objects which are too small for the human eye to resolve itself. The first use of a microscope is attributed to 16th century work by Van Leeuwenhoek, who used a single rounded glass lens which was able to magnify objects by up to 400x, enough to see bacteria and cells. Since his work, the light microscope has been altered to incorporate additional lenses, most importantly the objective lens and eye pieces, to improve magnification by up to 1000x, with the current best possible resolution around 100 nm[15].

The basic principles of electron microscopy and light microscopy are the same – starting with a light or electron source (named the probe), a condenser lens is used to 'capture' and direct the probe through the microscope column, to illuminate the specimen. The objective lens is located closest to the sample and is what provides the magnification by focusing the probe to a point. Following this, a projector lens magnifies the imaged formed and projects it onto the viewing screen or detector – either an ocular eye piece for camera screen for light microscopes, or an electron florescent screen or electron camera for transmission electron microscopes. This system is illustrated in Figure 2-1. An additional setup is commonly used for both light and electron microscopes where the probe is 'reflected' from the sample surface back towards the eye piece or

detector. This second method provides surface information rather than bulk information of the sample. In Transmission Electron Microscopy (TEM) the probe illuminates the entire sample area, whereas Scanning Electron Microscopy (SEM) focuses the probe to a small point, which is rapidly scanned across the sample surface to generate a 2D image. TEMs may also be operated in scanning mode, known as Scanning TEM (STEM).

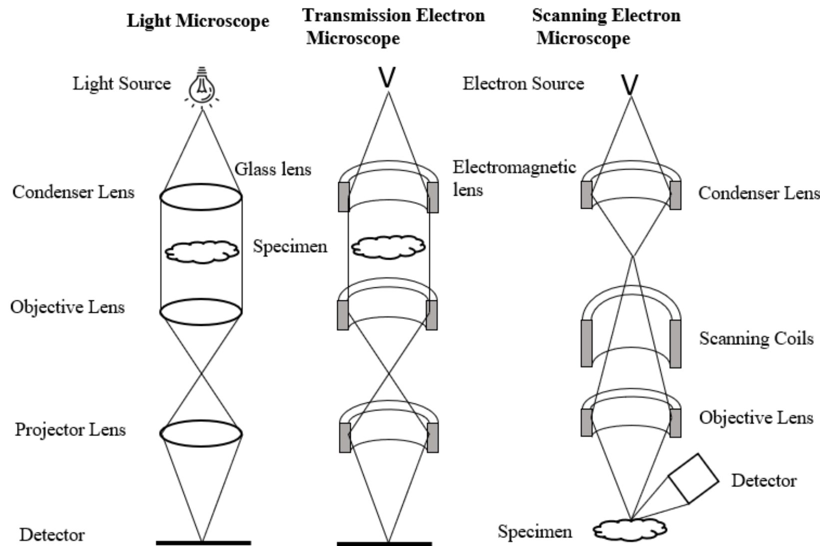

Figure 2-1 Simplified ray diagrams of light microscopes, and transmission and scanning electron microscopes

A key concept for both light and electron microscopy is the term resolution or spatial resolution, referring to the smallest size spacing between two light points distinguishable by the detector, or in other words the smallest object the detector can 'see'. The maximum achievable resolution is typically defined by Lord Rayleigh's criterion, stating that the central maximum for one Point Spread Function (PSF) lies on the 1st subsidiary maximum of a second PSF. When a probe passes through a lens, an effect similar to the famous single slit experiment occurs, where the probe interferes with itself creating a diffraction pattern. In the electron microscope, this occurs at the first crossover shown on the ray diagram in Figure 2-1, the 'back focal plane'. The self diffraction appears as a series of concentric disks of diminishing intensity, with a central bright spot known as the Airy pattern or PSF of the projected image, visualized in Figure 2-2. It can intuitively be seen that the resolving power is limited by the overlap of two neighboring central maxima.

The resolution of the human eye is approximately 0.1 mm, or around the thickness of a single strand of hair. Light microscopes, as mentioned, may improve this by up to 1000x, allowing

imaging of objects as small as 100 nm. An electron microscope may reach resolutions as small as 50 pm, or 10,000,000x magnification.

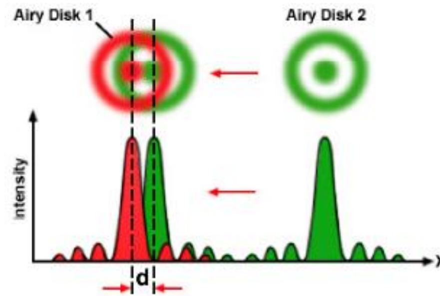

Figure 2-2 2D Airy disk patterns, and their overlap showing the Rayleigh criterion for imaging[16].

2.2.2 Imaging with electrons

In a light microscope, image formation is very straight forward. The photos are emitted from the source and focused to a point on the sample before magnification and detection. The photon energy (or wavelength) provides information such as colour or spectral absorption, and the image intensity at each pixel is determined by the number of photons absorbed, reflected, or transmitting by the sample at that location. The resolution available is limited by the wavelength of the light – a 400 nm or blue source may only detect an object as small as 400 nm. Higher energy Ultra Violet (UV) light allows for higher resolution, but to approach nanometer resolution requires much higher energy, in the x-ray regime. A TEM operates with typical electron accelerating voltages from 80-300 kV with electron wavelength on the order of 3 pm traveling at relativistic speeds, and hence electron microscopes are not resolution limited by the probe itself, but rather the objective lens transfer function, including aberrations.

In STEM operation, where the probe is focused to a point and scanned over the surface, the probe size is limited by the diffraction limit and any aberrations caused by the lenses. The diffraction limit for an ideal optical system is given by Abbe's equation[17]:

$$d = \frac{0.612\lambda}{n\sin(\alpha)}$$

Where d is the maximum resolution, λ is the electron wavelength, n is the index of refraction of the medium between the source and the point focus (1 in a vacuum), and α is the electron probe convergence angle. The relativistic De Broglie equation is used for calculating the electron wavelength from the accelerating voltage. To be consistent with future derivations, the probe

diameter which contains 50% of the total beam current will be used, yielding diffraction limited resolution to be[18]:

$$d_{diff} = 0.54\,\lambda/\alpha$$

The probe diameter limited by spherical aberrations is given by[18]:

$$d_{cs} = 2^{-5/2}\,c_s\alpha^3$$

With typical spherical aberration coefficient c_s=1 mm and electron beam convergence angle of 9 mrad. Spherical aberration corrected systems have c_s=0 mm. The diffraction and spherical aberration limited probe diameters are statistically independent and may be added in quadrature to find the probe limited resolution of a STEM system of d_{50}. For 200 keV accelerating voltage, a typical d_{50} is 0.2 nm. The Rayleigh criterion for resolution states the spatial resolution for resolving point objects to be $2d_{50}$. Inside the liquid cell, there are further beam broadening effects which further reduce the imaging resolution, to be addressed in the next section.

2.3 Liquid cell electron microscopy: electron-sample interactions

In this section, the electron-water interactions are addressed, with focus on how the sample has changed from a thin solid sample to a thicker bulk which interacts more strongly with the high energy electrons. The large sample bulk changes the resolution to be limited by multiple scattering effects, and the liquid solution undergoes radiolysis upon encountering the high energy electrons.

2.3.1 Image formation: Theory of spatial resolution

The image formation within the liquid cell is very similar to that with a standard solid sample, however the increased thickness induces multiple scattering events changing the spatial resolution to be signal to noise limited, and not from the electron optics. In this section the theory of spatial resolution is derived based from work from Niels de Jonge, 2018[18]. The signal to noise ratio (SNR), beam broadening, material type, sample geometry, and electron resolution will be investigated.

It is well understood that, in STEM mode, the highest resolution is achievable for objects near the top of the sample. The image is formed by electrons scattering to an angle of β or higher such that they reach the annular dark field detector (ADF), forming a ‘dark field’ image. During beam propagation through the bulk, multiple scattering events cause a beam broadening effect which contributes to background noise and defines the limiting factor for objects near the top surface.

Objects lower in the bulk are limited by the beam broadening causing delocalized electrons to contribute to the image contrast[19]. For STEM calculations, it is assumed the objects are near the top surface of the sample. Contrarily, for TEM imaging, highest resolution is achievable for objects along the bottom surface, and resolution is dictated by α, the opening semi angle of the electron beam, which is set using the objective aperture. In this case, a smaller aperture reduces beam brightness but improves resolution. TEM resolution is not directly discussed, only STEM imaging was used for experimental results, however the same electron-matter interactions still apply.

The probability of elastic scattering to a solid angle of θ or higher, which dominates high angle scattering towards the ADF detector, is listed below, based from the Rutherford scattering model

$$\sigma_{el}(\theta) = \frac{1}{\pi} Z^{3/4} \lambda^2 \left(1 + \frac{E}{E_0}\right)^2 \frac{1}{1 + (\theta/\theta_0)^2}$$

With atomic number Z, and electron energy E. The characteristic scattering angle θ_0, electron wavelength λ (relativistic), and electron rest energy E_0 are given by[18]:

$$\lambda = \frac{hc}{\sqrt{2EE_0 + E^2}}; \qquad E_0 = m_0 c^2 \ ; \qquad \theta_0 = \frac{\lambda Z^{1/3}}{2\pi a_H}$$

With physical constants: Plank's constant h, the speed of light c, the rest electron mass m_0, and Borh radius a_H. Similarly, the inelastic scattering probability to an angle θ or higher is given by:

$$\sigma_{inel}(\theta) = \frac{4}{\pi} Z^{\frac{1}{3}} \lambda^2 \left(1 + \frac{E}{E_0}\right)^2 \left[-\frac{1}{4(1 + \theta/\theta_0)^2} + \ln(\sqrt{1 + (\theta_0/\theta)^2})\right]$$

This yields the total cross-sectional scattering area to an angle θ or higher as

$$\sigma(\theta) = \sigma_{el}(\theta) + \sigma_{inel}(\theta)$$

Using this, the mean free path for scattering (total, elastic, or inelastic) is given by

$$l(\theta) = \frac{W}{\sigma(\theta) \rho N_A}$$

For a bulk of density ρ, molar average atomic weight W, and Avogadro's number N_A. The Beer-Lambert absorption law may also be written, showing the number of electrons scattered to an angle of θ or higher for a bulk thickness of t. Similarly, the number of electrons not scattered, or scattered to an angle lower than θ is given by M.

$$N = N_0\left(1 - e^{-t/l(\theta)}\right); \qquad M = N_0 e^{-t/l(\theta)}$$

This shows that beam scattering has a complex dependence on beam energy and that dense and heavy materials yield much higher scattering than light ones. Note that this model does not address absorption probabilities due to the high electron energy.

Taking the calculated number of scattered electrons, the signal to noise limited spatial resolution can be written, as derived by Niels de Jonge et al.[18]. Assuming the geometry of an object of thickness d near the top layer of the liquid cell with water thickness t and membrane thickness t_{SiN}, the number of signal electrons which reach the ADF detector is given by the scattering of each of these objects, as:

$$N_{signal} = N_0\left[1 - \exp\left(-\frac{d}{l_0} - \frac{t-d}{l_w} - \frac{2t_{SiN}}{l_{SiN}}\right)\right]$$

Which is simply the Beer Lambert law, including terms for the mean free path through the object l_0, water l_w and SiN_x l_{SiN}, and each of their thicknesses. Similarly, the number of background electrons will those scattered from the membranes and the liquid layer:

$$N_{noise} = N_o\left[1 - \exp\left(-\frac{t}{l_w} - \frac{2t_{SiN}}{l_{SiN}}\right)\right]$$

The SNR, written below, shows the ratio of the number of signal electrons compared to the total number of collected electrons. Generally, a SNR of ~3-5 is required to determine if a point is statistically significant form the background noise level, a threshold known as the Rose criterion[20,21]. Rearranging the equation for SNR to isolate for object diameter d yields the SNR limited resolution assuming negligible contribution from the SiN_x membrane.

$$SNR = \frac{|N_{signal} - N_{noise}|}{\sqrt{N_{noise}}} \geq 3$$

$$d_{SNR} = \frac{l_w l_o}{l_o - l_w}\left[\ln\left(-3\sqrt{\frac{(1 - e^{-t/l_w})}{N_0}} + e^{-t/l_w}\right) + \frac{t}{l_w}\right]$$

Assuming t ≫ d, a Taylor expansion is performed to simplify the minimum resolution to:

$$d_{SNR} = \frac{3l_o}{(l_w - l_o)\sqrt{N_0/tl_l}}$$

From this equation, we can see that the smallest resolvable object strongly depends on the scattering properties of the object such as atomic number and density, the number of imaging electrons, and the thickness of the liquid, which matches what we would intuitively expect. Note that here the contribution of the SiN_x membrane was assumed to be negligible. Analytically solving for the SNR limited resolution with the inclusion of the membrane is possible, but messy, so modeled parameters which require its contribution were solved through Mathematica and a closed form expression is not stated. A typical parameter measured in *in situ* LCEM is the number of electrons per unit area, or dose, D. The dose limited SNR resolution is obtained by replacing the total number of imaging electrons N_0 with the equivalent sample dose:

$$d_{SNR} = \sqrt{\frac{6l_0}{l_w - l_o}}\left(\frac{tl_w}{D}\right)^{1/4}$$

The SNR is not the only limiting factor to resolution. From here we examine the beam broadening during propagation though the sample. Typical beam broadening modeling assumes a single scattering event due to thin samples being smaller than the typical mean free path. In this case, a multiple scattering model is assumed, and yields a probe diameter d_{blur} of

$$d_{blur} = \frac{1.5}{2}\frac{\lambda^2}{2\pi a_H} z^{1.5} \sqrt{\frac{N_A \rho}{3\pi W}} Z(1 + E/E_0)$$

With z being the depth of the object of interest, and the diameter of the beam taken as the diameter containing 50% of the total beam current. Total beam broadening from multiple materials is calculated as the linear superposition of the broadening through each material individually. For TEM imaging, beam broadening can be thought of as blurring of the projected image onto the detector from objects lower in the liquid layer. This can be used to justify why objects near the bottom layer have the highest resolution in TEM mode.

The total resolution of the system depends on the beam broadening effects, the SNR limitations, and the beam diameter itself, modified by the Raleigh criterion. The effects are added in quadrature as they are statistically independent from each other.

$$d_{STEM} = \sqrt{(2d_{50})^2 + d_{SNR}^2 + d_{blurr}^2}$$

Before investigating plots of the maximum achievable resolution, there are several factors which should be discussed. In STEM imaging, the resolution has a very weak ($D^{-1/4}$) dependence on dose rate, meaning beam sensitive samples can easily be imaged without much loss in resolution. Contrarily, a very large beam dose increase must be used to improve the resolution of low contrast systems involving thick liquid layers and light elements, such as carbon. It is intuitive that heavy and dense materials have large cross-sectional scattering areas, which improves contrast in DF STEM imaging. Finally, the sample thickness t has a reduced influence on the final resolution for liquid layers smaller than the mean free path of the electrons through water, around 1 μm thickness.

These results show that the achievable resolution within the microscope is a function of many parameters, however the experimentally controllable ones are the opening angle of the ADF detector β, the liquid layer thickness t, and the electron dose D. Within each of these settings is also a dependence on the object density, thickness d, and depth within the liquid layer z, as measured from the top surface.

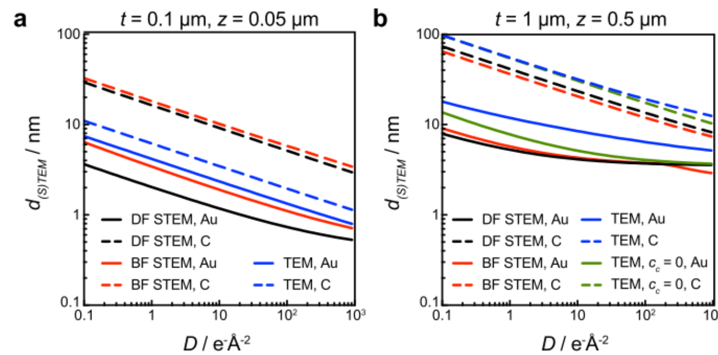

Figure 2-3 Relationship between electron dose and maximum resolution for LCEM, showing BF and DF STEM, and TEM results. The plots show different liquid thickness, and include data for several imaging modes and both a heavy element Au, and a light element C. The object is placed in the center of the liquid layer, with no SiN contribution, and optimal microscope and detector settings. TEM resolution is for phase contrast imaging, Cc is the coefficient of chromatic aberration. Image reproduced with permission from Elsevier[18]

It is immediately obvious from Figure 2-3 that larger heavy elements are easier to detect and provide higher resolution than light elements. Additionally, higher dose levels provide universally better resolution, although at a low dependence as the $D^{-1/4}$ relationship suggested.

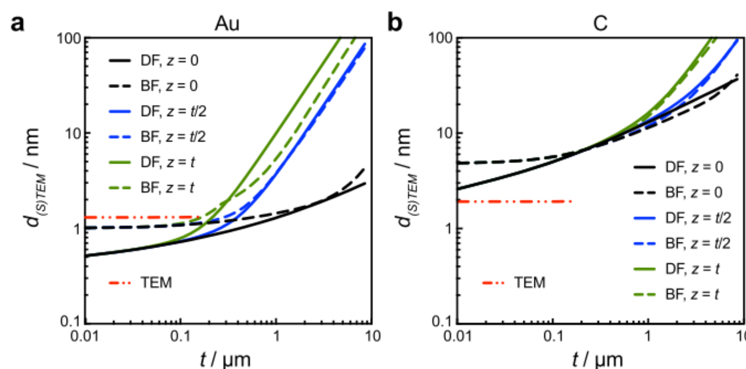

Figure 2-4 Using the same microscope settings Figure 2-3, the resolution as a function of liquid layer thickness t is calculated for Au (a) and C (b). Different object depth z is plotted. Effect of SiN membranes is not included. TEM imaging is phase contrast. Image reproduced with permission from Elsevier[18]

As predicted, thinner liquid layers provide higher resolution, due to reduced beam blurring (d_{blurr}) and background scattering raising the noise level of the image (d_{SNR}). It is also noted that for thicker liquid layers there is an extreme resolution difference between objects located near the top layer, z = 0, and the bottom layer, z = t, especially for STEM imaging modes. TEM phase contrast imaging is only available at very thin liquid layers, before the multiple scattering causes loss of electron coherence and loss of phase contrast.

Including the effect of the SiN_x membrane of 50 nm thickness into BF and DF STEM resolution, for liquid depths greater than ~600-700 nm there is minimal contribution from the membranes to reducing resolution. For liquid layers 100 nm and below, the scattering due to the SiN_x membrane causes more than a factor of 2 resolution loss and is more significant for lighter materials.

The membrane scattering is a significant challenge in improving imaging resolution. It has motivated much of this thesis to improve on commercially available liquid cells by modifying the membrane material. Here we see quantitative motivation for the drive towards graphene cells for atomic resolution imaging. In this thesis, as will shortly be presented, an approach which places small pin holes in the membrane material, without sacrificing the sealed pressure of the liquid cell, removes the scattering contribution of the membrane, improving the resolution.

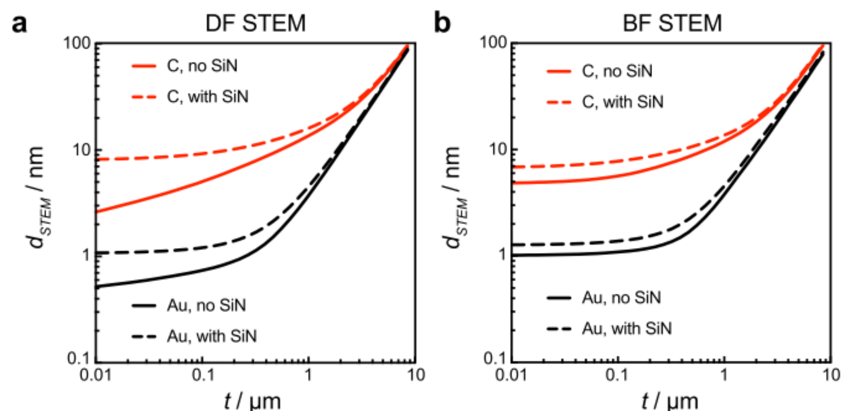

Figure 2-5 LCEM spatial resolution dependence on liquid layer thickness, with the inclusion of a top and bottom 50 nm SiN membrane. Same microscope settings as Figure 2-3. Object located at z=t/2. Image reproduced with permission from Elsevier[18]

2.3.2 Electron-water interactions and solution chemistry

It has been long known by radiology chemistry that bombarding liquid samples with high energy particles causes dissociation of the molecules into many complex high energy forms, as first shown by Giesel in 1902[22] who triggered the release of H_2 and O_2 gas from radium bromide solutions through the use of X-rays, which were discovered approximately 6 years earlier. As a basis for the discussion on radiolysis, water is used as it is the most popular solvent for *in situ* studies.

Radiolytic events in water are broken into 3 sub categories, physical, physico-chemical, and chemical, each occurring on largely different time scales[23]. The physical stage, within the first femtosecond (10^{-15} s) is the energy transfer phase, which excites water molecules to higher states, followed by quick relaxation resulting in ionized water, $H_2O^+ + e^-$, and excited water molecules H_2O^*. The physico-chemical stage, within 1 fs – 1 ns, the ionized water many react with nonionized water forming hydronium and excited hydroxides, the excited water molecules dissociate, and the free radical electrons dissolve becoming the aqueous or solvated electron. During the chemical stage, 1 ns-1 µs after exposure, the generated complexes diffuse into solution and chemically react with other present molecules and each other. These three processes are visualized in Figure 2-6.

Of the radicals generated in the chemical stage, the most prevalent are the aqueous electron and hydroxyl radicals, with smaller but relevant concentrations of excited hydrogen and dihydrogen.

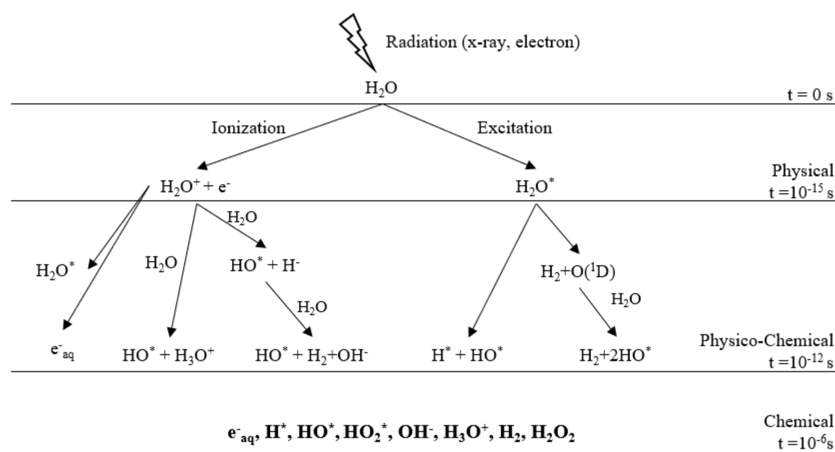

Figure 2-6 Three stages of water radioloysis, and dominant reactions in each stage

It was immediately realized by liquid cell microscopists that the generation of these radicals would alter the solution chemistry, which is routinely used advantageously to induce chemical changes resulting in deposition or etching of metal salts, typically referred to as electron beam induced phenomenon. The aqueous electron and hydrogen have standard reduction potentials of -2.9 V and -2.3 V[23] respectively vs the natural hydrogen electrode, which are very strong reducing agents and cause the precipitation of metal salts from solution. The hydroxyl radicals are very strong oxidation agents of +2.7 V standard potential, which act as stripping or etching agents.

The first work to use the radiology of water in the electron microscope was that by Eugenii Donev et al. in 2009, from University of Kentucky[13]. By trapping a liquid layer of chloroplatinic acid, H_2PtCl_6, in a small reservoir capped with a 150 nm polyimide membrane, they used an SEM beam to induce radiolytic species which triggered the reduction of platinum nanocrystals onto the membrane surface. Their work studied the effect of varying deposition times and beam currents on the growth rate of the nanocrystals, with post characterization to study the chemical composition of the structures and the nucleation conditions. This initial work showed that future characterization through changing the membrane material to SiN_x, and testing beam induced growth of other metals such as gold, silver, and nickel was desirable.

Since this initial work, further experiments within the TEM combined with data taken from radiolytic chemistry has produced well-characterized solution properties based on the imaging conditions and solution chemistry. A good example is the work published Woehl et al. in 2017[24], which summarizes and condenses much of this information. A few important concepts are drawn for this work and summarized here.

Two important conclusions from radiology are that first, species are generated relative to their concentrations within the solution, so dilute solutions (below ~100 mM) have primary reaction products based from the solvent not the solute, and second, the concept of a Gray (units Gy = J/kg) and G-values. The Gray shows the amount of energy in joules absorbed per kilogram of material, and the G-value is a measure of the number of produced molecules of a species per unit energy delivered to the material. For example, the G-value for the radiolysis of H_2 from water is 2.7 molecules/100 eV. These units are used to quantify many radiolytic conditions.

From this work, it is concluded that for water solutions of pH>3, there is an equal generation of the oxidizing agents, OH^{*-}, and the reducing agents, e^-_{aq} and H^*. Through the addition of 'scavengers,' the solution is altered to produce net oxidizing or reducing environments. For example, the organic molecules acetone and methanol scavenge OH^*, yielding net reducing conditions. High concentration scavengers may fully eliminate a radical species.

A full database of radiolysis reactions and reaction rates is freely available from NIST which, combined with summary tables in by Woehl et al., allow formation of net reducing or oxidation conditions for many common solvents and solutes.

Shown in Table 2-1 are the electron beam interactions with the liquid layer, and how electron beam properties influence the solution chemistry. Intuitively, high electron beam dose rates ($e^-/nm^2/s$) results in higher concentrations of radicals. By switching between STEM and TEM mode, it changes the radical generation to localized or broad area generation respectively.

Work previously published by Woehl et al. along with Abellan et al in 2014[25] extrapolates on these comments, concluding that there exists a 'threshold dose' of ~10 $e^-/Å^2$ below which no nucleation or beam induced phenomenon occurs. The critical dose may be found, for example, by using a solution containing aqueous silver Ag^+, which reacts with beam induced e^-_{aq} to form solid Ag precipitates. A beam current can be found that produces insufficient aqueous electrons to meet the saturation conditions required for the formation of Ag nanocrystal nuclei. Morphologies of formed nanocrystals help to find the threshold dose, with spherical diffusion limited growth formed at high dose rates, and faceted reaction rate limited particles formed closer to the limiting threshold[26].

Table 2-1 Solution chemistry and electron beam effects on LCEM. Reproduced with permission

	Experimental parameter	Characteristic[a] effect	Advantages[a]	Disadvantages[a]
Solution chemistry	Radical scavengers	React specifically and rapidly with certain radicals (e.g. isoproponal eliminates OH)	Certain radical species can be eliminated from the pool of primary radicals	Scavengers must be added in excess
	Additives (i.e. halide ions)	Alter oxidizing/reducing power of radicals and molecules *via* complexing and interconversion reactions	Complexation of metallic ions by halides increases effective oxidizing power of ·OH; Halides convert ·OH to more selective oxidizing agents	Require changes to solution chemistry; complexation reactions are only applicable to some noble metals (e.g. Cl^- complexes Au and Pt; Br^- complexes Pd)
	pH in aqueous solutions (neat water)	Alters concentrations of primary and secondary radicals	More predictable reaction limited nanoparticle growth kinetics at low pH	Require changes to solution chemistry; some reactions require specific pH
	Solvent type (e.g. aqueous, organic, aprotic, aromatic)	Controls the types of primary radicals formed	Control over radical *G*-values, e.g. aromatics have low *G*-values for radicals so reactions are controlled by molecular species	Solvents are not interchangeable for some syntheses; radiation chemistry of organic liquids is more complex than that of water
Electron beam	Electron dose rate	Determines the steady state concentrations of radicals	Requires no chemical additives	No specificity in types of radicals formed
	Imaging mode (STEM or TEM)	Controls how electrons are delivered to the liquid	TEM enables faster image acquisition and reaction modelling; STEM allows control over amount and location of dose	Some instruments not capable of STEM; TEM imaging often causes bubbling
	Accelerating voltage (neat water)	Affects the electron stopping power and radical G-values	High kV (300 kV) reduces radical G-values due to lower electron stopping power	No specificity in types of radicals formed; some TEM instruments do not allow variable kV

[a] References to each description in these columns are provided in the respective sections of the paper.

As seen in section 2.3.1 regarding image formation, the scattering cross section of particles is strongly influenced by beam energy, or accelerating voltage. High beam energy (300 kV) reduces scattering cross sections, netting fewer collisions and reduced radiolysis complexes, with the risk of introducing knock on damage to the system. It was found that lower beam energies (80 kV) produce similar growth profiles as high beam current situations, with electrolytic diffusion limited growth and saturation of radiolytic species. The opposite is true for high beam energy[26].

TEM and STEM mode irradiation differences also influence growth profiles and total electron dose per imaging frame. In TEM mode, global irradiation allows time resolution to be dictated by the detector speeds, whereas STEM applies high local irradiation for higher contrast. STEM images apply a pA beam current to an area of ~1 Å^2, at dwell times of ~0.5-5 µs per pixel, resulting in typical frame times of ~500 ms. Localized areas are irradiated under a very large current followed by a relatively long time between frames to 'regenerate' the solution. TEM flood imaging applies orders of magnitude fewer electrons per pixel per unit time, however total cumulative dose at the end of the exposure is significantly higher due to the continuous exposure.

Experimentally, there are many combinations of beam current, dwell times and magnification used to compare TEM and STEM modes, and any comparisons must be made for similar levels of dose

rate per second and per frame, and for total cumulative dose. Lower beam current (dose rate) STEM mode results in reaction limited growth of faceted particles, and higher rates yield diffusion limited spherical growth. Under similar cumulative dose, TEM experiences lower dose per frame, and diffusion limited spherical growth with lower nucleation density. Long-time beam illumination in TEM mode did not nucleate or increase the size of any nanocrystals, suggesting that the TEM beam caused depletion of precursor ions. It is concluded that the high local dose of STEM yields local saturation required for nucleation, whereas the global irradiation from TEM provides sufficient radiolytic species for diffusion limited growth, but reduced nucleation.

Primarily in TEM mode, a very sudden contrast and resolution improvement often occurs which is attributed to the formation of a gas bubble from radiolytically generated H_2 and O_2. Bubbles are typically formed under high electron beam irradiation, as seen in TEM mode. In STEM mode, once the radiolytic species are generated the probe is removed, allowing time for diffusion and recombination of species before more are generated. TEM continuous irradiation does not provide this relaxation, contributing to the increased prevalence of gas saturation and bubble formation.

2.4 Liquid cell electron microscopy: putting liquids in a vacuum

In chapter 1, a brief history of the key inventions in the development of the liquid cell was outlined. Presented here is a description of notable designs and approaches to liquid cell microscopy which are used in many research areas and provide unique approaches to LCEM which will be applied to meet the thesis objectives. Additionally, a review of LCEM applications and experimental methods is outlined with emphasis on using these applications as characterization methods of LCEM as a microscopy technique.

2.4.1 Alternative liquid cell designs and systems

With the invention of a system to trap volatile liquids within effectively transparent membranes, liquid cell microscopy sparked interest into a wide field of research, including the design of other liquid cell geometries. The cells first discussed in the introduction are typical examples of 'glued' chips, where the hermetic seal is formed by gluing an upper and lower chip together. The system adopted by commercial production has been a clamping mechanism, creating a liquid seal using o-rings and tightening screws, with 2 chips spaced apart by surface-printed structures. With these designs, there was a large disadvantage of needing alignment between the upper and lower windows. The windows are required to be large to allow the upper and lower chips to align with

each other, and as will be discussed in the next section, the larger windows required thicker membranes for support which limited the spatial resolution. With that said, a currently unspoken advantage of the 2-chip design is the ability to pattern or modify the interior of the chips prior to use followed by *post situ* characterization after use. In the remainder of this section, several alternative designs to the clamped cell are presented, each with the goal to minimize various difficulties faced by LCEM.

In 2012, the first graphene liquid cell was presented by Jong Min Yuk et al. at University of California at Berkley[27]. The cell comprised of a liquid droplet of <100 nm in diameter encapsulated between two graphene sheets, which were held together using van der Waals forces. Graphene is a 2-dimensional material which is impenetrable to liquids and gasses, providing incredibly high spatial imaging resolution.

The cell was constructed by growing graphene on a Cu substrate through chemical vapor deposition (CVD), and then transferred to a gold TEM grid with an amorphous carbon support. Two of these grids were prepared, and a palladium ion solution was pipetted between the two grids, which are then pressed together. The van der Waals forces between graphene sheets holds them together as one TEM mesh and the carbon supports are removed, yielding the graphene encasement on a single TEM mesh. With such an encasement, the mesh is loaded onto a standard TEM holder, and the small liquid pockets between the graphene sheets can be imaged. In this work, the electron beam was used to induce growth of palladium nanocrystals which was studied with atomic resolution.

The use of graphene as a membrane material prevents non-specific adsorption to the side walls due to the chemical inertness of graphene, allowing for study of diffusion and particle motion dynamics[27]. Additionally, the small sample volume and high electrical and thermal conductivity of the graphene cause accumulated charge and heat to be quickly transferred away, which is beneficial to sensitive biological samples[28].

The graphene cell provides unprecedented resolution, although it also has some inherent limitations. There is no way to control the size or thickness of the liquid droplets formed, making reproducibility of experiments challenging, and the system does not provide a good platform for incorporating electrodes, heating, and cooling for more complex experiments.

A second generation of this cell, which is very similar to a 'microcell' which will be presented shortly, is to use graphene to seal holes in a perforated membrane. In this case, a membrane typically 200 nm thick is controllably perforated with holes between 100 nm and 1 µm in diameter. Graphene is used to seal one side of the through holes, the solution of interest is deposited in the holes, and capped on the other side with a second graphene sheet. By this method, microwells with highly controlled thickness and dimensions are created, and imaging occurs through monolayer graphene. This second-generation graphene cell suffers many similar limitations and challenges as the first generation, aside from greatly improved control over the microwell dimensions.

Several other microcell systems have also been created in a similar fashion, such as that available from Protochips Inc. and those demonstrated at Virginia Tech Carilion Research Institue[29], with the wells capped in SiN_x, SiO_2 or a metal plates, and shown in

Figure 2-7. In this case, a semi-perforated SiN_x membrane is constructed, with the microwells built into the membrane. The wells are filled with the solution of interest before the system is sealed with a second membrane.

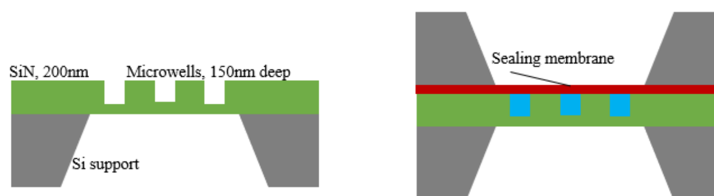

Figure 2-7 Concept design of a microwell liquid cell system. (Left) SiN membrane with microwells.(Right) Sealed system, after addition liquid of interest and a sealing membrane.

A third form of graphene cell, known as the graphene flow cell, offers a hybridization of the commercialized Protochips design and the microwell design. Typical SiN_x window chips have very large viewing areas, which bend and deform under the pressure difference of the microscope vacuum compared to the liquid pressure. Obtaining graphene sheets this large is very difficult to do, and they will not have the strength necessary to support the pressure difference. An alternative would be to create a series of connected microwells in a support membrane to create a channel through the membrane. A second material such as SiO_2 could be used to form bridges across the channel, effectively reducing the span of the required capping graphene sheets. The graphene would seal both top and bottom of the channel, leaving a series of interconnected graphene microwells for imaging. Using this system, the full benefits of the commercial system could be

realized, including electrodes, heating, and flow of electrolytes. Such a system was proposed and patented in 2014, with no current published results[30].

Another interesting approach is the monolithic chip, which requires only a single wafer rather than a sandwich of two systems used by graphene and commercial cells. Monolithic chips do not suffer from alignment issues of the top and bottom membranes, allowing for smaller channel widths and windows to be made, which in turn allows for thinner window materials. One system is demonstrated by Eric Jensen et al in 2014[31]. The system started with typical manufacturing seen thus far, forming a free supported Si_xN_y membrane on a Si support wafer. A sacrificial layer is then deposited above the membrane and patterned to form the channel. It is then coated with a top layer of Si_xN_y, and a small inlet and outlet are etched into each end of the top layer. A wet chemical etch is then used to remove the interior sacrificial layer of the channel, forming a thin channel on the membrane surface.

Many other innovative designs for capturing liquid within electron transparent membranes which look to minimize several of liquid cell microscopies' challenges and improve characterization of a specific system have been proposed; however, in many cases the commercially available clamped SiN_x window design is general enough to for a wide range of experimental conditions.

2.4.2 Window bulging

In several sections so far, there have been mentions of window bulging and window thickness limited by high pressure difference between the interior and exterior of the cell. It was concluded without explanation that a 50 nm thick SiN_x membrane with a typical span of 50-550 nm is often used. In this section a discussion of window materials is presented.

The membranes must meet three specific requirements: have high electron transparency, have high stiffness to resist the pressure difference, and must be easily microfabricated using common MEMS and cleanroom processing. The most common materials are silicon rich silicon nitride Si_xN_y, stoichiometric silicon nitride Si_3N_4, silicon dioxide SiO_2, polyimide, and the 2D materials graphene and hexagonal boron nitride hBN. Note that SiN_x refers to nitride layers whose elemental ratio is not stated, and may refer to either Si_xN_y or stoichiometric Si_3N_4.

The 2-dimensional materials have high material stiffness and unmatched electron transparency, but they are not producible on large scale, and sheets are not large enough to form sufficient

viewing areas. 2D materials are typically used for microwells or bubble encapsulations and are not viable for flow type geometries.

Silicon nitrides and oxides are very commonly used within MEMS processing and are relatively electron transparent due to the light elements present. SiO_2 has a low Young's modulus, causing a large amount of bulging under the pressure difference. Stoichiometric Si_3N_4 has a high Young's modulus and is grown using Low Pressure Chemical Vapour Deposition (LPCVD, to be described later). Unfortunately, silicon nitrides' crystal structure has a thermal expansion coefficient mismatch with crystalline silicon substrates, yielding large residual stress in the thin film which often leads to breaking of the membranes, limiting its use. By incorporating large amount of Si into the film, typically 2:1 ratio of Si:N, the film becomes amorphous and has a closer thermal expansion coefficient match with Si leading to lower residual stress and a lower Young's modulus, near that of SiO_2.

Polyimide is a very soft material with a significantly lower Young's modulus than the previous materials, yielding a large degree of bulging and increased liquid layer thickness. It is also not producible through regular cleanroom methods and films are typically not thinner than 150 nm. For SEM LCEM, the liquid layer thickness is not a limiting factor as electron interaction volumes are much larger than in TEM, so the thicker membranes are not as hindering. Polyimide membranes are therefore viable for SEM cells, but not TEM.

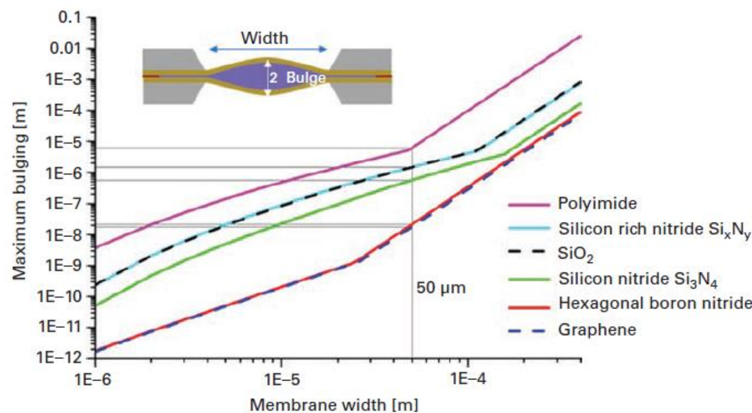

Figure 2-8 Membrane bulging as a function of membrane width, for 50 nm thick membranes. A pressure difference of 10^5 Pa is applied. Note polyimide typically uses 150 nm thickness, showing reduced bulging than displayed here. Graphene as a single layer, rather than 50 nm would also show very different results. Reproduced with permission from[32]

We can see in Figure 2-8 the membrane bulging as a function of membrane width for each material, which shows that high Young's modulus results in less deflection. Intuitively, membranes with a

larger span will be able to bulge more. To this end, many membranes are designed with one dimension as small as possible, while maintaining a suitable viewing window, with a typical compromise around 50 µm as marked on the graph. At this width the window bulging approaches 1 µm for Si_xN_y and SiO_2 membranes, significantly complicating control of the liquid layer. As seen in the maximum resolution calculations neglecting the membrane scattering, a 1 µm liquid layer thickness has nearly 10x lower resolution than 100 nm.

One technique to avoid the bulging effect is by imaging near the edges of the windows, where bulging is intuitively less prevalent. This becomes more challenging for 2 chip systems, where a slight misalignment of the chips within the sandwich results in the 'edges' of the windows being in distinct locations relative to each other, and no minimum bulging location can be found. The approach often adopted by these systems is to orient the membranes perpendicular to each other, reducing total viewing area but guaranteeing the corners of the formed viewing areas will be at the minimum bulging edge of each chip.

This significant membrane bulging has led to motivation for making monolithic chips, or gluing and bonding the windows together, effectively shrinking the membrane span to reduce bulging. Note that most microwell setups have well dimensions smaller than 10 µm, which also experience significantly less bulging.

2.4.3 Applications for the liquid cell

The previous background sections have eluded to many different experimental methods which take advantage of the liquid cell for its unique spatial and temporal resolution of liquid samples, as well as studying the effects of electron-liquid interactions. In this section we formally introduce the types of experiments typically performed, with a focus on works related to the thesis objectives.

Experimental techniques are broadly distributed into four groups: aqueous imaging, beam induced phenomena, external stimuli, and correlative measurements using spectroscopic imaging along side the stimuli. In all experiments it is important to decouple the effect of the electron beam from the external stimuli, making all experiments, at some level, fall into the beam induced category.

Aqueous Imaging is important for biological fields, where traditionally the sample must be freeze dried or placed in a cryo system, often killing the artifacts of interest. Nanoscale resolution of live cells opens many possibilities including the studies of protein dynamics and cellular membrane

geometry changes; however, it is unknown if the electron beam effects will destroy the cells function[33]. Additionally, aqueous imaging is used to track and study Brownian motion of particles in confined spaces and investigate the influence of the membrane materials.

External Stimuli are generalized into electrochemical, heating, and liquid flow experiments, where an external driving force is applied upon the liquid to induce a visible change.

Electrochemical techniques, often electrochemical deposition of metal salts, or corrosion mechanisms controlled through electrochemical cycling, have an opportunity for dynamic studies on growth and etching profiles. As discussed in the introduction, initial liquid cells studied the electrodeposition of copper onto gold electrodes using a 2 electrode system[1,9], visually showing and quantifying the factors influencing nucleation density and growth rates from nucleation sites. Other works have revealed a modification to the models of the short- and long- term growth profiles of palladium structures[34], as well as the structural degradation of catalysts for fuel cells[35]. Electrochemical biasing allows direct study of operations within a battery, including incorporation of Li into anode materials, changes to the structural and chemical properties of the electrodes, and anode volume changes during operation[36].

Corrosion mechanics are studied by visually tracking the location where pitting nucleates within protective films, such as those on stainless steel and aluminum, after exposure to salt solutions[37,38]. This is done with and without electrochemical potentials. However, electrodes are often used to record the current vs voltage of the dissolution profile.

Heating methods often apply heat to induce a phase change or to change the rate of a reaction. Localized heating of water nucleates bubbles into the solution, and monitoring their nucleation density, growth rate, and stability yields information regarding the phase change dynamics[39].

Flow systems are used to replenish reactants in electrochemical or heating setups, remove by-products from a reaction, change solution chemistry during imaging, or in newer commercial systems, combine two solutions and image the mixing dynamics. Flow capabilities allow studying of diffusion dynamics of nanoparticles and bubbles within a closed space, but this is often complicated by particles sticking to the windows or by beam induced phenomena.

Beam-induced phenomena study the electron-solution interactions. For example: using the electron beam to generate e^-_{aq} which reduce metal ions and cause precipitation of metal

nanocrystals; beam induced oxidative conditions which cause stripping and corrosion of thin films; or generation of nano-bubbles for the study of nanophysics; and other radiolytic experiments.

Initial work with liquid cells showed beam induced growth of palladium structures, and characterized new growth pathways which were not realized until visual tracking of the mechanics was studied[11]. An electrochemical study at McMaster traced both beam induced growth of gold nanoparticles and electrodeposited particles, and compared their growth mechanisms and morphologies[40]. This work showed that beam induced growth and electrodeposited growth forms significantly different nanocrystal morphologies, related to the saturation or depletion of reactants within the imaging area forming either diffusion limited or mixed kinetic-diffusion growth profiles. It was shown that large liquid layers reduce or eliminate beam induced artifacts, likely due to the radiolytically generated species falling below a threshold concentration.

Correlative simulation and *in situ* studies for gold nanocrystals aimed to modify solution chemistry and beam dose rates to understand and control the growth modes of gold nanostructures[41]. These studies conclude that linear growth rates do not vary with object size or shape (along vertices, edges and faces) and growth is limited by the formation of Au atoms. High beam dose rates increase linear growth rates, further supporting this conclusion. Low pH solutions containing Cl^- ions show close linearity between beam current and growth rate. Through altering solution chemistry and dose rates, a growth model showing high diffusion of surrounding Au^{+3} ions to form the generated nanocrystals was developed, as well as relative reaction rates required to convert Au(III) to Au(0) through the formation of various AuCl complexes. This proves that tracking of the Cl^- and e^-_{aq} concentrations is important for gold growth models.

Other work with gold has shown that surface reaction rates have equal dependence on electron dose rates and concentration of reducing agents within the cell. By balancing gold concentrations and dose rates, a critical rate resulting in 3 monolayers of gold per second was achieved, above which formation of nanoplates is not possible. Using the slow growth conditions, the effects of thermodynamic and kinetic growth profiles were separated, allowing for controllable faceted growth of nanocrystals[42].

It is important to note that in all the above reports, many of the conclusions were determined by *post situ* analysis of the grown structures, through either TEM or SEM imaging of liquid cell chips

after the initial experiments. This is in part due to the limited resolution within the liquid cell not providing sufficient information, and by the difficulty in interpreting the *in situ* results.

An interesting system of study is that of palladium nanostructures electrochemically grown and oxidatively etched on an electrode. Palladium nanocubes are, among other uses, used for hydrogen storage due to the unique ability to ad- and absorb hydrogen and it has been shown that increasing the number of facets improves the catalytic properties. Electrochemical methods are often used to study the hydrogen evolution and absorption properties[43]. During operation and fabrication, the interaction between the palladium deposits with the supporting electrolyte, HCl, and palladium-chloride complexes is of great interest. Specifically, it has been predicted that specific palladium planes allow formation of palladium-chloride complexes which act as a blocking agent to future growth or etching[44]. The solution conditions including pH and HCl concentration dictate which complexes may form in solution[45]. Finally, palladium-hydrogen alloys may form during growth yielding brittle nanostructures[46].

Yingying Jiang et al. in 2014[47] studied the *in situ* etching of palladium nanocubes of 18 nm side length in 0.01-0.1 mol/L KBr solution under the effect of the electron beam. Under the 200 keV beam acceleration, the nanocubes began dissolution from the edges and vertices, forming nanospheres before complete dissolution, after about 30 s under the electron beam. The Br^- ions in the solution oxidatively etch the Pd, transforming it to Pd^{+2} and forming complexes including $[PdBr_4]^{-2}$, which was shown to only occur in the presence of oxygen in the solution. During the *in situ* experiments, oxidizing agents were introduced radiolytically in the form of OH^*, HO_2^*, O and H_2O_2 by the electron beam. Comparing *in situ* results with HRTEM images of *ex situ* structures at various stages of etching showed the transition from a vertex-truncated cube to polyhedron, before forming very small nanoclusters and completely dissolving. The *in situ* resolution was not sufficient to trace the etching of the faceted sides, however nanoparticle diameter as a function of time was recorded to determine etch rates.

Similar *ex situ* work completed by Jinfeng Zhang et al. in 2013[48] showed shape controlled etching during fabrication of nanocubes by controlling the ratio of precursor solution H_2PdCl_4 and HCl. This work showed that small inclusions of HCl would truncate the vertices of the cubes exposing {111} planes, with higher HCl concentrations yielding increased oxidative etching to form cuboctahedrons or complete octahedrons. In their work, they discussed that the presence of H^+

ions raise the oxidative potential of oxygen, allowing stronger oxidative etching of the palladium surface, with oxidized palladium transported away through Cl complexes including $[PdCl_4]^{-2}$.

Previous work summarized by Jie Yang, 2018[49] and expanded upon in the liquid cell discusses the inclusion of HCl with the palladium complexes during electrochemical cycling, and the interaction between the palladium salt and the Pd-Cl complexes to form specific palladium dendritic structures. Applying CV cycling and CA, the structural evolution of the Pd dendrites was characterized with and without the presence of HCl. Low solution pH through the inclusion of HCl allows palladium chloride complexes to be stable, which inhibit reduction and increase the dissolution rate of the palladium dendrites. Previous work suggested that Cl ions form blocking sites on specific crystal planes of the palladium structures, modifying growth structures, with the effects visualized here.

In this thesis, it is worth separating the growth and etching phases of the Pd cycle to study the effect of HCl etching of pre-deposited palladium dendrites without the presence of H_2PdCl_4 in the solution. Similarly to oxidative etching in KBr presented above, the structures will be oxidatively etched under the stimulus of the electron beam and under a reducing applied potential.

Correlative spectroscopic experiments use systems known as Electron Energy Loss Spectroscopy (EELS) and Energy Dispersive X-ray Spectroscopy (EDX or EDS) to obtain chemical composition from the image. EELS detects the loss of energy from the transmitted electrons due to scattering events, which is specific to chemical compositions, and has also been applied to measure the t/λ ratio, the thickness of the liquid compared to the mean free path through the liquid, to actively measure sample thickness and window bulging. EDX captures X-rays generated by the sample due to beam induced excitation and relaxation of target electrons, which is used to obtain elemental mapping. EDX is difficult in sandwich setups because the support Si, sealing o-rings, and metal plates absorb many of the emitted X-rays.

2.4.4 The holey liquid cell

Of interest to this thesis is the work by Li Yang et al. at Pacific Northwest National Laboratory. They have developed an *in situ* liquid channel compatible with SEM, time of flight secondary ion mass spectrometry (ToF SIMS), optical microscope, or any other analytical tool with a probe size at or smaller than ~1 µm[50–52]. Their system incorporates many ingenious properties, most notable being a hole in the membrane of the liquid channel, exposing the contained liquid to the vacuum

of the probe system. The remainder of this subsection will refer to the work presented in the aforementioned papers, unless otherwise noted.

The system provides a micro liquid environment, sealed with a thin membrane, which is selectively milled to form a hole breaching to the vacuum that confines the liquid. The general operating principle is that the small hole diameter and high water surface tension maintains the vacuum, allowing for probing at the surface-vacuum interface.

Recalling section 2.3.1: Image formation: Theory of spatial resolution, at low liquid layer thickness the SiN_x membrane poses a significant loss of resolution. By combining the holey liquid cell with TEM LCEM it is proposed that resolution enhancements may be made within the SiN_x enclosed chip design. To this end, several relevant design considerations for a holey cell will be addressed, with emphasis placed on adaption for the TEM environment and Protochips liquid cell.

Aperture size plays a significant role in determining other constraints on the device. Yang et al proposed a 3 μm diameter for the hole due to the 200-300 nm resolution available to spectroscopic SEM techniques and to ToF SIMS lateral resolution, which forms a reasonable viewing window. LCEM typical resolution is <10 nm, however fields of view are on the order of 1-5 μm. To this end, a 1 μm diameter hole will be assumed for the following calculations.

Surface Tension of the liquid maintains the vacuum environment, which is calculated using the standard 'bubble point' formula for capillary flow through channels.

$$V = \frac{\pi h(3R^2 + h^2)}{6}; \qquad U = \sigma A = \sigma\pi(R^2 + h^2)$$

$$P = \frac{dU}{dV} = \frac{4\sigma y}{R^2 + h^2}; \qquad P_{max} = \frac{2\sigma}{R}$$

The surface energy U is given by the area A of the bubble times its surface tension σ. The pressure P of the bubble is simply the derivative of the surface energy with respect the bubble volume V, the volume of a hemisphere, where h is the height of the bubble from the aperture. The pressure is maximized in the centre of the bubble, for y = R. Taking[53] σ =0.073 N/m and R = 0.5 μm, yields a maximum pressure of 292 kPa, or 2.92 bar. The pressure for a 3 μm diameter hole is 0.97 bar.

The surface tension of water must be able to withstand the vapour pressure of water, 0.023 bar at room temperature, plus the pressure caused by flowing the solution through the channel, about 0.1-

0.2 bar. With the maximum pressure calculated, the chosen aperture is more than sufficient to maintain a mechanical seal for the cell. It is important to note that dissolved gas within the solution will be at a pressure of 1 atm, approximately 1 bar, which will be sufficient to destroy the seal. To this end, all liquids must be thoroughly degassed prior to use in a holey system.

Mean free path of probe: Due to evaporation of water from the liquid surface, there is expected to be a 'cloud' of water molecules surrounding the hole at a partial pressure of 0.023 bar for pure water at room temperature. The mean free path for 1 keV electrons in this density of vapor is $\lambda_{e-} \approx$ 1 mm. For TEM, the electrons have much higher energies (and velocities) at 80-300 keV, which would extend the mean free path length. The vaporized cloud must be sufficiently smaller than λ_{e-} to ensure no significant loss of probe electrons. Photons for EDX imaging also traverse this cloud, however they have smaller scattering cross sections and their mean free path is significantly longer.

The next step is to calculate the size and average density of the vapor cloud. In an equilibrium system of evaporating and condensing vapor, the evaporation rate is equal to the thermal effusion rate E (rate of gas molecules hitting the surface) times the sticking probability S, defined as the chance the water molecule will stick to the surface. For water sticking to water, this is often assumed to be unity[54]. The evaporation rate is given by

$$ES = \rho_0 \sqrt{\frac{kT}{2\pi m}} S$$

Where ρ_0 is the number density of water molecules, k is the boltzman constant, T is temperature in Kelvin, and m is the molecular mass of the water. The holey cell is not in equilibrium due to diffusion of gasses into the vacuum system, and thus the number density at the surface will be half of this value, the evaporating molecules only, decreasing with distance from the hole.

For diffusion radius of r away from an aperture of radius R, the number density of water molecules is approximated by

$$\rho(r, \theta) \approx \begin{cases} \dfrac{\rho_0}{2} & r \leq R \\ \dfrac{\rho_0 R^2}{r^2} H(\theta) & r > R \end{cases}$$

Where H(θ) is the angular distribution of the particles, which is assumed constant and will only be altered by an external source modifying the diffusion away from the aperture. The $1/r^2$ approximation is accurate for constant velocity particles. Using this equation, the electrons must travel through distance R with average density of $\rho_0/2$, and a regime of declining pressure further from the aperture. This is simply the integral from R to infinity of p(r,θ) dr. The net result is that the probe travels a total effective distance of 2R through an average particle density of $\rho_0/2$, or equivalently through distance R at particle density of ρ_0.

The mean free path of 1 keV electrons through 0.023 bar of water vapour is ~1 mm. An aperture radius and equivalent vapour cloud radius of 1 μm, which is three orders of magnitude smaller than the electron mean free path, will yield negligible probe loss due to evaporating species.

Aperture gas load: Clearly, as the previous section suggested, gas molecules will be escaping from the surface of the liquid and contributing to a gas load within the microscope. Electron microscopes typically operate at 10^{-6}-10^{-7} Torr, and a significant gas load will 'crash' the vacuum causing the microscope to shut down. It is important to ensure the gas load is sufficiently small that the vacuum pumps will compensate for the additional load, and that any evaporated species do not damage the microscope. For the following discussion on gas loads into the vacuum systems, all concepts and equations are attributed to work presented by Leybold in 2016[55], and that of R. Kersevan of the Technology Department: vacuum, surfaces and coatings department of CERN working with European Science Institute and the Joint Universities Accelerator School in 2017[56].

To calculate the gas load, we model the system as a perfect vacuum with a small aperture holding off 1 atm (~1.01 bar) of gas. When a valve is opened releasing the gas, the gas will flow into the vacuum at the speed of sound, 343 m/s for air, or ~429 m/s for room temperature water vapor[57]. The quantity of air flowing into the vacuum is given by

$$q_{L-water} = \Delta p * v_s A = (p_{water} - p_{vacuum}) * v_s A$$

Where the gas pressure ρ_{water} is the partial pressure of water (equal to vapor pressure in this case), the vacuum is approximated to be perfect at zero pressure, the speed of sound v_s was stated above, and the area is the surface area of the hole, given by $A = \pi R^2$, with a chosen radius of 1 μm. Note that this equation holds true for an infinitely thin hole, which is a good approximation for the 50nm

thick membranes. This nets 2.52x10^{-5} mbarL/s of gas entering the system. This leak will be compensated by the vacuum pump such that the final pressure in the chamber is dictated by

$$P_{final} = \frac{q_L}{S_{eff}} = \frac{Leak\ Rate\ \left[\frac{mbarL}{s}\right]}{Effective\ Pumping\ Speed\ \left[\frac{L}{s}\right]}$$

Most TEM systems have several vacuum systems, with the primary pump ranging from 10-300 L/s pumping speed[58,59]. An average value of 100 L/s and chamber size of 30 L nets a final pressure rise of 1.88x10^{-7} torr due to the leak which is lower than the operating pressures of the microscope.

In the above calculation, there was one potentially significant assumption that was made: the effective pumping speed is equivalent to the actual pumps pumping speed, which neglects diffusion of gasses to the pump. In the simplest scenario of a singular tube with the pump at one end, the gasses will interfere with the walls of the tube during the journey towards the pump, considered as a 'resistance to flow', and defines the 'conductance' of a vacuum chamber. Effective pumping speed is modified by the conductance of the chamber by the following:

$$\frac{1}{S_{eff}} = \frac{1}{C} + \frac{1}{S_0}$$

Where S_{eff} is the effective pump speed, C is the conductance, and S_0 is the actual pump speed. The conductance depends on chamber length and diameter, but also on how direct of a path it is towards the pump. The overall conductance of the system is, in practice, minimized though changing the number of pumps, the spacing and location of the pumps, and the vacuum chamber geometry. It is typically calculated through Monte Carlo simulations, although there are several highly approximate equations to be used as baseline values for estimation of system costs.

It becomes very complicated to calculate effective pumping speeds, and the is beyond the scope of this work. Using a rough model for a typical column-based chamber, S_{eff} is estimated by

$$S_{eff} = \left(\frac{l}{12C} + \frac{1}{S_0}\right)^{-1}$$

With l being the length of the column (~3 m for a TEM), and a conductance of about 20 Lm/s, the 100 L/s nominal pumping speed for one vacuum pump is dropped to 44 L/s. This is a pessimistic estimate due to TEM's containing a vacuum pump within a few centimeters of the sample stage.

Although this is a very rough estimate, with typical conductance values in this range the pressure rise of the system would still be negligible.

Temperature change: As any introduction to thermodynamics class will explain, evaporation is an endothermic process requiring surface molecules to gain energy and transfer into the gas phase. Here the energy for evaporation must come from the bulk liquid, cooling it and risking freezing along with local changes in solvent concentration. The following calculations are adopted from the initial developers of the holey cell, Li Yang et al.[52].

An approximate geometry of a spherical system bowed into a hemisphere is used in place of a cylindrical aperture and hemispherical bulge, for simplicity. Following diffusion laws and assuming evaporation from the entire exposed surface, the concentration C as a function of time t is expressed in terms of the diffusion constant D, initial concentration C_0, disk radius R, and hemisphere height h, as written below.

$$D\nabla^2 C = \frac{\partial C}{\partial t}$$

$$\frac{\partial C}{\partial r} = h(C_1 - C) \quad for\, r = R$$

Substituting $h' = h + 1/R$

$$\frac{C|_{r=R} - C_0}{C_1 - C_0} = \frac{hR}{(1 + hR)}\left[1 - \exp\left(h'^2 Dt\right) * erfc\left(h'\sqrt{Dt}\right)\right]$$

Where erfc is the error function. This equation represents a system which at t=0 begins to experience molecular diffusion from the spherical surface defined at r=R. This general diffusion equation is mapped to represent temperature diffusion through several variable replacements.

- C is replaced by temperature T
- D is replaced by thermal diffusivity, κ/c. κ = thermal conductivity, c = volumetric heat capacity
- h is replaced by $B(T_0)c/\kappa/(T_0-T_1)$. B(T) is the evaporative heat load per unit area which depends on temperature and is calculated from the latent heat of vaporization. For linearization, B(T) is approximated by $B(T_0)$, the heat loss at time zero. T_1 is the temperature at which B(T) is at a value of zero.

With these changes, the surface temperature as a function of time is expressed by

$$\frac{\kappa}{c}\nabla^2 T = \frac{\partial T}{\partial t}$$

$$\frac{\partial T}{\partial r} = \left(\frac{B(T_0)c}{\kappa(T_0 - T)}\right)(T_1 - T) \quad for\, r = R$$

$$T|_{r=R} = T_0 + \frac{(T_1 - T_0)hR}{1 + hR}\left[1 - \exp\left(h'^2\frac{\kappa}{c}t\right) erfc\left(\sqrt{\frac{\kappa}{c}t}\right)\right]$$

For simplicity, it is assumed that thermal conductivity, thermal diffusivity, latent heat of evaporation, and B(T) do not vary widely over the expected range of temperatures experienced.

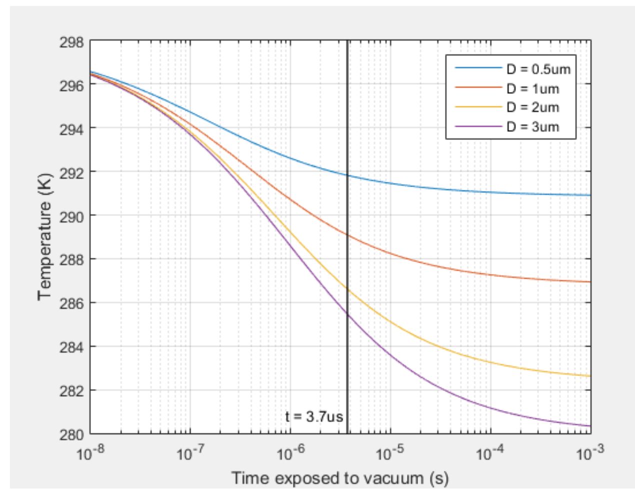

Figure 2-9 Evaporative cooling from the surface of the aperature as a function of time exposed to the vacuum.

The next step is to determine how long it takes for an individual molecule to cross the aperture and evaluate the above function to find the cooling factor. Using a Protochips liquid cell holder, typical pump speeds are 300 µL/hr, however dimensions of the cell can widely vary. A rough estimate of a rectangular channel formed from a 500 nm spacer and the 600 µm opening in the isolation layer under plug flow shows a linear flow rate of the liquid to be 27 cm/s, which transits the 1 µm hole in 3.7 µs. Figure 2-9 plots the bubble surface temperature as a function of time exposed to the vacuum, with the expected crossing time of an individual particle marked.

It is interesting to note that as the liquid cools the rate of evaporation decreases asymptotically to a particular minimum temperature above freezing, dependent on the hole size. For a 3 µm diameter hole, the total cooling is significant at nearly 16^0 C after ~70 µs, however for smaller 1 µm diameter holes, the cooling is only 9^0 C for the same duration. Regardless of the time taken to cross the aperture, there is no risk of the liquid layer freezing.

Flowing vs static liquid: In many liquid cell experiments discussed previously, the liquid was in a static configuration due to cell limitations. Using this holey cell, it would not be possible to operate with static liquid due to the evaporation causing eventual drying of the cell. Additionally, the flowing liquid reduces the surface cooling effect adding to the safety of the system, and as the next section will address, aids with the moderation of solvent concentrations.

Concentration changes: Until this point, all calculations have assumed the use of pure water. The addition of solvents modifies surface tension, gas flow rates, evaporation rates, and all other physical constants mentioned. In the case of very dilute solutions the change is minimal, but these parameters are worth recalculating for the safety of the instrument.

Evaporation of water will result in either evaporation of surface solvents, if they are volatile, or increased local concentrations of the solvents, if they are non-volatile. A volatile solvent is defined as one which evaporates at room temperature. Calculating the surface evaporation rate and solute diffusion rate for non-volatile solvents gives an estimate to the surface concentration changes. To calculate the diffusion of solvents, the generalized diffusion equation above is again modified by incorporating a solvent source at the surface, r=R.

$$\frac{\partial C}{\partial r} = \frac{1}{D}\rho_0(T)\sqrt{\frac{kT}{2\pi m}}\frac{1}{\rho_{liq}}\ (C) \qquad at\ r = R$$

$\rho_o(T)$ is the water vapor pressure as a function of temperature, which itself has a time dependence. Typical diffusion constants of small solutes are 1-3x10^{-5} cm^2/s, for example D = 1.5 x 10^{-5} cm^2/s for NaCl, resulting in a diffusion distance of 0.32 μm after 70 μs transit time of a large hole.

The evaporation rate of water is assumed to be equal to the effusion rate of water[60],

$$E = \frac{P_w}{\sqrt{2\pi m k T_s}}$$

where P_w is the vapor pressure of water, m is the molecular mass, k is the boltzman constant and T_s is the temperature of the water surface. Note that this is the same equation that was used for discussion of the probe mean free path. For simplicity, if the temperature change of the water is ignored and a constant upper bound of T = 300 K is used, an effusion rate of E = 139.8 mol/m^2s is found. Normalizing for the surface area of a 3 μm aperture and applying the ideal gas law with the

density of water vapor at 1.73×10^{-5} g/mL, accurate for pressures below 10 kPa, the water will be evaporating from the surface at a rate of ~3.3×10^{-3} m/s. Taking into account large hole diameters as with the ionic diffusion, a transit time of 70 μs is assumed and we find a 0.23 μm drop in surface level. Considering surface cooling effects lowers the evaporation rate, reducing the net surface drop. It is important to note that surface tension will compensate for the water level drop and prevent any physical change, but the equivalent volume of water will be lost, displacing the solutes.

The ionic diffusion distance of 0.32 μm is a similar order of magnitude to the surface level drop of 0.23 μm, and both are smaller than the aperture. Further calculations by Li Yang et al. show a surface ions concentration increase of 1.2-2.2x the initial concentration, which may be a significant amount for highly controlled experiments.

The results from this section show the viability of placing a small hole in the liquid cell membrane with compatibility to the extreme vacuum pressure. As discussed in the previous section, for thin liquid cell configurations the membrane plays a significant role in limiting liquid cell resolution. By forming a hole in the membrane, a viewing window for improved resolution over commercial liquid cells is realized.

2.5 Microfabrication

Previous sections have shown a wide variety of liquid cell designs, each with their own benefits and complications. In our research group, we have access to the liquid cell system commercialized by Protochips, but are limited by the choice of microchip designs for the formation of the liquid cell. To this end, we are motivated to fabricate custom chips through microfabrication techniques, with the techniques used summarized in the remainder of this section.

Microfabrication is a term used to describe creating devices or systems with a critical dimension on the scale of 1 μm to 100 μm. It is typically a 2-dimensional surface building technique, where a flat substrate is used with layers of material either added or removed to create 3-dimensional structures. Common microfabrication processes include material growth, physical metal deposition, wet chemical etching, dry reactive ion etching, and a patterning process known as photolithography. Each of these processes will be addressed in the following subsections. If the reader is well acquainted with microfabrication techniques, they are advised to continue their reading at section 2.6-Focused Ion Beam.

2.5.1 Photolithography

Photolithography, first developed in 1955 at Bell Labs[61] was invented for the purposed of decreasing the size of the electronic circuits. Since then, it has been widely applied and has become a standard and very important procedure in the fabrication of nearly all micro devices. Put simply, photolithography uses light to impress a surface pattern or feature onto a substrate, and create a predetermined design.

Photolithography can be analogous to using painters tape to protect or pattern a surface during treatments. Imagine wanting to pain half of a wall red. Tape can be used to cover half of the wall, and then red paint can be applied over the entire surface. Removing the tape afterwards will result in a perfectly straight edge to the red paint, without needing to be careful during the application of the paint. Photolithography works in a similar fashion, where a photopolymer, or photoresist (PR) is applied to the surface. Exposing areas of the PR to light will cause a change in the polymer which allows those areas to either become soluble, or insoluble depending on the type of resist used. Further exposing of a solvent will yield a surface which is geometrically patterned with the remaining resist, acting as the 'painters tape'. Deposition and etching surface treatments can then be applied, which will only affect the areas uncovered by the resist. This process can be easily visualized through Figure 2-10.

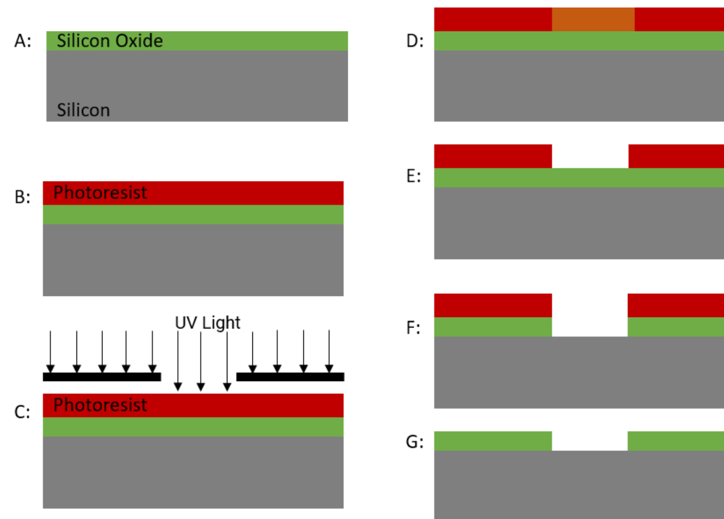

Figure 2-10 Process flow for photolithography. A: clean silicon substrate with silicon dioxide thin film. B: Deposition of photoresist. C: Using a black mask, selectively expose areas to light. D: Exposed photoresist changes solubility properties. E: Remove exposed photoresist in a developer solution. F: Process exposed surface, in this case removal of the exposed oxide. G: Remove any remaining photoresist.

Despite its wide use, photolithography is still a complicated process which requires many processing steps. Each step has specific parameters which must be optimized for each situation to ensure high quality patterning, and will be covered below.

Substrate preparation: Surface preparation for lithography is very important, because any defects on the surface may cause the adhesion of the photoresist to be poor, or the film thickness to be uneven resulting in challenges for further steps.

A standard surface cleaning procedure, first developed in the 1960's and published in the 1970's by Werner Kern at RCA laboratories is often used[62]. The so called 'RCA' clean has two primary steps, often termed SC-1 and SC-2 for 'standard clean 1' and 'standard clean 2' respectively. The SC-1 solution contains water, hydrogen peroxide and ammonia (H_2O:H_2O_2:NH_4OH) mixed at a ratio of 5:1:1 by volume. Hydrogen peroxide is standard 30 wt%, and ammonia is 27 wt/wt%. The SC-2 solution contains a mixture of hydrochloric acid, hydrogen peroxide, and water (HCl:H_2O_2:H_2O) mixed at a ratio of 1:1:6. HCl concentration is 37 wt%, and hydrogen peroxide is the same as before. The SC-1 solution rapidly attacks and removes organic contaminants through ammonia's oxidation and the basic properties of H_2O_2. It was also later discovered that SC-1 dissolves and regenerates the native Si oxide layer at approximately equal rates, which helps with the removal of contaminants and some metal complexes. The SC-2 solution is designed to remove alkali trace metals and metal hydroxides, both are often left as traces from other processing steps. Both the SC-1 and SC-2 solution are applied at 70-80 ^{o}C for 10-20 minutes [62].

While working with raw silicon surfaces, a third step is also included which is the removal of the native silicon oxide layer. This is done in hydrofluoric acid (HF) acid which preferentially etches the oxide layer, leaving the silicon surface unaffected[63]. This step is not crucial for lithography.

Another common cleaning step is a solvent clean, sometimes named the AMI (Acetone, Methanol, Isopropanol) clean[64]. This approach uses solvents to remove oils and organic contaminants, but has the risk of leaving new contaminants on the surface. It works very well for cleaning photoresist residue from surfaces. The clean procedure places the substrate in acetone for 5 minutes, followed by methanol to remove the contaminated acetone. Finally, isopropanol is used to remove the other cleaners, and is quickly air dried off using a nitrogen air gun to prevent drying of the solvents. Processing steps involving vacuum pumps, can introduce oils and polymer deposits on the surface which are generally cleaned using ozone, plasma, or further chemical cleaning[65].

Adhesion of photoresist to a surface is promoted by a dehydration bake to removes the presence of water from the surface. The wafer is placed on a hotplate above 120 ºC for 3-60 minutes[65]. The dehydration bake also thermally cracks -OH bonds present on the oxidized silicon surface, resulting in a hydrophilic surface, for further improved resist adhesion[66].

Resist adhesion promoter: In many cases a resist adhesion promoter is used. Silicon, silicon oxide and silicon nitride surfaces contain -OH terminated bonds which do not bond with photoresist. By binding a silane to the exposed hydroxyl, the surface becomes hydrophilic, preventing adsorption of water, and offering superior adhesion[67]. A common silane group is HMDS (hexamethyl disilizane) can be directly deposited as a solution to the wafer, and spun dry. If spin coating is used, a thick film is deposited which later releases ammonia and diffuses into the photoresist, crosslinking the polymers and preventing complete resist development[68] and possibly reducing resist adhesion.

Resist application: Photoresist is applied to wafers in one of two techniques: spin coating, and spray coating. To spin coat resist, the substrate is placed on a rotating chuck and photoresist is deposited on its surface. The wafer is spun at typical speeds of 2000-4000 rpm, using centripetal force to throw excess resist off. Counteracting this force is the viscous frictional forces of the fluid which act to hold the resist onto the wafer, resulting in a thin uniform layer.

The resulting film thickness is a function of many parameters, due to PR viscosity changing with the temperature of the wafer, ambient air and resist temperature, and humidity. The centrifugal force varies based on spinning acceleration, speed, and geometry of the sample. Calculating the final thickness of the resist based on these parameters can be very complicated[69]. Approximately 95-98% of the initial resist is immediately removed, and the final thickness becomes a balance of the viscosity of the remaining thin film and the spin speed. It is calculated that the final resist thickness is proportional to the viscosity to the 0-4-0.6 power, and spin speed to the -0.5 power [69].

In practice, a spin-speed curve is experimentally determined for each photoresist. For most commercial resists, a spin speed can simply be chosen from the curve to get the desired thickness. The lower limit on spin speed is typically set around 100 rpm, as these speeds are harder to control and harder to produce uniformity. The upper limit of spin speed is limited by the turbulent air flow around the outer edge of the wafer, also limiting uniformity.

A final note about photoresist application is that along the edge of the wafer a third force comes into play: surface tension. The surface tension creates an additional inward force preventing expulsion of resist and resulting in an edge bead of material[70]. The edge bead will have significantly increased thickness compared to the rest of the surface and will prevent complete contact with the exposure mask, reducing feature resolution as discussed in further sections. The edge bead can be removed by controllably spraying solvent around the wafer edge, removing the photoresist around the outer 1-2 mm of the wafer.

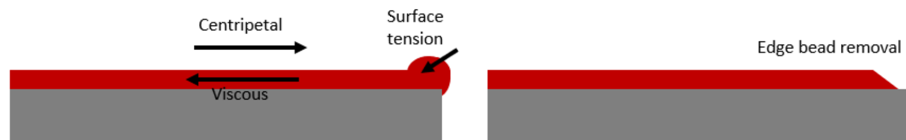

Figure 2-11 Force balance during spin coating, and edge bead removal.

Soft bake: Soft baking serves 4 very important roles. The bake itself is to remove remaining photoresist solvents, which is typically present at 20-40 wt%. Removal of the solvent causes: reduced film thickness; improved resist adhesion; improved resist stability; and prevention of bubbling from N_2 gas escaping during future processing[65,66]. Removal of the solvent solidifies the resist, reducing sticking of the wafer to the mask, diffusion after exposure (resulting in dark erosion, see development section), and reduces the resists vulnerability to contamination.

In the event a soft bake is too short or cool, the above factors become problematic. Baking at excessive temperatures or durations decomposes the photoactive compound within the resist, reducing the development rate and increasing dark erosion. A typical soft bake is ~100 ^{o}C for 1 min/µm of film thickness on a hotplate, but will vary based on resist and substrate material.

Exposure: The alignment and exposure of the photoresist is what allows surface patterning to be achieved. The essence of this step is that the photoresist contains a photoactive compound (PAC) which, when exposed to light, changes chemical properties. There are two primary types of resists: positive diazonaphthoquinone based resist, which when exposed to UV light converts to a carboxylic acid soluble in basic developer solutions, and negative resists, where UV exposure results in insoluble cross-linked polymers[71]. A third type of resist named an image reversal resist also exists, which may act as a positive or negative resist. The polymer chemistry of photoresist is quite complicated and will not be covered in detail here. In general, negative resists contain a much more robust and stable support resin, yielding higher chemical resistance and more robust film

tolerances of the final film[72]. Negative resists have high sensitivity to exposure because upon absorbing a photon, the PAC cross link and produce highly reactive intermediate chemicals which can trigger a chain reaction of further cross linking. The chain reactions lower the maximum image resolution compared to positive resists.

To create a geometric pattern on a surface, an optical mask with the desired pattern is made which contains transparent and opaque sections to project its pattern onto the substrate. The mask is made from a glass plate with high transmission to UV wavelengths, and is coated by a highly absorbing material such a chromium[73]. A cheaper, lower resolution is to screen print ink onto a transparent sheet, in a similar fashion to overhead projector screens. This may cause imperfections in the transparent regimes, pinholes in the opaque regimes, and deterioration with use, but they provide a much cheaper alternative for low resolution rapid prototyping.

Once the mask is made, there are several approaches taken to project the light source onto the wafer, including contact, proximity, and projection methods. In fact, screen writing approaches may also be used which do not require a mask and instead serially write the desired pattern. A discussion of these approaches is not included as the fabrication facility available simply uses contact printing, where the mask is placed directly on the wafer surface, as shown in Figure 2-12.

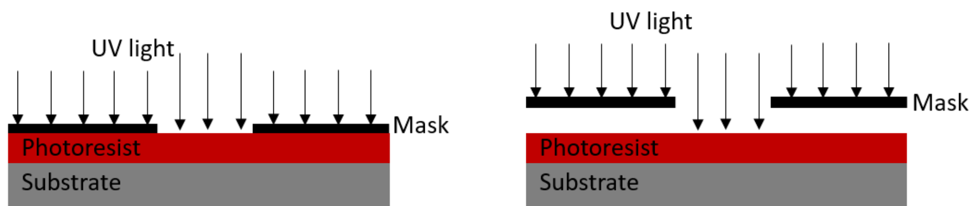

Figure 2-12 (Left) Contact-mask exposure. (Right) Proximity- mask exposure

Contact lithography resolution is typically limited by the optical system and approaches the wavelength of the light radiation (~365 nm I-line printing). This can further be limited by optical inaccuracies and lens aberrations. In this work the limiting resolution factor is on the printing of the screen masks at 10 µm minimum feature size, and thus a further discussion will not be included.

A principal factor in the exposure of the resist is the correct cumulative energy of photons deposited into the resist. For a positive photoresist, if exposure is too high a bleeding effect occurs which effectively exposes the areas under the opaque regions, resulting in dark erosion. Dark erosion is where the unexposed areas are removed by the developer solution. Too low of an

exposure will not change the polymer structure through the entire resist, leaving a residue of insufficiently exposed PR after development[74].

Each photoresist specifies a total optical energy to be applied per unit volume of resist. These specific energy levels can be difficult to calibrate for, due to back reflections from the wafer and any deposited films reflecting the light back through the resist. Upon exiting the photoresist, it may again reflect into the polymer. Repeating this cycle may result in standing waves of the light within the film, drastically over or under exposing the resist[65]. The resultant alternating high-low exposure pattern leaves a sinusoidal edge to the developed resist profiles and total exposure may be difficult to calculate. To this end, lithography exposure rates are typically found experimentally (within bounds) for each application, as various substrates, thin films, and resist thickness can have widely different results.

Post exposure bake: The primary purpose of the post exposure bake is to remove the effect of standing waves in the developed resist. The post exposure bake (PEB) allows for diffusion of the photoactive compound, to reduce the effect of standing waves during resist exposure and yield vertical sidewalls. Excessive temperatures can damage the resist similarly to soft baking.

Development: The photoresist development selectively removes soluble photoresist from the surface. Depending on the photoresist used, a specific developer solution is applied. Typical developers are aqueous base solution such as TMAH (tetramethyl ammonium hydroxide) or sodium hydroxide[75]. Immersion development systems submerge the sample entirely under the solvent for a set amount of time, often under agitation to improve uniformity[65]. Spin development is like spin coating, with the developer either drop deposited or spray coated. Spin processes require a much lower volume of developer solution if properly controlled.

Hard bake: The last, optional, step to photolithography is to hard bake the final resist, removing any remaining solvent, water, and gas bubbles within the resist for improved chemical, thermal and structural properties. This makes the resist more stable in future chemical etchants and vacuum processes. At temperatures of 140-150^{0} C, chemical bonds are formed between the resist and the substrate for improved adhesion. Hard baking may result in cracks through the photoresist due different thermal expansion coefficients of the resist and substrate, so it is not always a recommended procedure[76].

Stripping the resist: Once the resist is in place, either an etching process, deposition process, or ion implantation method is applied to the exposed surface. Afterwards it is desirable to remove the photoresist from the surface for future processing, with any of the solvent clean methods listed in the substrate preparation section, such as AMI or SC-1 cleaners. Plasma cleaning and oxygen plasma ashing may also be incorporated for monolayer contamination removal.

2.5.2 Wet chemical etching

With the ability to use photoresist to create micro sized patterns on wafers, the next step is processing which can be applied to the now patterned surface. Three categories of processing exist: top down etching, bottom up growth, or ion implantation (which will be irrelevant to this thesis's work, and will not be discussed). Etching can be done in one of two different approaches: wet chemical etching, and dry reactive ion or plasma etching.

Etching requires understanding of several key parameters, namely etch rate, etch rate uniformity, selectivity, and isotropic vs anisotropic qualities. The etch rate is how quickly material is removed from the surface, expressed in units of vertical velocity. The etch rate uniformity refers to changes in the etch rate between wafers, location on the wafer, or changes over time. Uniformity is expressed below[77], where R_{high} and R_{low} are the highest and lowest etch rates recorded.

$$U = \frac{R_{high} - R_{low}}{R_{high} + R_{low}}$$

Selectivity is the ratio of the etch rates between multiple materials for a single etchant. For example, SiO_2 as a mask for Si when exposed to HF acid. The etch rate of SiO_2 is ~26 nm/min[63] whereas Si is not etched at all, resulting in a 1:∞ selectivity. Photoresist is often a suitable etch mask and with sufficient selectivity; however, it is also common to use a layer of SiN or SiO_2 with higher selectivity, depending on the etchant.

Etch anisotropy refers to the ratio of vertical to horizontal etch rates, or how uniform the geometric etch profile is between depth vs width. The degree of anisotropy is defined as

$$A = 1 - \frac{R_{horizontal}}{R_{vertical}}.$$

An isotropic etch has A = 0, with equal vertical and horizontal etching. Anisotropic etches have A > 0, and purely anisotropic etches have A = 1. Purely anisotropic etches result in a vertically side

walled hole. Isotropic etching results in an undercutting profile compared to the etch mask due to the presence of lateral etching, shown in Figure 2-13.

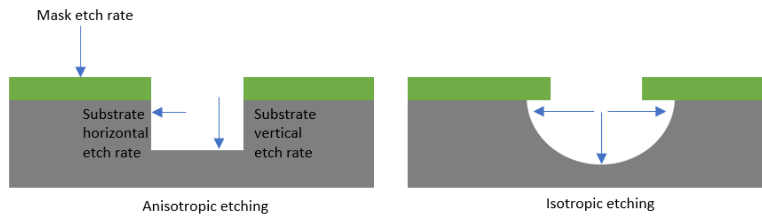

Figure 2-13 Anisotropic vs isotropic etching

For wet chemical etching, the mechanism for material removal is the following: transport to the surface; chemical reaction of the etchant; and waste product transport away from the surface[78]. The etch rate is typically limited and controlled by temperature, concentrations, and chemicals used. Shown in Table 2-2 is a list of common etchants for Si, as well as etchants of other materials to be used in the fabrication of the liquid cells.

Etchant Descriptions for Table 2-2:

- **KOH/TMAH/EDP** – See text for etching details.
- **HF** – (Hydrofluoric acid) 10:1 H_2O:HF. HF strongly attacks oxide layers and certain metals, leaving Si relatively untouched.
- **Ti etch** – 20:1:1 H_2O: $H_2O_{2\,(30\%)}$: $HF_{(49\%)}$.
- **CR-7** – $(NH_4)_2Ce(NO_3)_{6\,(9\%)} + HClO_{4\,(6\%)} + H_2O$. Mixture of Ceric ammonium nitrate and perchloric acid, at room temperature. Etch mechanism follows: $3Ce(IV)(NH_4)_2(NO_3)_{6\,(aq)} + Cr_{(s)} \rightarrow Cr(III)(NO_3)_{3\,(aq)} + 3Ce(III)(NH_4)_2(NO_3)_{5\,(aq)}$. The Ce^{+4} is reduced to Ce^{+3}, while oxidizing the Cr to Cr^{+3}, forming a soluble product. Perchloric acid acts as a stabilizer by ensuring acidic conditions. Does not attack organic compounds, gold, or Si complexes.
- **Dilute aqua regia** – 3:1:2 $HCl_{(37\%)}$:$NHO_{3\,(70\%)}$:H_2O. Mixture of hydrochloric acid and nitric acid. Standard aqua regia does not include water dilution. Mixing of the acids raises solution temperature to ~30^0 C, where it etches noble metals. The nitric acid oxidizes metals, and the chlorine ions form soluble products, with typical reactions: $Au_{(s)} + 4H^+ + NO^-_3 + 4Cl^- \rightarrow AuCl_4^-{}_{(aq)} + NO_{(g)} + 2H_2O$. Does not affect organic compounds or Si.
- **Au etchant** – $I_{2\,(5\%)} + KI_{(10\%)} + H_2O_{(85\%)}$. Specifically designed to etch gold, without attacking photoresist or other common MEMS materials. Etching mechanism is $2Au_{(s)} + I_{2\,(aq)} \rightarrow 2AuI_{(aq)}$. The KI is added to increase solubility limits of reactants and products, allowing for higher concentrations and etch rates, and helps with diffusion of products.
- **Piranha** – See sample surface preparation section for further details. 50:1 $H_2SO_{4\,(96\%)}$:$H_2O_{2\,(30\%)}$, heated to 120°C, attacks organic compounds. May be used without heating, as mixing the solution is a self-heating step.

- **Acetone/Methanol/Isopropanol –** Rapidly attacks photoresist and organic contamination. Acetone evaporates very quickly, and may leave surface residue, so it is often removed by methanol and/or isopropanol.
- **SU-8 -** is a negative photoresist which shows very high chemical stability. There are no known chemical etchants, however some solutions may cause swelling or delamination.

Table 2-2 Etch rates in nm/hr for various etchants. Rates are determined from[63] unless otherwise noted. Any cells left empty are because they are irrelevant to the proposed fabrication flow, or no data was found. ✓ represents an etch that works, but the rate is unmeasured. S means the etch rate is very slow, or close to zero. * means a soft unknown material remained after exposure.

Material: **Etchant:**	**Si (100)**	**Thermal (Wet) SiO_2**	**Stoichiometric LPCVD SiN**	**Si Rich LPCVD SiN**	**Au**	**Cr**	**Pt**	**Ti**	**Ni**	**Microposit Photoresist**	**SU-8**
KOH (30 wt%, 80^{0C})	78590[79]	434[79]	0	0	0	4.2	0	*	0	✓	S
TMAH (optimal parameters)	60000[80]	1644.5[80]	0.102[81] -SiN type unknown							Fast	S
EDP - ethylene-diamine-pyrocatechol	60000[82]	120[82]	~8[83] -SiN type unknown		0	0					S
Phosphoric Acid	0.17	0.18	4.5	2.7	0	100	0			120	S
HF	S	✓	1.1	S	S	S	0	1100	0	S	S
Ti etch	S	12	0.99	S	0	0	0	1100		<0.5	S
CR-7	0	0.02	S	0	0	170	0	<2	1.7	0	S
Dilute aqua regia	0		0	0	680	0	3.6	<0.5	100	0	S
Au etchant	S	S	S	0	660	0	<2		0	0	S
Piranha	0	0	0	0	0	>16	<3	240	380	>92000	S
Acetone	S	0	0	0	S	S	S	S	S	>176000	S
Methanol	S	S	S	0	S	S	S	S	S	>36000	S
Isopropanol	S	S	S	0	S	S	S	S	S	>1000	S

2.5.3 Wet etching of Silicon

Si wet etching has been very extensively studied for integrated circuit and microchip fabrication, and there are several common etchants and masks available. Table 2-2 shows the three most common wet chemical etchants used: potassium hydroxide (KOH), tetramethylammonium hydroxide (TMAH), and Ethylene Diamine Pyrochatechol (EDP). All three etchants show strong selectivity towards SiO_2, allowing it to be a masking material for short etches, and very strong selectivity to SiN_x. Wet chemical etching displays anisotropic etching according to the crystal plane orientation of the exposed Si.

Crystalline Si follows a diamond cubic structure, which is best described as a 'two interpenetrating face centred cubic,' or a 'face centred diamond cubic lattice', where the {111} plane has much higher density than {110} and {100} planes. The {110} and {100} planes each have 2 bonds into the surface, and 2 dangling bonds per unit cell, whereas the {111} planes have 3 bonds and only 1 dangling[84], as shown in Figure 2-14. The etching of Si is reaction rate limited, meaning the denser packed {111} plane has a significantly lower etch rate, yielding the etch profiles shown in Figure 2-15. The etch rates between the planes differ by over 100x, whereas this explanation only accounts for a factor of 2 difference. A full discussion of the etch mechanism was presented by Helmut Seidel et al. in 1990[85], which presents that the primary dissolution product for all etchants is $Si(OH)_4$, and the anisotropic nature is due to variations in the bond energy between surface Si atoms and their backwards bonds, as a function of crystal orientation. Further discussion of the anisotropic structure is beyond the scope of this background.

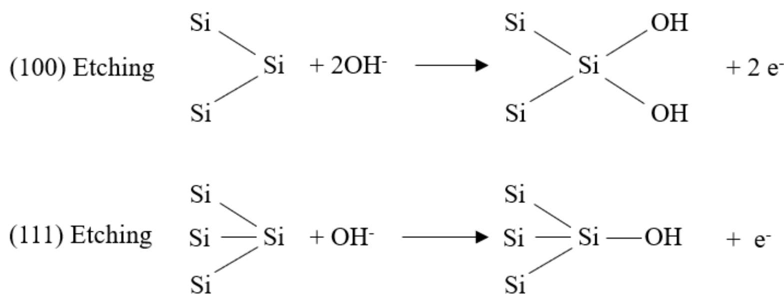

Figure 2-14 Chemical structure and suface binding for OH based etching of Si crystal planes.

Table 2-3 Approximate etch rate selectivities for common Si etchants. Data for oxide/nitride selectivities derrived from Table 2-2

Etchant	Orientation	Selectivity	{100}:SiO_2 selectivity	{100}:SiN selectivity
KOH	{111}:{110}:{100}	1:~600:400[83]	1:~200	1:∞
TMAH	{111}:{100}	1: ~30[86]	1:5000	1:50000-∞
EDP	{111}:{100}	1:35[83]	1:3000	1:7000

Interestingly, the type of etchant changes the relative etch rate of each crystal plane, shown in Table 2-3. KOH has the highest selectivity, and EDP and TMAH show similar rates. Another oddity is that KOH etches the {110} plane faster than {100}, whereas EDP will etch the {110} planes slower than {100}, resulting in less undercutting from and EDP etch[83,87].

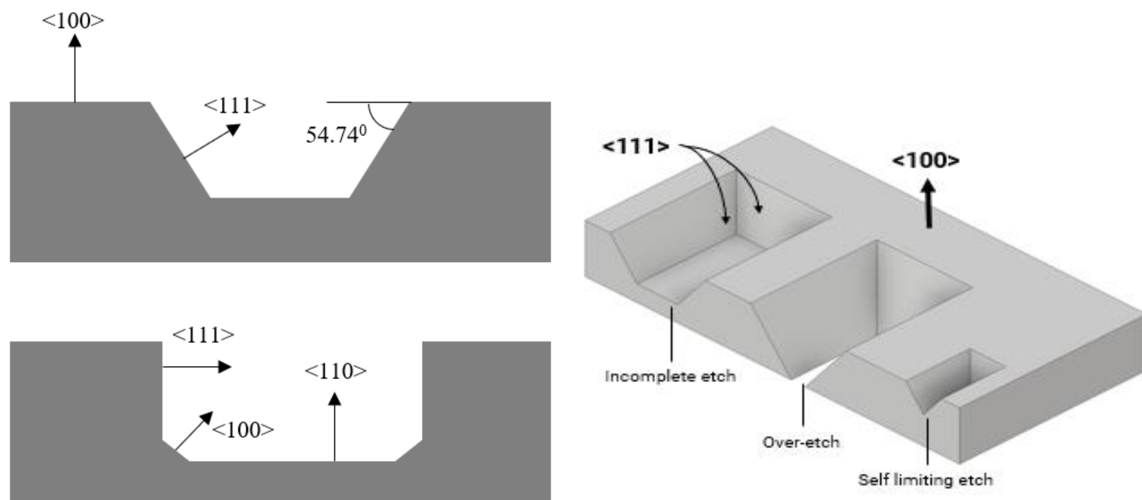

Figure 2-15 Crystal plane wet etching of Si. (Left) Typical etch profiles from <100> and <110> oriented Si substrates. (Right) Effects of mask hole size, and over/under etching of the substrate. The angle of the etched sidewall is due to the crystal plane orientation.

KOH is the fastest wet chemical etchant for the {100} crystal planes of Si, and shows the highest selectivity towards other planes. Despite this, KOH is often avoided as it introduces highly mobile potassium ions into the Si or SiO_2 bulk, which influences the electrical properties and is not ideal for microchip manufacturing.

The etch rates of KOH and TMAH are strongly dependent on their concentrations and temperatures. For both etchants, low concentrations (<20 wt%) provide insufficient OH^- ions and net low etch rates. Increasing the concentration will gradually improve the etch rate; however, at high etchant concentrations there are insufficient water molecules available which slows the etch

rate, as seen in the governing reaction: $Si + 2 H_2O + 2OH^- \rightarrow Si(OH)_4 + H_2$. Through experimental means, etch rates have been maximized for ~4 wt% solutions of TMAH[80] and ~20-30 wt% for KOH, depending on etch temperature[88].

H_2 bubbles are generated as by-products to the overall reaction. The removal of these H_2 bubbles from the surfaces plays a significant role in determining the etch quality, or smoothness of the final Si surface because their formation acts as a localized hard mask. Bubble formation is dictated by the hydrophobicity of the exposed surface, with high KOH wetting permitting only small H_2 bubbles to form, reducing surface roughness of the etch. This is maintained by high (~60%) solution concentrations, at the cost of slower etch rates[89].

KOH etch rates are strongly affected by temperature, attributed to the increased mobility of reactants and products and the access to the surface for etching. It has been experimentally shown that the etch rates for both TMAH and KOH are directly proportional to the inverse of the applied temperature[88], and limited by the solution boiling point of 100-130 ^{0}C depending on concentrations. Approaching the boiling point introduces evaporated gas species to the solution, so practical temperatures are kept below ~80 ^{0}C.

IPA inclusion in the KOH etch reduces the etch rate of the {110} plane, without significantly impacting the etch rate of the {100} plane[84]. It is generally accepted that the IPA masks the surface of the Si limiting access to etchants and removal of products, not directly forming any chemical bonds in the process[90]. This explanation is further supported due to the enhanced etch rate differences seen while using lower concentration KOH solutions. IPA modulation enhances the high etch selectivity and is often used to create complex structures with facets along the (110), (331), (311) and (211) planes. For 5 M (23 wt%) solutions, the IPA significantly improves surface quality for (100) and (110) planes, whereas higher concentration solutions of 10 M (46 wt%) show nearly no change. It is important to note that because the IPA does not chemically react with the surface, the concentration doesn't matter, simply the availability in the solution. As IPA has a lower vapour pressure than water, it evaporates more rapidly and requires replacement throughout the duration of long etches[84].

TMAH etch rate is strongly dependant on concentration and temperature. The optimized concentration for TMAH is much lower than that of KOH for fast etch times, but a similar relationship was found relating processing temperatures to etch rates[80]. TMAH is advantageous to

KOH for CMOS processing as it does not introduce highly mobile potassium ions into the bulk, and it is also a non-toxic chemical unlike KOH and EDP. TMAH has worse selectivity than KOH which yields a higher degree of undercutting[86].

The inclusion of IPA has been studied for TMAH etching. Following similar processes as those described for KOH, the IPA improves etch selectivity and reduces undercutting of the mask. As with KOH, high concentrations of etchants (~25% TMAH) showed very smooth surfaces, less than 60 nm mean roughness on the (100) plane, and lower concentrations resulted in formation of small hillocks. At these low concentrations, the IPA inclusion enhances the size of the hillocks[86] without affecting number density, which is consistent with the understanding that the IPA reduces etch rates of the densely packed crystal planes. For high TMAH concentrations, the IPA further smoothens the surface, which agrees with the theory of slower etching producing a more uniform surface, and is further enhanced by IPA masking. In general, KOH produces much smoother surfaces than TMAH[88]. An additional study showed that for both TMAH and KOH, higher etch temperatures produce improved surface roughness[91].

Due to the much higher selectivity of TMAH to oxide films than KOH, the native oxide which forms on the surface of the wafers is enough to strongly inhibit the etching. An oxide removal step is critical for TMAH processing.

EDP is more complex than KOH and TMAH, with overall governing reactions described by[82]:

$$2NH_2(CH)_2NH_2 + 6H_2O + Si \rightarrow Si(OH)_6^{-2} + 2NH_2(CH_2)_2NH_3^{+} + 2H_2$$

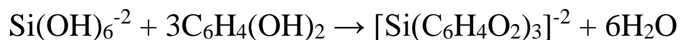

$$Si(OH)_6^{-2} + 3C_6H_4(OH)_2 \rightarrow [Si(C_6H_4O_2)_3]^{-2} + 6H_2O$$

EDP is advantageous because it does not introduce mobile potassium ions, the selectivity to SiO_2 is significantly higher than KOH, and it does not attack most metals. EDP etching often leaves a white residue comprised of SiO_2 and reaction product. The reaction products have a low solubility limit within the solution causing precipitation out of solution, which is partially avoided by preparing fresh solutions for each use or replacing the solution during long etches, adding to processing cost. Controlling the solubility of the etch products is done by modifying the temperature of the solution, and further steps may limit the formation of the residue, however once formed it cannot be dissolved without HF[91].

2.5.4 Dry chemical etching

Dry etching is an alternative to wet chemical etching where the etchant is a reactive ion or plasma in place of an aqueous solution. In general, dry etching allows for higher resolution, has higher anisotropy, a lower degree of undercutting, improved process control, and uses significantly lower volumes of corrosive and cleaning materials, making it more environmentally friendly and economical for batch processing, all at the cost of slower etch rates and worse material selectivity. Unless otherwise mentioned, the following discussion is adapted from work by K. Nojiri, 2015[92].

Dry etching is a process where gas particles are excited to higher energies becoming a very reactive plasma, which interacts with the sample to form gaseous by-products and 'etch' the surface. Typical processing gasses employ fluorine based CF_4 and SF_6 chemistries and use one of three methods: chemical etching, physical etching, or ion-enhanced etching.

Chemical plasma etching is a process where highly volatile neutral species, or 'free radicals', chemically react with the surface to form volatile compounds which are transported by processing gasses. Chemical etching is described by 5 steps: diffusion of reactant gas to the surface, absorption of the reactant, chemical reaction with the substrate forming gaseous products, desorption of gasses, and diffusion of the products from the surface. A common example in the etching of Si is the use of CF_4, and is governed by 2 chemical reactions: $e^- + CF_4 \rightarrow CF_3 + F^* + e^-$ and $4F + Si \rightarrow SF^4$.

First a plasma is formed from CF_4, producing the free radicals F^* and CF_3. Note the superscript asterisks is used to denote highly reactive, electrically neutral ions. The free F^* react to form SiF_4, which has a high vapor pressure and will readily desorb and diffuse away from the surface.

Chemical plasma etching selectivity is tuned by incorporating additional processing gasses. Incorporation of H_2 gas promotes $F^* + H \rightarrow HF$, reducing the F^* content and reducing the formation of SiF_4. SiO_2, which has lower Si content than pure Si, will have a proportionally higher etch rate as a result. Including O_2 to CF_4 promotes the formation of F^* radicals and Si etch rate by the combination of O with CF complexes, $O + CF_x \rightarrow COF_{x-1} + F^*$. This reaction will reduce the recombination of CF_3 with F^* radicals, further improving Si etch rates. High incorporation of O_2 promotes $Si + O_2 \rightarrow SiO_2$ to occur more readily, causing formation of SiO_2 and reducing the overall etch rate and selectivity[93].

Physical plasma etching, or sputter etching is a non-selective, directional, non-chemical etch method. As the name implies, it is a physical method where heavy Ar^+ ions are used to bombard the sample and physically dislocate the atoms from the sample. It is applied for almost any substrate[77], but is often coupled with chemical etching to form ion enhanced etching.

Ion enhanced etching, or reactive ion etching (RIE) combines both physical and chemical etching to result in an improved system, which improves on the etching mechanism of both chemical and physical etch methods by more than the linear superposition. RIE yields highly anisotropic etch profiles and high chemical selectivity and is the most widely applied form of plasma etching.

The exact mechanism of enhanced etching by RIE is not fully understood, but several theories apply. Most commonly accepted is the 'hot spot model,' where ion bombardment causes local high temperature increases boosting the chemical etch rate of the radicals. Other theories show that ion bombardment removes etch by-products such as carbon deposition or contaminants from redeposited photoresist, and physical damaging of the surface allows for improved access of chemical etchants. The ion-assisted etching provides a directional etch which is orders of magnitude faster and more directional than the indirect chemical etch.

Although RIE creates anisotropic etch profiles, it is limited by the chemical anisotropic sidewall etching, preventing very high aspect ratio trenches. A solution to this problem is a sidewall protection process, the most common of which is know as the Bosch process as developed by Bosch Inc.[94], which is a form of deep reactive ion etching (DRIE). During this process the sidewalls of the etched hole are coated in a polymer which limits or prevents chemical sidewall etching.

Starting with a lithographically patterned substrate, an RIE step using CF_4 or SF_6 is performed which opens a trench in the substrate. A protective polymer is deposited to the surface using C_4F_8 gas, conformally coating the substrate and the trench sidewalls. The RIE etch is repeated, removing the polymer at the bottom of the trench followed by the underlying substrate, while the trench sidewalls are protected from the chemical plasma etching. Repeating this process provides high aspect ratio anisotropic etches, for deep trenches.

Each cycle of a Bosch process typically yields 0.5-1 µm etch depth in Si and consists of ~10 s of deposition and ~15 s of etching. Including the time taken to switch gases, the overall process yields etch rates on the order of 0.5-2 µm/min of vertical Si etching. Many experimental issues affect the

outcome of a Bosch process, as outlined by the University of Alberta nanoFAB facilities[95]. Importantly, each etch is unique and shows non-linear scaling. A short etch applied for a larger number of cycles does not linearly scale etch depth due to changed active surface area on the wafer and aspect ratio dependant etch rates. For exposed surface areas greater than 20-30%, the etch depth has poor radial uniformity, likely due to access of processing gasses to the abundantly exposed surface. There is poor vertical etch rate uniformity for different width trenches along the substrate. Further complicating the process, the etching of the initial masking layer introduces by-product gasses and alters etch rates and uniformity. Sample heating causes the protective polymer to desorb, and buried layers cause 'pedestalling'. Pedestalling is where the vertical etch rate is slowed due to changed material properties, but the horizontal etch rate at interface has not slowed, resulting in sidewall etching of the upper material and an inverted T shaped etch profile.

Each of these process issues are indirectly controlled and mitigated through mask design, gas flow rates, total and partial gas pressures, etch and deposition time, power, and the ambient temperature of the gasses, chamber, and sample[96]. In the experimental methods, reasoning behind why the DRIE process was not used is presented, and thus further background is not necessary.

RIE is often used for patterning of SiN_x or SiO_2 films in semiconductor manufacturing, using various gas compositions, including CF_4, C_2F_6, CHF_3 and SF_6, with additives such as O_2, N_2 and H_2[97–101]. The simplified chemical reaction which governs the etching process is $Si_3N_4 + 12F \rightarrow 3SiF_4 + 2N_2$, where both reaction products have high vapor pressure and are transported away as gasses. Etch rates are influenced by growth mode (LPCVD or PECVD) of the nitride, and the gas type, with CF_4 etching an order of magnitude faster than C_2F_6, which in turn is an order of magnitude faster than CHF_3. This relationship is likely attributed to deposition of a carbon-silicon layer which occurs during the second two processes[101].

Regarding CF_4 etching of nitride films and oxide films, incorporation of O_2, at a ratio of 15% of the CF_4 pressure increases the etch rate by a factor of 2 and the presence 5% N_2 improves the etch rate by another factor of 7, for constant power and CF_4 gas flow rate[98]. O_2 concentrations higher than 20% begin to reduce etching rates due to the formation of SiO_2 on the surface. This effect was not noted while etching SiN_x. During the etching of SiO_2 the etch rate increased to a factor of 3 from 15% inclusion of O_2, whereas incorporation of N_2 gas did not have any effect. In all cases the enhanced etch rates were not attributed to increased F^* concentrations, but due to the formation of

NO gas. The gas removes N from the surface of the sample, in a very simplified form: $N_{surface}$+ NO_{gas}→ N_2O_{gas}; $N_{surface}$+ NO_{gas}→ $N_{2\ gas}$+ $O_{surface}$.

Many similarly detailed investigations of processing parameters for bulk Si, and nitride and oxide films have been conducted. From all results, optimal conditions yield SiN_x etch rates on the order of 100 nm/min and oxide etch rates up to 50 nm/min. Selectivity towards Si and photoresist is poor, typically 1:2 and 1:1 respectively, with some tuneability.

2.5.5 Growth and deposition methods

In contrast to wet and dry etching methods, common micromanufacturing approaches include bottom up processing through growth and deposition via thermal oxide growth, physical deposition of metals and thin films, or chemical growth from a plasma or gas source. These techniques are characterized into two categories: Physical Vapour Deposition (PVD) and Chemical Vapour Deposition (CVD). CVD introduces gas phase reactants which chemically react on the surface, and PVD methods physically produce the required atoms as a gas phase which condense to the wafer surface. Other deposition approaches include electrochemically deposited films through the reduction of ions to an electrode, or spin on processes such as that for PR. The following discussion on deposition methods is adapted from Chapter 9 of Silicon VLSI Technology, a textbook by J. Plummer et al, 2000[102], unless otherwise noted.

CVD of films is done through introduction of gasses into a chamber which either react with the surface to deposit a film or react with each other to produce a deposit on the film surface. During Atmospheric Pressure CVD (APCVD), gasses are introduced at atmospheric pressure, the chamber sides are left at room temperature and the wafer is heated, promoting deposition to the wafer. APCVD is commonly used for epitaxial SiO_2 and Si growth but is less common than Low Pressure CVD (LPCVD) and Plasma Enhanced CVD (PECVD).

LPCVD introduces gasses at low temperatures into a chamber surrounded in resistive heating coils. The heating coils create a 'hot wall' chamber which generate very uniform heat profiles, providing energy to the gas to induce chemical deposition on the wafer surfaces. There are 7 main steps for the operation of any CVD system:

i. Reactant transport into chamber
ii. Reactant transport to wafer surface from main gas stream. Typically, must pass a boundary layer formed by other reactant and by product gasses

iii. Reactants adsorbed to wafer surface
iv. Surface reactions: chemical decomposition of gasses, surface migration of atoms towards active sites, etc.
v. Byproduct desorption
vi. Byproduct transport back through the diffusion layer to the gas stream
vii. Byproduct transport away and out of the chamber

Without presenting the derivation in this thesis, the growth rate of the film is given by

$$v = \frac{k_s h_g}{k_s + h_g} \frac{C_G}{N}$$

where the growth velocity ν in cm/s is given by the inverse addition of the mass transfer coefficient h_g in cm/s and the surface reaction rate κ_s, times the relative concentration of the reactant gas, given by the gas concentration C_s divided by total number of incorporated atoms N per unit volume, also called the film density. From this equation and the seven primary steps of CVD growth that changing physical parameters of the deposition system, mainly temperature, can limit the CVD into two separate types: surface reaction rate limited, and mass transport limited.

Mass transport rate is not affected much by temperature due to pump systems dominating the gas diffusion rates; however, the surface reaction rate is strongly influenced, with high temperatures reacting exponentially faster than in low regimes. At high temperatures the deposition rate becomes mass transfer limited, and low temperatures are reaction rate limited, with the cross over temperature being controlled by pressure, gasses composition, wafer layout, flow rates, etc.

For surface rate controlled processing, lowering the temperature to reach this regime also lowers the deposition rate, which is undesirable for bulk processing. This introduces LPCDV, where the reactant gasses are placed at low pressures around 0.25-2 torr, significantly dropping the mass transport rate and extending the regime of surface controlled reactions. The low gas pressure improves the diffusion of gasses through the boundary layer by decreasing gas phase collisions, reduces the amount of carrier gas required, and reduces the number of gas phase reactions which result in nonuniform precipitates to fall to the wafer surface.

One problem common to LPCVD and APCVD is the use of high temperatures which may affect pre-deposited surface structures. For example, an Al film has a melting point of 660^0 C, limiting future processing temperatures to under 500^0 C. For LPCVD and APCVD in surface controlled operation, a significant drop in deposition rate occurs. PECVD, or Plasma Enhanced CVD, uses a

high energy plasma is used in place of thermal excitation of the reactant gasses allowing deposition temperatures to drop as low as room temperature without reducing deposition rates. The plasma is typically formed through an applied electric field across the entire reaction chamber, with the wafers placed face up to allow deposition from the ionized gasses.

The plasma generated in PECVD systems can form many complex ionized species of the reactant gasses, including ionized, excited, or neutral molecules (or atoms), ionized and excited dissociated molecules, broken up from the original parents, and other free radicals. Due to the wide variety of plasma produced species, there are numerous reactions which may take place and dominate a deposition. If well controlled, this can be used to form non-stochiometric N or O rich silicon films, high incorporation of dopants and H_2, O_2 and N_2 gasses, and tuning of film stress.

PVD methods rely on static adhesion forces to deposit films rather than chemical surface reactions, allowing for a large variety of materials onto nearly any substrate. Atoms or molecules of the desired material are produced from a ‘target’ which is either heated to induce species evaporation or bombarded with ions from a plasma to knock off surface atoms. The generated atoms are transported through a vacuum chamber and condense onto surfaces they contact, forming the desired thin film. The vacuum chamber is necessary to reduce collisions of the generated atoms with gaseous atoms and ensure deposition to the desired surface.

For evaporation systems, a chamber pressure around 10^{-5}-10^{-6} torr is used, and a source material is heated through either resistive heating elements or an electron beam, which heats a ceramic crucible holding the target metal, evaporating atoms with some distribution profile, which then diffuse and condense on the substrate. By mapping the distribution profile of the evaporated atoms, a spherical shaped holder is used to ensure uniform coverage onto multiple wafers.

Evaporating methods have several main disadvantages which have reduced their use. Low vapour pressure metals and all alloys are very hard to evaporate with high control. Alloys will have each constituent evaporate at different temperatures and rates, yielding deposited films which do not match the initial alloy. Additionally, there is no surface cleaning available inside the reaction chamber, and the low chamber pressure causes emitted species to travel in straight lines leading to high shadowing effects from surface topography.

The most common approach to PVD is the sputter deposition system, which uses a higher vacuum than evaporation deposition, ~1-100 mTorr. A sputter deposition system acts similarly to PECVD. A high energy plasma is generated in an inert gas through an applied electric field between the target material as the cathode, with a metal plate as the anode. For conducting targets, a DC voltage is applied, and non-conducting targets require AC voltages to prevent charge accumulation. Using the target material as an electrode accelerates plasma species towards the surface and physically sputters the target material, in an analogous manner to physical reactive ion etching, which then travel to the wafers for deposition. Because the sputtering mechanism is physical and no chemical change of the target occurs, the sputtering rate is primarily determined by the applied plasma energy and density, with lower contribution from the target properties.

Sputtering systems have better step coverage than evaporation systems due to several main factors. Primarily, the target is larger, with each location on the target producing a broad angular distribution of sputtered atoms. Additional step coverage improvement is due to the ability to rotate the wafers in plane of the disk, allowing for deposition from all angular distributions. The third factor is that higher gas density yields more gas phase collisions, scattering sputtered atoms into alternate trajectories and broadening the distribution of atom arrival angles to the substrate. The mean free path λ can be calculated from the kinetic theory of gasses:

$$\lambda = \frac{kT}{\sqrt{2}\pi d^2 P}$$

Where k is the Boltzman constant, T is temperature, d is the scattering cross sectional area, and P is the pressure. At a typical pressure of 5 mTorr, λ ≈ 1 cm, much shorter than the typical distance between the target and wafer.

It was mentioned briefly that for insulating materials an AC voltage must be applied to the electrodes. Applying a large negative potential to the target, causes charging with excess electrons. This attracts the positive Ar plasma ions as intended, however the positively charged ions will stick to the surface of the target to balance charges. After about 1-10 µs, the Ar accumulation results in a shielding effect reducing the electric field, and no longer sustaining the plasma. Equivalent results can occur for easily oxidized surfaces which react with trace O_2 molecules and form an insulating compound. Appling high frequency (~13 MHz) AC voltage which adds a ‘discharging’ step to the electrode, reduces charge accumulation and attracts the high mobility electrons from the plasma to

prevent the negative charging. The Ar ions have low enough mobility that they cannot react to the changing field as quickly, causing a build-up of negative charges on the target electrode but preventing accumulation of Ar atoms.

A slight modification to the above sputtering methods named magnetron sputter deposition uses magnets to increase the relative number of Ar ions that become ionized and contribute to the target sputtering[103]. The magnets trap electrons near the target electrode and cause them to spiral along magnetic field lines to collide with more Ar ions close to the electrodes, for improved sputtering rates and efficiency. This reduces plasma density further from the electrodes, reducing the incorporation of Ar into the deposited films and unintended sample heating.

Many other physical and chemical depositions systems exist through further variations of the aforementioned processing, employing different temperature, pressure and gas flow parameters for more controlled deposition. .

Table 2-4 shows typical deposition processes for common materials. Note these are not the only methods to deposit each material, simply the most commonly used method in industry. For example, Si_xN_y and SiO_2 may also be deposited through physical methods.

Table 2-4 Typical deposition methods of common micorfrabrication materials

Material	**Deposition Method**	**Chemical Reaction**	**Comments**
Polysilicon	LPCVD	$SiH_4 \rightarrow Si + 2H_2$ $SiCl_4 + 2H_2 \rightarrow Si + 4HCL$, $SiHCl_3$, and SiH_2Cl_2	~600^0C, grain structure control possible
Epitaxial Si	APCVD, LPCVD	See above	$1000\text{-}1250^0$ C. LPCVD used for low temperature deposition
Si_3N_4	LPCVD PECVD	$3SiH_4 + NH_4 \rightarrow Si_3N_4 + 12H_2$	700^0 C as oxidation mask. 300^0 C for passivation layers. PECVD for Si/N rich films.

SiO_2	LPCVD, PECVD, APCVD Thermal Growth	$SiH_4 + O_2 \rightarrow SiO_2$ $2H_2Si(OC_2H_5)_4 + O_3 \rightarrow SiO_2$ + by-products	200-800^0 C 200-500^0 C Only if within thermal budget
Ti	Magnetron Sputter		CVD difficult
Al	Magnetron Sputter		25-300^0 C standard
Au, Cr, Pt, other	Magnetron Sputter		
Cu	Electroplating, sputter, CVD	$Cu^{+2} + 2e^- \rightarrow Cu$	Electroplating most common

2.5.6 Bulk processing: wafer cleaving

One major benefit of the listed MEMS processing methods is that they are all parallel flood methods, affecting the entire surface of the wafer simultaneously. This allows for the simultaneous fabrication of many structures or devices, limited by the size of the wafer. This up-scaling ability was crucial to the development of the semiconductor industry, allowing fabrication of millions of transistors on a single wafer. In the case of many MEMS applications however, it is desirable to separate the fabricated devices from the wafer after fabrication.

It is well known that Si can be diced, or cleaved, along its crystal planes. Using a diamond blade to inscribe a mark on the wafer, further stress causes a cleave to propagate along the crystal plane yielding perfectly straight breaks. For a <100> oriented wafer, the cleave planes will be parallel and perpendicular to an orientation flat, allowing cleaving into rectangular shapes.

This system encounters problems for fragile structures, or in this case, a via though the wafer bulk. Due to the high stress concentration required for cleaving propagation, the cleave plane often deviates from the initial scribed marking and travels to the fragile holes, breaking the windows. Other methods of separating devices exist as well, including wire saw cutting, and laser cutting.

Saw blade cutting of Si is a very effective approach for large processing, using a metalized diamond blade at a relatively slow linear velocity of ~100 mm/s combined with a mechanical stage, Si wafers are diced in any orientation, non-restricted to crystal planes. The mechanical saw causes chipping of the edges of the silicon, limiting cutting speeds to 10 mm/s, and may induce cleaving along the

crystal planes of the Si[104]. Mechanical vibrations introduced through the wafer propagate which may destroy fragile structures and membranes, and contamination on nearby surfaces due to debris thrown by the blades is common. Diamond saws have a width around 1 mm, with cutting kerf up to an additional 1 mm, sacrificing a large amount of the wafer for small devices[105]. High accuracy systems may achieve cutting kerfs around 125 μm[104].

The best way to reduce mechanical damage to the cutting system is the removal of mechanical contact by using laser beam systems. The laser reduces chipping, allows curved cutting paths, achieves kerf widths of 30 μm or lower, and scales well with thinner wafers. Despite these advantages there are several key parameters which must be addressed, most of which are related to the heating and ablation required for material removal, and the related nearby damage.

Laser cutting involves both thermal and non-thermal processes to remove material from the cutting path, and typically operate in a pulsed mode, applying large bursts of energy in short, ~1 μm, time periods to melt or damage the substrate. Si is typically cut with actively q-switched Nd:YAG lasers, however, near infrared and long wavelength CO_2 lasers have been used. The mechanisms of material removal, and details of laser energy pulses is beyond the scope of this thesis and the reader is directed to one of many textbooks for further reading, with my personal favorite 'Laser Engineering' by Kelin Kuhn[106]. The field of laser machining has been very extensively studied for Si wafer cleaving, however, much of it is irrelevant to this work as it is not available at McMaster, or in nearby facilities for use.

One system that is available in Dr. Leyla Soleymanis lab, McMaster University, is a 30 W, air cooled, CO_2 (10.6 um) laser with no pulsing and beam spot size of ~80 μm from Universal Laser Systems Inc. USA. From the optical absorption curve of Si, it shows that the absorption of this wavelength is approximately zero, or small enough to be neglectable[107]. Using a similar device, it was shown that by attaching a glass slide to the back of a Si wafer, the glass slide absorbs the 10.6 μm light and cause localized heating of the Si substrate, which alters the absorption characteristics, allowing absorption and melting of the Si[104]. Their results show that a high number of passes increase cutting depth at the cost of increased edge roughness, and in all cases re-solidification near the cutting kerf and accumulation of Si vapour deposits exist after cutting.

2.6 Focused Ion Beam

A Focused Ion Beam, or FIB, is like an SEM with a surface scanning beam of particles, however in place of electrons, ions are used. Most typically Ga^+ or Ar ions are accelerated at the sample surface by a voltage of 1-30 kV, resulting in imaging, milling, deposition, or etching of the surface with nanometer process control. They very high control of the FIB has caused it to be extremely valuable in micro and nanomanufacturing for fabrication and characterization, and it has seen extensive use in sample preparation for TEM.

FIB milling is a process where the high energy, and mass, ions bombard the sample and physically sputter material from the surface through momentum and nuclear energy transfer[108]. The beam displaces targeted atoms, losses some energy, and continues to propagate into the sample displacing further atoms and effectively sputtering targets from the substrate in an analogous manner to dry etching mechanisms. A common metric in FIB processes is the sputtering yield, r, a function of material properties (primarily density), incident angle, and beam energy. Under typical conditions of 10-40 keV, Ga^+ ions are implanted between 10-30 nm into Si or SiO_2 milling holes with an aspect ratio around 10-20[109]. The ion beam is finely focused to around 10 nm and is scanned in any desired pattern to mill shapes with a similar minimum feature size. Common issues are the redeposition of sputtered material contaminating nearby surfaces, and Ga^+ contamination into the sample.

FIB imaging is accessible due to the emission of secondary electrons (SE) and ions from the target upon bombardment. The SE, like those generated in an SEM, are collected by a detector and used to reconstruct topographic and Z-contrast images. During imaging, Ga^+ ions will be implanted into the sample and surface sputtering of the sample also occurs. Reducing beam voltage and current reduces the sample damage, however higher noise images are collected.

FIB deposition is very similar to that of a CVD system, where a source gas is introduced and the Ga^+ ions dissociate the precursor gases, allowing them to chemically react to the substrate. Using the same scanning techniques as a before, patterns are drawn on the sample surface, with lateral resolution of 100 nm, vertical resolution of 10 nm, and typical growth rates of 0.05 $\mu m^3/s$. Following similar physics to reactive ion etching, precursor gas can chemically etch the substrate with high spatial control.

In this work, the FIB will be used as a milling machine for high control removal of the membrane material, forming holes for high resolution imaging, as discussed previously. Using a typical Ga^+ FIB, the sputter rate of Si_3N_4 is ~0.2 $\mu m^3/nC$. For a 1 μm diameter hole through a 50 nm film and a medium beam current of 1 nA, the milling process should take 1.3 seconds, a trivial operation. Lowering the beam current results in reduced Ga^+ contamination and improved sidewall quality, which is easily done due to the short process time.

2.7 Electrochemistry

Electrochemistry, in a nutshell, is keeping track of chemical and physical state changes though monitoring the transfer of electrons. This thesis is focused around inorganic processes, typically oxidation, the loss of electrons, or reduction, the gain of electrons of metal species. Through various electrochemical techniques, deep understanding of complex chemical reactions can be tracked and characterized. This section is adapted from: Allen Bard, Electrochemical Methods: Fundamentals and Applications 2000[110]; Richard Compton, Understanding Voltammetry 2011[111]; and Noemie Elgrishi et al 2017[112], unless otherwise noted.

2.7.1 Basics: 2 and 3 electrode systems

In the basic case of electrochemical oxidation, a potential is applied to a metal conducting electrode, raising the energy of the electrons within the metal. Once the electrons are at a greater energy than the lowest unoccupied molecular orbit of a nearby species they 'jump' to the molecular species. The potential which must be applied to the electrode varies based on the potential reference and the chemical species, and is referred to as the reduction (or oxidation) potential of the material. The standard reduction potential of the chemical species is measured relative to the natural hydrogen electrode, which is the potential at which a proton becomes hydrogen.

The simplest electrochemical reaction is that of the galvanic 2 electrode cell, which contains 2 metal electrodes electrically connected and sitting in 2 unique chemical baths, connected by a salt bridge which allows for ionic transfer between the baths. At the anode, surface atoms contain high energy electrons relative to the solution state, which is thermodynamically unstable. The surface atoms transfer electrons to the anode, oxidizing, and dissolve into the solution as ions or electrolytes. At the cathode the opposite occurs, where electrolytes are reduced though high energy electrons on the surface, and deposit as precipitates to the electrode surface. In this way, electrons transfer from the anode to the cathode, with a driving force known as the cell potential which is the

difference in the standard oxidation and reduction potentials occurring at each electrode. The number of electrons transferred per second is the cell current, which is primarily dictated by the speed of surface reactions, limited by diffusion of ions to and from the electrode surfaces, and intuitively the surface area and quality of the electrode.

Incorporating a third electrode allows separation of the oxidation and reduction mechanisms to study them individually, at higher control over the applied potential. The three electrodes are named: the working electrode, which applies potential, measures current, is the surface where the desired reaction occurs, and is generally inert to the solution of interest by being made of gold, platinum, or glassy carbon; the reference electrode which measures the potential applied at the working electrode, holds a constant electrochemical potential, and experiences no current flow; and the counter or auxiliary electrode which electrically completes the circuit acting as an electron sink or source, is chemically inert and made of platinum or graphite. In general, electrons may enter or exit the solution through the working electrode at an energy (voltage) measured and controlled by the reference electrode, and the counter electrode exist to balance the flow of charges. The current measured by the working electrode supplies critical information about changes to species within the solution. Note that for corrosion experiments the working electrode is not inert, it is the material of interest which is actively corroded by the solution.

2.7.2 Physical methods: CA and CV

The most common methods applied in three electrode setups are chronoamperometry (CA) and cyclic voltammetry (CV). CA is the process of applying a constant potential to the working electrode and recording the current at the electrode surface over time. CA is typically used to apply net oxidizing or net reducing currents on the working electrode, resulting in deposition or etching on the surface. CV is a cyclic process, where the voltage is linearly changed between an upper and lower bound, forming a triangle-wave shape, typically cycling between oxidative and reductive potentials on the electrode. In both cases, the current measured at the electrode consists of two components, faradaic and non-faradaic currents.

The non-faradaic or capacitive current is due to charge accumulation on the electrodes due to a changing potential or adsorption/desorption of species from the electrode surface. There are no chemical reactions present, simply the transfer of electrical charge onto the electrode and the ‘electric double layer,’ a region surrounding the electrode which balances the net charge on the

electrode with the surrounding solution. The non-faradaic step-voltage current as seen in CA can be calculated as a function of time t by

$$i = V/R_s \, e^{-t/R_s C_d}$$

With applied voltage V, electrolyte (solution) resistance R_s, and double layer capacitance C_d. The product R_sC_d named the 'time constant' has units of inverse time and characterizes the current decay rate after the voltage application. CV applies ramped voltages and the current is predicted as

$$i = VC_d\left[1 - e^{-t/R_s C_d}\right]$$

Naturally, these equations represent ideal non-faradaic currents at conducting electrodes, which are modified ad/desorption of species to the electrode and multistep charge transfer. In typical electrochemical cells the faradaic current is much higher than non-faradaic currents, however for small area electrodes faradaic currents are low and non-faradaic currents can be seen. It is important to remove non-faradaic contributions when comparing and quantifying current signals.

Faradaic processes are those introduced by chemical reactions on the electrode, and separated into two main process types: charge transfer limited, which CV aims to measure, and mass transfer limited, as measured by CA.

For charge transfer limited processes, take a solution at potential V_0 where the reduction and oxidation share the same reaction rate, and generate a net current density of j_0. The Bulter-Volmer equation shows that at an overpotential of η, the current density at the electrode will become

$$j = j_o \exp\left(\frac{\alpha z F \eta}{RT} - \frac{(1-\alpha) z F \eta}{RT}\right)$$

For electrode charge transfer coefficient α, z electrons transferred per reduction/oxidation metal ion, Faraday constant F, universal gas constant R and temperature T. During charge transfer control, the current through the electrode/electrolyte surface will exponentially change relative to the overpotential applied to the electrode.

Mass transfer limited processes are limited by diffusion (movement under a concentration gradient), migration (charged species moved by electric fields) and convection (stirring) of species to the electrode surface, which is primarily studied using CA, but plays a significant role in CV

analysis. In the simple case of a single diffusion limited species, the electrode current is predicted by Fick's diffusion laws, yielding the Cottrell equation:

$$I = zFAC\,\sqrt{D/\pi t}$$

For surface area A, bulk concentration C and diffusion coefficient D.

A typical example of a CV is given by Figure 2-16 which shows the CV of a ferrocene solution (Fc, $[Fe(Cp)_2]$, Cp = cyclopentadienyl) and its reversible reduction to Fc^+ under a cyclic linear voltage from +0.3 V to -0.3 V and back at a scan rate of 100 mV/s. Starting at an overpotential at point A, the system contains only Fc^+ at the electrode surface and extending to the bulk due to oxidation of Fc. As the potential is lowered, surface Fc^+ is reduced to Fc and begins diffusion though the solution. This registers as an increase in current, as electrons leave the electrode. At the point of peak cathodic current, with applied potential $E_{p,c}$ at point C, the current becomes mass transport limited as Fc^+ must diffuse towards the electrode for further reduction to occur. As the scan continues to point D, the cell still experiences the reduction of Fc^+ to Fc, however at an increasingly slower rate due to mass transport limitations and growing of the electric double layer. During the reverse scan at point E, the surface Fc is oxidized back to Fc^+, and the system becomes mass transport limited again as it approaches the positive scan potential range.

From the CV curve in H, several important parameters are measured.

- $E = E_{1/2}$, the potential which is halfway between the two peaks. The peaks are separated due to diffusion limitations to and from the electrode surface
- $E = E_{p,c}$ and $E = E_{p,a}$ the potentials at which the current is at a maximum or peak cathodic or anodic value, respectively. The peak-to-peak separation for a reversible system is 57 mV at room temperature, and measure the stability of the formed analyte, in this case Fc^+.
- $I_{p,a}$¸and $I_{p,c}$ the peak anodic and cathodic currents, as measured from the 'baseline' mass transport limited currents.

The CV scan rate provides information regarding the diffusivity of the redox species and surface conditions of the electrode. At faster scan rates, there is less time for the accumulation of charges and the formation of the electric double layer netting higher peak currents. The Randles-Sevcik equation describes the peak current i_p as a function of the cell properties

$$i_p = 0.446\, nFAC_0 \left(\frac{nF\nu D_0}{RT}\right)^{\frac{1}{2}}$$

For bulk concentration C_0, diffusion coefficient of the oxidized species D_0 and scan rate ν. The peak current should vary linearly with the root of the scan rate, and with the effective surface area of the electrode. The Randles-Sevcik equation calculates effective surface area of an electrode, diffusion constants, or bulk concentrations, depending on the controlled parameters of the system. This equation only applies for freely diffusing redox species, yielding an electrochemically reversible system. In cases where i_p vs $\sqrt{\nu}$ is not linear, then either the system is quasi-reversible, or the generated species have adsorbed to the surface of the electrode. Studying peak-to-peak separation shifts with scan rate and other CV features yields more detail into this analysis.

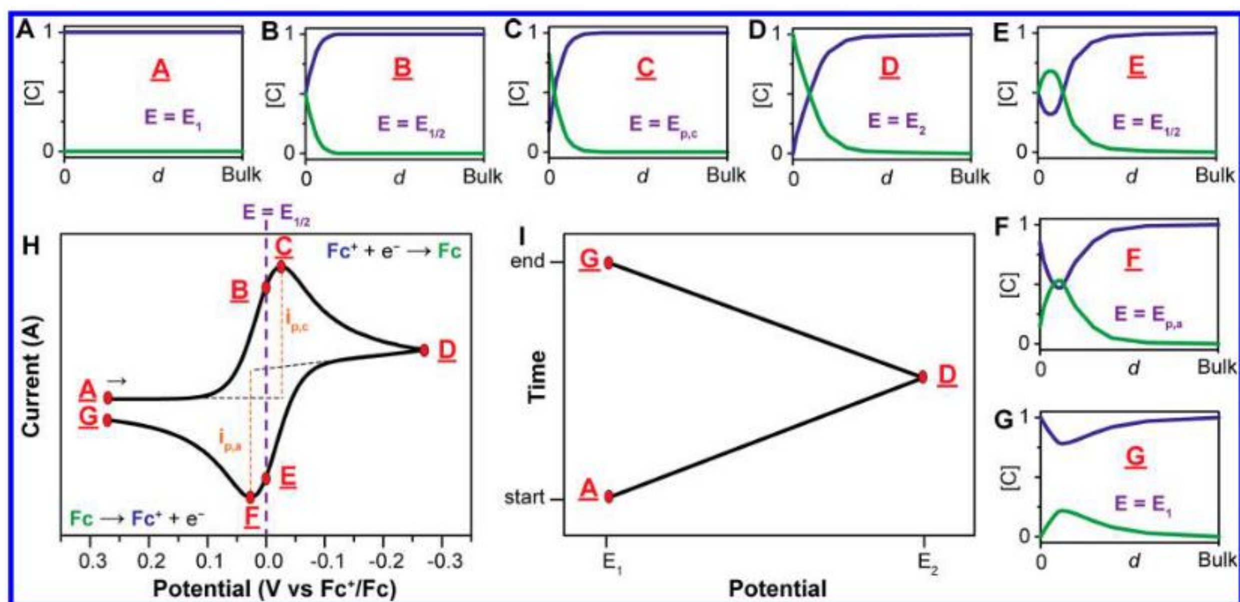

Figure 2-16 Concentration profiles during various stages of a CV cycle. Reproduced from[111]. [A-G]: Concentration profiles of Fc^+ (blue) and Fc (green) vs distance to the working electrode. H: current-voltage profile of 1 mM Fc solution with scan rate 100 mV/s. I: applied potential over time.

Not all systems are electrochemically reversible. Reduced species may: undergo a second reduction step and shift the oxidation potential out of range of the scan; form a new chemical species governed by a reaction rate k, reducing the peak currents for each consecutive scan; or the oxidation species may be limited by an initial generation step. Each of these effects will modify the uniformity of the CV and can therefore be studied.

2.7.3 Physical Electrochemistry: Electrode Specifications

In the previous subsection, several places noted the importance of the working electrode surface area. It is important to note that the current predictions are based from electrochemically active surface area, not geometric surface area. Adsorbed insulating species or inactive surface states may

result in decreased effective surface area, whereas wrinkles and 3D features increase the active surface area above the geometrical area. As electrochemistry is a surface based method, the surface quality is especially important when designing electrodes which are not meant to interact with the solution, and characterization of fabricated electrodes becomes important. Each of the three electrodes have different specifications which must be met.

A Working Electrode (WE) must be inert to the solution and the redox reaction in the potential range of interest. In pH 7 water, glassy carbon (GC) electrodes are stable from approximately -1 V to 1 V, platinum from -1 V to +0.5 V, and gold from 0 V to 1.25 V[113], beyond these potential ranges the electrode material reaches a potential at which it may oxidize or reduce with the solution, yielding currents which add to the CV signals, but are not a measure of the electrolyte. These potential windows vary based upon the supporting solution.

The surface preparation of the electrode is important, to ensure no contaminating species are on the electrode. For macroelectrodes this is achieved by mechanical polishing of the surface using an aluminum slurry and cloth polishing pads followed by sonication in pure water or organic solvents[114]. Mechanical polishing microelectrodes is impossible, so chemical cleaning is used as described section 2.5.2-Wet chemical etching. GC and gold electrodes are sometimes electrochemically polished, where the surface is oxidised and reduced 40-80 times stripping any adsorbed species in the process. This is typically done in 0.1-1 M H_2SO_4 for gold, at a potential range of -0.3-1.7 V vs Ag|AgCl.

The counter electrode (CE) acts as a current source or sink to balance the flow of charges occurring at the working electrode. Whatever reaction occurs on the WE, the opposite occurs at the CE. The CE must not interfere with electrochemical reactions and is made much larger than the WE to allow excess current flow and is made of inert Pt or Au.

The Reference Electrode (RE) is a metal submerged in an encapsulation electrolyte solution and separated from the bulk solution of interest by use of a glass sheath with a semi-porous tip, and acts as a constant potential refence, irrespective of applied potential and solution/electrolyte materials. The most common macro electrodes are the saturated calomel electrode (SCE), the standard hydrogen electrode (SHE) and the Ag|AgCl electrode. Through isolation in a standardized solution, the electrodes hold a constant potential and are calibrated to determine the electrode potential versus a standardized reference.

This RE geometry becomes very challenging for microfabrication or surface construction, the most difficult step being to prevention of dissolution of the electrodes' electrolytic solution. Typical techniques summarized by Shinwari et al in 2010[115] are described in the remainder of this section. One approach would be thin film or electroplating deposition of the base metal (ex Ag) followed by chlorination for Ag|AgCl or the introduction of Hg_2Cl_2 for SCEs to 'activate' the electrode. For Ag|AgCl, the activation is done either through a spontaneous chemical reaction with $FeCl_3$ to form a AgCl layer, or electrochemically though oxidation of the electrode in a HCl bath.

Following this is the requirement for a solution bath, with a diffusion barrier to the electrode. A microfluidic channel is lithographically formed out of a semi-porous agarose gel, polyacrylamide gel, porous glass, polymer membranes with laser ablated nanopores, or more complex heterogeneous designs. Unfortunately for a microfluidic channel design, the electrolyte solution must be continuously flushed over the electrode, which is not ideal for the liquid cell setup.

Some solid-state Ag|AgCl setups replace the filling solution with a KCl-saturated agar gel, which has low vapor pressure and shows stability issues after long term storage since manufacturing. In some work, polyurethane, nafion, or silicone rubber coatings are used to protect the agar gels from evaporation, or polyvinyl chloride (PVC) and epoxy coatings have been used on bare electrodes, however they have shown poor reproducibility in construction.

In some work, the filling solution is removed entirely causing the solid state electrode to become a quasi-reference electrode, which does not have a guaranteed voltage and will drift depending on the test solution. The AgCl layer on the electrode also dissolves with use, however for single use and short lifetime lab-on-a-chip type applications this is less significant. An example of this is a chlorinated silver electrode coated in an adhesive aminopropyltriethoxysilane (APTES) and a blocking perfluorocarbon polymer (PFCP) which reduced contaminating ions, which showed minimal drift long term, but significant drift with Cl^- ion concentration.

Many other approaches have been taken for surface fabrication of both RE and quasi-RE, however in all cases it requires several microfabrication steps, with highly stable electrodes typically being more complicated to fabricate. The reader is directed to Shinwari et al.[115] for further information.

In cheaply manufactured surface electrode setups, all three electrodes are often chosen to be the same material to reduce fabrication costs. In the case of three gold electrodes, the pure gold makes

a poor RE. A RE holds a constant potential though a redox reaction with its surrounding electrolyte. For this reason, metals such as Ag and Fe which form complexes with the surrounding solution act as surprisingly stable REs. Gold is conducting and inert, meaning small current changes cause potentials shifts, and no surface redox reactions are available to balance the voltage.

Commercially available systems employ gold or platinum reference electrodes, which is not sufficient for high accuracy electrochemical experiments. This provides motivation for construction of liquid cells with multiple electrode materials, and the ability to electrochemically prepare and clean large batches of multi-electrode chips for LCEM.

2.8 Chapter conclusions

Commercially available LCEM systems provide a solid generalized starting point for many *in situ* experiments, however, as discussed, there is much room for improvement. By looking at the electron scattering induced from the thick liquid layers and membrane materials, it has motived the need for improvement of resolution in liquid cells, which will be addressed by forming small holes in the membrane material for imaging. Under flowing conditions and a sufficiently small aperture, the surface tension of the liquids will prevent breaching of the vacuum system.

Commercial electrochemical systems are limited by the choice of electrode materials, and the lack of a suitable reference electrode. This and the inflated cost of chips has motivated work to reconstruct a liquid cell chips, with customization over electrode materials, geometry, and dimensions of the structures. The fabrication techniques to be applied have been briefly described, presenting many options available for the construction of the system.

3 Experimental Methods

3.1 Chapter introduction

In this chapter, the experimental processes applied are described. The chapter begins with a discussion of applying the microfabrication technology presented in chapter 2 and the challenges involved in designing the process flow from a practical standpoint, taking into account the fragility of the membranes. Following this, experimental methods for testing and characterization of the custom chips is presented. Afterwards, *in situ* experiments are outlined which demonstrate the application of the FIB milled holes in the membranes through the study of oxidative etching of palladium dendrites under beam induced and electrochemical bias. For all sections images of the fabricated structures are discussed in chapter 4.

3.2 Fabrication process flow

Microfabrication has existed for several decades, and as such there are a plethora of fabrication techniques available. To obtain maximized throughput with a minimal chance of breaking devices, the fabrication process flow, or the order of fabrication, plays a significant role. For this work, there are three main structures that need to be fabricated: the viewing window, the electrodes, and the isolation layer.

3.2.1 Windows

The formation of the windows is most complicated by the etching mechanism though the bulk Si wafer. As discussed in the background, the Si may be wet chemically etched in KOH, TMAH (tetramethylammonium hydroxide) or EDP (ethylene di-amine pyro-catechol), or dry RIE (reactive ion etch) by following a Bosch process. The optimal window materials are SiN_x or SiO_2 for the high strength and low atomic density, allowing them to be made large (up to 500 μm) and still support the vacuum of the microscope with high electron transparency. Complicating this process is the choice of masking material for the Si etch, and patterning of the masking material. Ideally, the masking material on the wafer back side is the same as the window material on the front side to reduce the number of fabrication steps. Figure 3-1 shows a flowchart presenting the combination of these parameters, and the required masks.

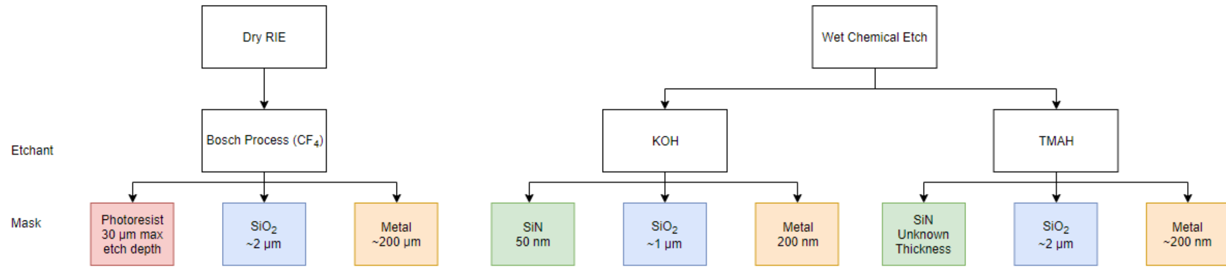

Figure 3-1 Si etching and masking options

Mask patterning depends on the mask material and thickness. Photoresist can be directly patterened using light exposure and developing, whereas SiO_2 is patterned through photolithographic masking followed by either a wet chemical HF etch or a RIE step. SiN_x is patterned either by dry RIE or in phosphoric acid, the latter requiring a thin SiO_2 layer to be photolithographically patterned as a mask, because the acid readily etches PR so a hard mask is needed, adding a sizeable number of fabrication steps.

One approach is thermal growth of SiO_2 on both sides of the wafer followed by lithographic patterning of the back-side, to mask both sides of the wafer and expose a via for bulk Si etching. A highly controlled KOH or TMAH process would be used to etch through the bulk Si, while simultaneously thinning the front side film to the required >100 nm.

Following this procedure, TMAH etching yields a typical Si etch rate of ~60 µm/hr[80], meaning a 300 µm wafer etches in 300 minutes. For the same etching conditions, wet thermally grown SiO_2 etches at 16.4nm/hr, resulting in 82 nm of wet growth-SiO_2 being consumed. Using a growth model and constants derived from Gary McGuire, 1988[116], it would take ~4 mins and 44 seconds to grow an oxide 132 nm thick, assuming a 50 nm remaining film, at 1100 ^{o}C in a wet environment.

Similarly for KOH etching, etch rates over 100 µm/hr are achievable for 40 wt% KOH solution at 80^{0} C. The required 3 hr etch consumes 1.2 µm of wet growth-SiO_2, assuming a 400 nm/hr etch rate[85]. This SiO_2 layer would take ~3 hours to grow, under the same conditions as before. For both KOH and TMAH etching, all etch rates and film thicknesses must be very precisely controlled to prevent over-etching of the front side SiO_2 which forms the membrane material. The high precision is not easily done for the expected 5 hr chemical etches of the Si, especially considering etch uniformity across the wafer.

A Bosch process requires growth and patterning of either a silicon oxide or nitride. As discussed in the background, over etching of the Bosch process will either destroy the desired membrane, or since the membrane etches slower than the bulk, yield a highly undesired pedestalling effect. The Bosch process would need very high control and uniformity, which is not easy due to the substantial number of fabrication parameters. It is not possible to perform a Bosch process before deposition of the membrane, as there will be no substrate where the membrane is to be formed.

The most facile solution is a SiN_x window combined with a SiN_x masking material, by using LPCVD grown 50 nm films on both sides of the wafer. Chemical patterning of SiN_x requires a SiO_2 mask and would damage the front side film, however dry RIE of a PR patterned surface will only affect the back face. RIE has a 1:1 selectivity to PR, confirming that standard 1 μm PR films will be more than sufficient for the nitride patterning. The RIE step does not need high precision as over etching affects the underlying Si at nanometer scale, which will soon be etched entirely. The patterned and masked wafer will then be wet etched in either KOH or TMAH to form the membrane, which etch the SiN_x at 0-0.1 nm/hr and ~0.1 nm/hr respectively.

Although several CVD systems are available at McMaster, it was more efficient to purchase crystalline Si wafers with 50 nm SiN_x pre-deposited on both surfaces rather than to grow it ourselves. The wafers purchased from University Wafer Inc. (Boston, MA) were 2” diameter, 280 μm thick, P-type (boron) 1-5Ωcm, {100} orientation, double side polished with 50 nm stoichiometric LPCVD SiN_x on each face. There was an additional order with 300 μm thickness, and single side polish. It was discussed in the background that low stress Si rich nitride layers have reduced residual stress and lower Young’s modulus, which yields higher bulging but lower risk of windows breaking during operation. Stoichiometric films were used for cost efficiency and reduced bulging.

To etch the bulk Si, TMAH has a slow, ~0.1 nm/hr, etch rate of the SiN_x and yields high surface roughness, whereas KOH etches the nitride at 0-0.1 nm/hr[85] and provides a much smoother Si surface, as discussed in section 2.5.3. The high stability of the nitride layer allows over etching to be used as compensation for any poor etch uniformity without compromising the membranes. As discussed in the background, KOH etches Si crystal planes at different rates yielding slanted sidewall profiles. A process flow for this step is illustrated in Figure 3-2.

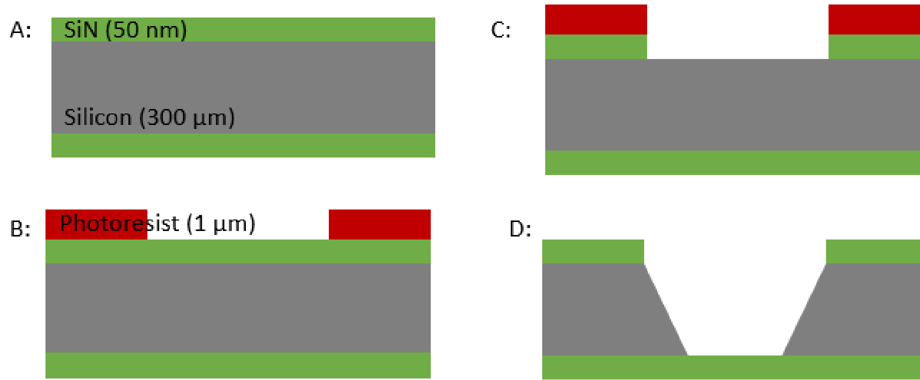

Figure 3-2 Window fabrication process flow. A: Deposition of SiN on both wafer surfaces. B: Photlioresist deposition and patterning. C: RIE etching backside SiN. D: KOH wete tching of Si, leaving a freely suported membrane.

The photolithography mask layout for this process is shown in Figure 3-3. The rectangular etch holes are located to align with viewing holes in the Protochips Poseidon holder, and are designed such that the windows will have dimensions of 200 x 40 µm, after the KOH etch through the bulk. The lithography step will use a standard positive tone PR, Microposit1808, which forms an 800 nm thick film after 30 seconds on a spin coater at 3000 rpm.

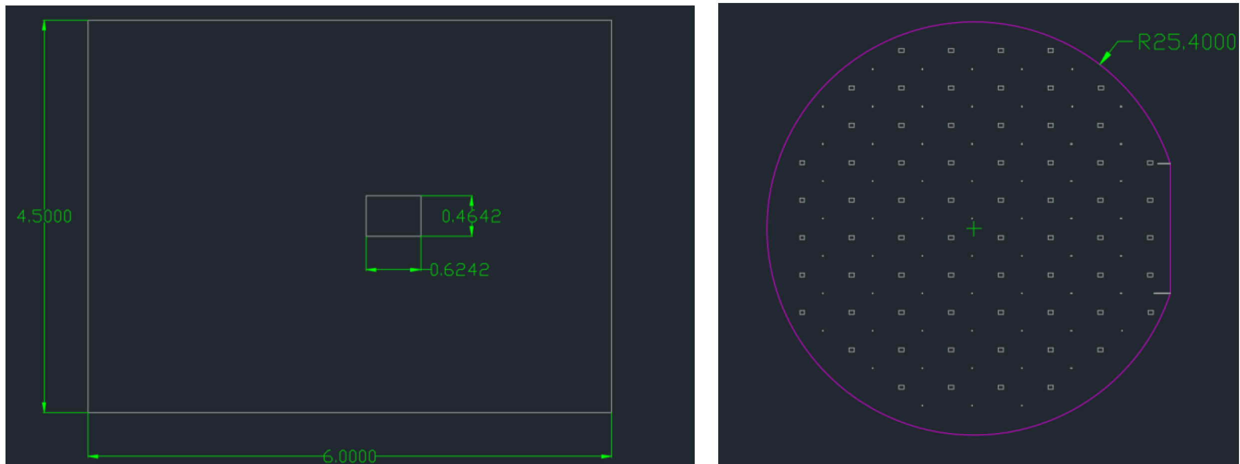

Figure 3-3 Mask design for windows in liquid cell chips. Dimensions in mm. (L) Dimensions of a single chip, with dimensions of the back side SiN hole required to form a 200 x40 µm veiwing window. (R) Wafer-sized view of the chip. The smaller white squares are 10 x10 µm, and located at the corners of each indivdual chip for allignment, and future cleaving. Purple structres inward are opaque, and white structures inward are transparent.

The full lithography procedure will be addressed in the appendix and generally follows the processing steps outlined in the background. It is important to note that the procedure must be modified relative to the underlying substrate, in this case flat SiN_x. All lithography was performed in a cleanroom available from the Center for Emerging Device Technology (CEDT) at McMaster.

RIE was performed using a STS 320PC available at the Centre for Emerging Device Technologies (CEDT, McMaster University) operated with 2.5 cm^3/m of CF_4 and 5.6 cm^3/m O_2 gas, with RF power of 120 W (1430 V peak-to-peak) and operational chamber pressure of 32 mTorr. Previous calibration at the facility found this recipe to etch stoichiometric SiN_x at ~60 nm/min, with a selectivity towards PR and Si of 1:1. To ensure complete removal of the 50 nm SiN_x, an over etch was performed with 2 min etch time, which did not compromise the remainder of the substrate due to excessive PR thickness.

During the KOH etching, the near-boiling temperature causes water to evaporate from the solution, increasing the etchant concentration and influencing the etch rates. Previous work found that a 250 mL beaker with exposed surface area of 28.27 mm^2 and baking temperature of 40^0 C yields 2.5 mL/hr evaporation rate[84], netting ~115 mL water loss over the expected 46 hr etch using this temperature. For improved etch rate and larger samples, a higher bath temperature, 80^0 C, and surface area, 8.11×10^{-3} m^2, results in a calculated 74 mL/hr evaporation rate[117], assuming the air above the beaker is 80^0 C and not moving. If a 250 mL solution losses 74 mL/hr, the solution will be depleted by the time a 4 hr etch is complete. In a less extreme hypothetical case where evaporation is reduced to a total of 100 mL water loss, the new concentration increases to 41.4%, decreasing the etch rate from 78.59 μm/hr to 64.27 μm/hr [79], and increasing the total etch time by up to 1 hour for a 300 μm wafer. KOH etch rates are not linear with concentration making high precision etches very difficult considering the water evaporation, further motivating the use of SiN_x as a mask. It was noted previously that although an over-etch is not problematic in theory, in practice a 1 hr variability in the expected etch time yields considerable risk of windows breaking along with further defects such as pin holes in the mask and etching of the SiN_x membrane.

The water evaporation was minimized by creating a custom reflux system to condense evaporating water vapour back into the solution. The reflux system is a PTFE (Teflon, Polytetrafluoroethylene) lid which fits tightly over the lip of a spout-less beaker, shown in Figure 3-4, which contains a reservoir filled with ice water, a small vent to prevent accumulation of gasses within the beaker, and a via for a dipping basket. Evaporating vapour that contacts the chilled lid condenses back into liquid phase and drops to the solution. In an ideal system, ice water could be continuously pumped across the surface of the lid to maintain cooling, however due to fabrication limitations the system was refreshed manually by adding crushed ice into the reservoir, waiting for it to melt, and

subsequently removing the water to be replaced with more ice. This system was repeated approximately every 20 minutes as the ice melted.

The lid was fabricated with the help of David Hendriks in the department of Mechanical Engineering at McMaster University using a CNC milling machine and drill press.

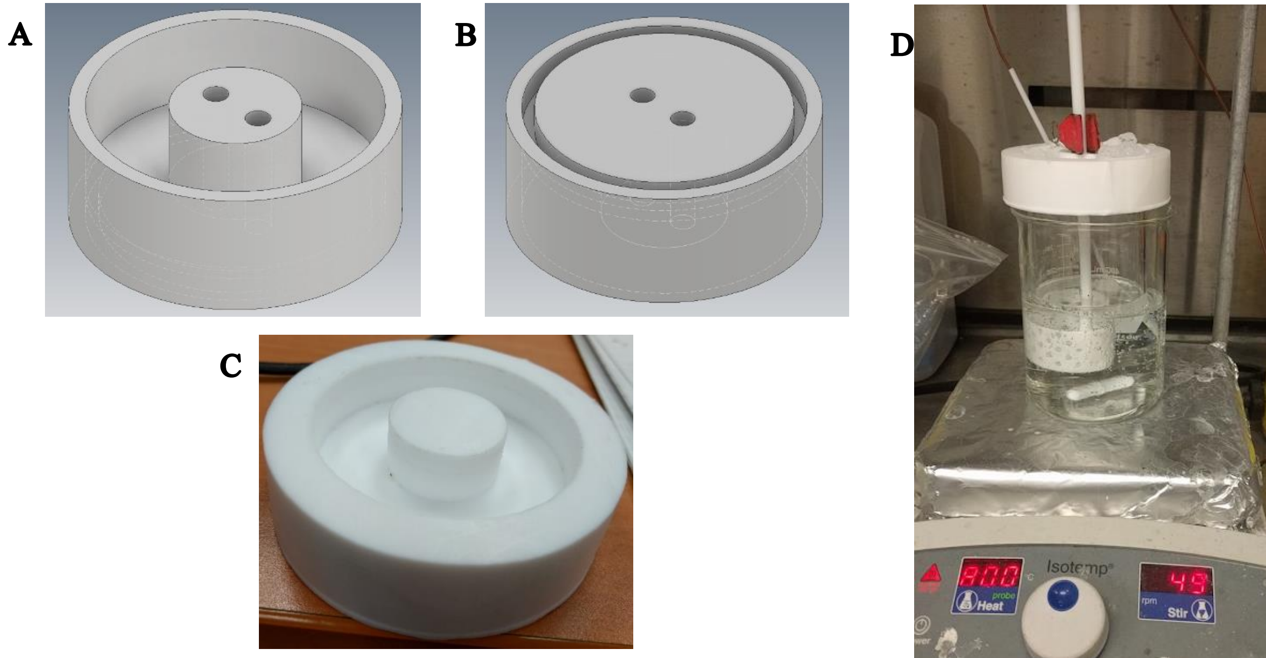

Figure 3-4 Reflux lid for KOH etching. A-B: CAD models of the reflux lid, not to scale. Top view of resivoir and bottom view of the grove for conformal fit on a spoutless beaker. C: CNC milled lid, before inclusion of vent holes and dipping basket via. D: Operation of the relux system. Note the thermocouple placed in a heating bath, a magnetic stir rod, and dipping basket. The ice is placed in the reflux lid, and repalced as it melts.

To maintain temperature uniformity across the wafer during etching, the solution was heated indirectly through a water bath, thermocouple controlled to 80^0 C and stirred continuously via a magnetic stir rod in the beaker at 50 rpm for the duration of the etch. The etch solution was 30 wt% KOH prepared from 106 g of solid pellets and 250 mL of deionized (DI) water (MilliQ, 18.2 MΩ resistivity), saturated with ~50 mL of isopropanol, such that excess isopropanol formed a film on the solution surface. The expected initial etch rate is 60 μm/hr, yielding a 5 hr etch time assuming no evaporative concentration changes, or etch rate changes due to geometry.

At the end of the etch the wafer was removed and cleaned with DI water, and blow dried using compressed air. An optical microscope was used to inspect the windows for completeness of the etch, uniformity, and to identify broken membranes, with a typical yield of about 50 windows perfectly formed of the 57 in the mask, and the remaining windows either broken or under-etched.

3.2.2 Electrodes

The systems available within McMaster University for metal deposition are metal evaporators, Direct Current (DC) and Radio Frequency (RF) sputtering and Chemical Vapor Deposition (CVD). Screen printing and electroless deposition require inexpensive equipment and are also viable, however they cannot achieve the required 10 μm resolution. The electrodes were sputter deposited and photolithography patterned.

Gold electrodes were sputter deposited using a Torr sputtering system available at the CEDT. The gold required an adhesion layer of 10 nm chromium, deposited with RF power of 60 W in a 10^{-5} Torr vacuum chamber under 6 sccm of argon flow to maintain the plasma at a rate of 0.01 nm/s. Gold films were DC sputtered in the same system without breaking vacuum between depositions, at ~300 V and ~0.7 A for a rate of 0.1 nm/s. Titanium is another possible adhesion layer, but etching of the Ti is more complicated than Cr as most common etchants also attack the SiN_x, and the thin Ti films typically formed small islands rather than the uniform coverage seen with Cr.

As discussed in the background, the electrodes should be able to be electrochemically cleaned as a batch, and fabrication must facilitate multiple electrode materials. The electrode layout was chosen with the following conditions: the contact pads must align with the contacts of the liquid cell holder; the Working Electrode (WE) is placed on the membrane; the Counter Electrode (CE) is much larger than the WE; the Reference Electrode (RE) is very close to the WE and large enough that formation of a bubble does not remove the electrode from the solution; the traces from electrode to contact pad are spaced apart to reduce interference between electrodes; and traces have minimal resistance such that they do not contribute electrical noise. There were several designs of electrode layouts, with the 2 final designs shown in Figure 3-5 and Figure 3-6. The first design does not have the ability to electrochemically clean in a batch, the second one has all WEs connected to a single contact point, and all REs similarly joined. The electrical connections are severed once the devices are separated from the full wafer.

Figure 3-6 shows several electrode structures which are not connected to anything and appear to be incomplete, along the edges of the wafer. These structures are used for alignment of the electrodes to the windows. When the window structures are lithographically patterned from the backside and etched to form membranes on the front side, several additional windows were constructed near the wafer perimeter and intentionally broken leaving ‘holes’ on the wafer front

surface. The holes are visible from the front surface and allow alignment of the electrode lithography to the window membranes.

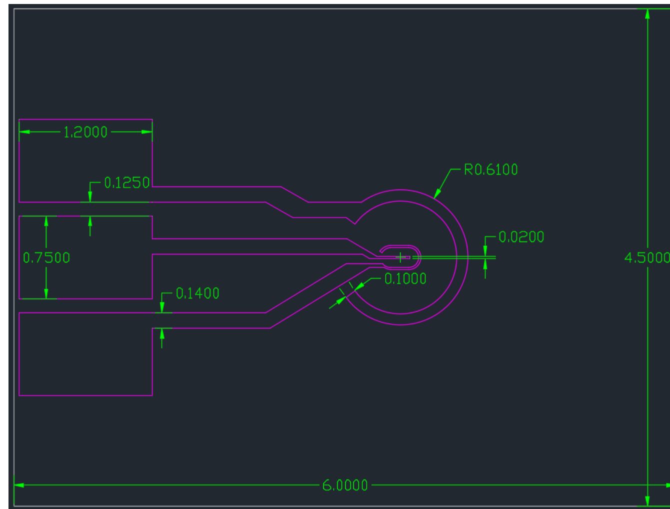

Figure 3-5 Initial electrode design, with dimensions in mm. The largest electrode is the CE, the smallest is the WE, and the middle is the RE. The WE is centered on the veiwing window. The mask was pritied with 2 polarizations: opaque purple structures and transperent chips, or vice versa. A similar mask of wafer scale containing a grid of this design was also created.

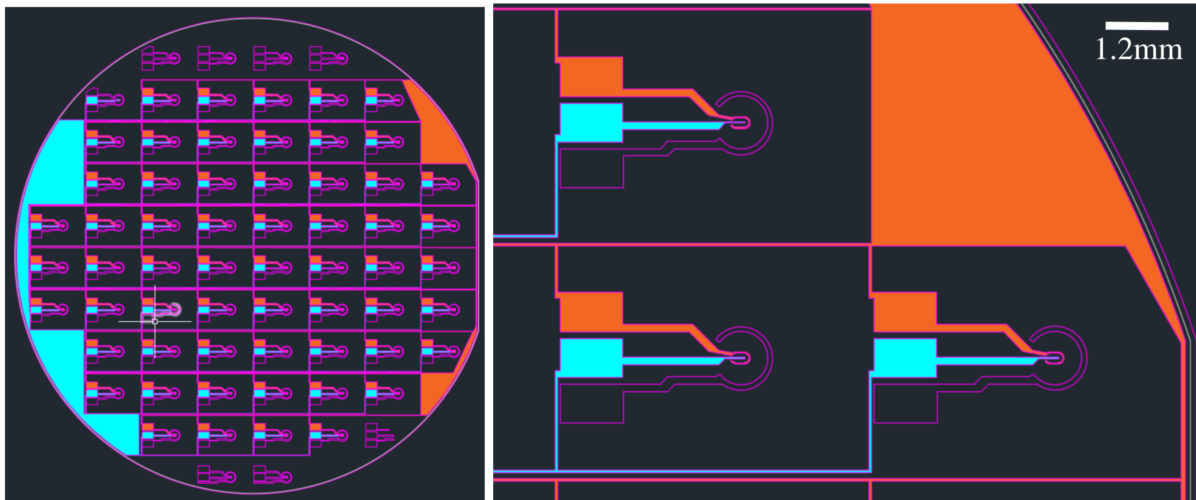

Figure 3-6 Showing final layout of mask for electrodes, along with a magnified view of one corner. All enclosed polygons are set opaque, with the remainder of the wafer set transparent. False coloured orange highlights show the reference electrodes, connected via traces to a central contact pad. Blue highlights show connection of the working electrodes, and the purple counter electrodes are left unconnected.

Although the metal films are not corroded by the KOH solution, they were found to delaminate during long etches, requiring the electrodes to be fabricated after the construction of the windows. This introduced two large problems. Firstly, the metal structures are formed through a ‘lift off’ process where lithographic patterning is followed by metal deposition, and the undesired metal is ‘lifted off’ by removing the PR film and the coating metals. To prevent re-deposition of metals and ensure complete lift off, the step is done in a sonicator, a device which vibrates the solution to

facilitate high diffusion, which also induces mechanical vibrations to the wafers instantly breaking all windows. Secondly, to spin coat the photoresist a vacuum force to holds the wafer in place. The vacuum force and mechanical shaking of the spin coater also break the windows.

The solution to lift off was to directly etch out the electrodes instead. By first coating the entire wafer in gold, PR was applied on top and patterned to the electrode geometry. Wet chemical etchants Cr-etch (product 651826) and Au-etch (product 651818) purchased from Sigma-Aldrich, were used to first strip the Au layer by a >30 s bath in the etchant, followed by cleaning and drying, and another >30 s in the Cr etchant to strip the underlying adhesion layer, both at room temperature and slight agitation. Over-etching of either film resulted in sidewall etching, often breaking continuity of the thin electrode traces. Incomplete etching caused a short circuit between electrodes. Finally, the PR was removed with 2 minutes in hand-agitated acetone, an isopropanol rinse, and plasma ashing to ensure monolayer residues were fully removed. This process involved only chemical baths and was found to very successfully form the electrodes with any risk to the windows coming from human error.

Two approaches were taken to allow compatibility with spin coating photoresist. The first was to place a vinyl sticker on the backside of the wafer. The sticker prevented direct damage from the vacuum of the spindle and provided a softer surface to reduce mechanical vibrations. The stickers used had very high adhesion to the wafer, so great care was needed to remove the vinyl without breaking the wafer. The sticker glue sometimes left residue on the wafer surface, which was cleaned with organic solvents. The second solution is an elastopolymer sold as Ecoflex™, a liquid polymer which dries to stretchy rubber and is used for moulding arts and crafts. Ecoflex™ was dispensed to a 3” Si wafer and allowed to dry. The resulting film was a very flat, slightly sticky substrate to place wafers on for spin coating. The Ecoflex film, if freshly made, was found to have very high adhesion to flat wafers making removal difficult without breaking the wafer. Overused films lost some adhesion, in severe cases causing the wafer to detach during spin coating and shatter. Both vinyl and Ecoflex™ substrates were used interchangeably, however the vinyl yielded to more consistent results.

Even with these systems in place to prevent window damage, photolithography and wet chemical etching involve many processing steps, including surface cleaning before and after each processing step. The membranes are incredibly fragile, and every step introduces a chance of breaking

membranes. The results section will address the success of each processing step in terms of the yield of intact membranes.

3.2.3 Multi-material electrodes

The process for changing a single electrode, or a portion of a single electrode, is straight forward. The traces of the electrodes are made using the same procedure as before to provide low resistance gold traces with a modified mask to not include the end of the chosen electrode, as seen in the working electrode of Figure 3-7. After the construction of the traces, a second lithography step is applied to form either lift-off conditions or etch out conditions (positive or negative PR patterning) for the actual electrode material. The patterns are made to overlap, and assuming conducting materials, this is sufficient for electrical connection.

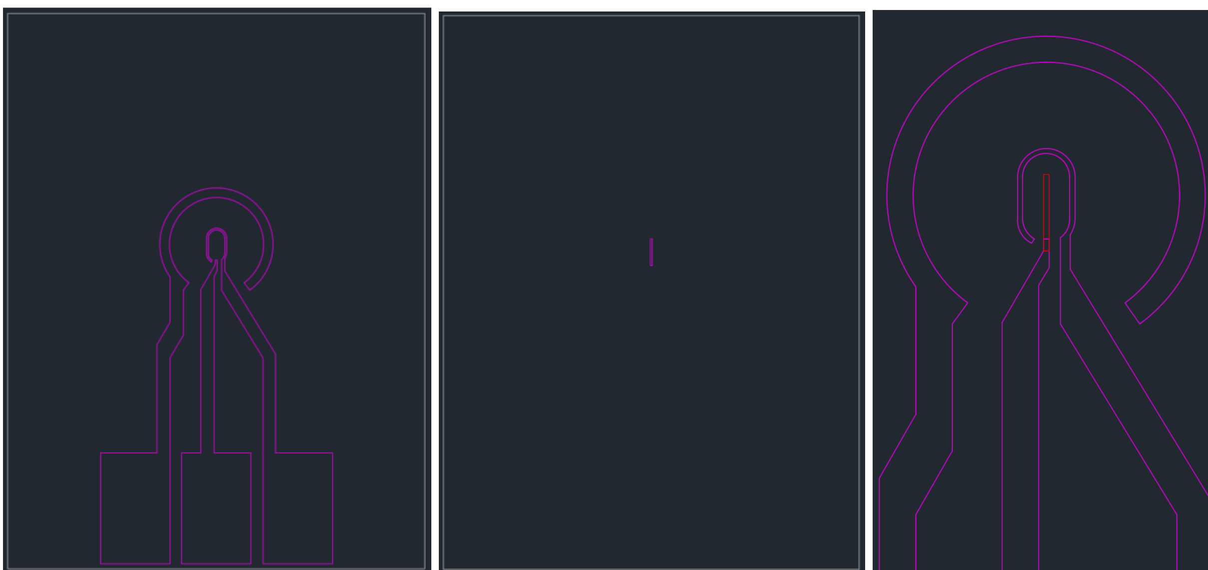

Figure 3-7 (Left) Electrode traces with missing end to WE. (Centre) Mask for only the central electrode. (Right) Magnified overlay, showing overlap of the WE with the contact trace.

It was mentioned previously that lift off is not a suitable method due to redeposition occurring without access to sonication methods. For certain electrode compositions a wet etch could be used, but this approach may be incompatible with all other materials on the chip, namely Si, SiN_x, Cr, Au, and PR depending on the etchant. Electrodeposition may also be used to coat a base gold electrode with a new material, although not all materials may be electrodeposited. Therefore, lift off is often the only viable approach despite the low success rate.

This general approach may be used for any of the three electrodes, not just the WE. In fact, it is possible to replace an entire electrode not just the electrochemically active area, and it may be

repeated twice for all three electrodes to have their own material. For more complex RE's such as the chlorinated silver reference electrode, additional fabrication and masking steps are required to ensure no contamination of the other electrode surfaces, as discussed in section 2.7.3.

It now becomes immediately obvious why multi electrode systems are not commercially available: each custom material involves a minimum of a full lithography procedure, etch out or lift off, and two additional cleaning steps, adding a larger chance of windows breaking.

In this work, a carbon working electrode was fabricated using two approaches. In all cases carbon coatings were physically sputtered in a EMTech K775 available at the Canadian Centre for Electron Microscopy (CCEM) at McMaster University. Carbon coating was performed for 20-60 s with an approximate deposition rate of 1 nm/s from a carbon target under 10^{-6} mbar vacuum. The first approach taken was to sputter carbon over an entire sample followed by a 1 μm layer of photoresist to protect the carbon electrode. O_2 plasma ashing performed at the CEDT for up to 20 mins at 50-70 W was used to oxidize and strip the unprotected carbon, followed by photoresist removal to expose the carbon electrode. A surface profilometer was used to measure the PR height after etching to ensure the carbon electrode was not ashed, and again after PR removal to test the electrode height. Plasma ashing is used as wet chemical carbon etchants will remove the PR too quickly, risking damage to the electrode.

The second approach was a negative resist lift off method. Negative photoresist NR9-1500P was used to form a 1.4 μm film protecting the substrate and exposing the working electrode. Following the same carbon deposition, a lift off was applied using RD6 developer. Both developer and photoresist were purchased from Futurrex, Franklin NJ, USA.

3.2.4 Isolation layer

The isolation layer was used to cover the electrode traces for interacting with the experiment, act as a spacer for the sandwich setup, and isolate the solutions to near to the viewing window. It was formed via two different materials, a SiO_2 solid layer, and a SU-8 polymer layer. SiO_2 deposited though physical sputtering in the same Torr system discussed earlier offers very high control of film thickness. Patterning, however, is much more challenging. If SiO_2 film patterning is done though liftoff, the typical 500 nm isolation layer thickness requires a minimum of 2 μm PR layer, which is a very thick film for lift-off conditions. Wet chemical etching using HF is possible,

however HF slowly etches stoichiometric SiN forming pinholes in the membrane, and has very specific handling requirements due to its personal and environmental dangers.

SU-8 is an ideal option as it is a photoresist material itself, making patterning simple and it becomes chemically resistant once fully dried. SU-8 thickness is controlled through the spin speed applied during spin coating, and by varying the viscosity of the initial film. A major problem is that, by looking at the film-thickness to spin speed curve, commercial versions of the 3000 series resist have a minimum film thickness of 5 µm. An older version of the resist, the 2000 series, shows thinner film availability; however, it has very poor adhesion to SiN_x surfaces.

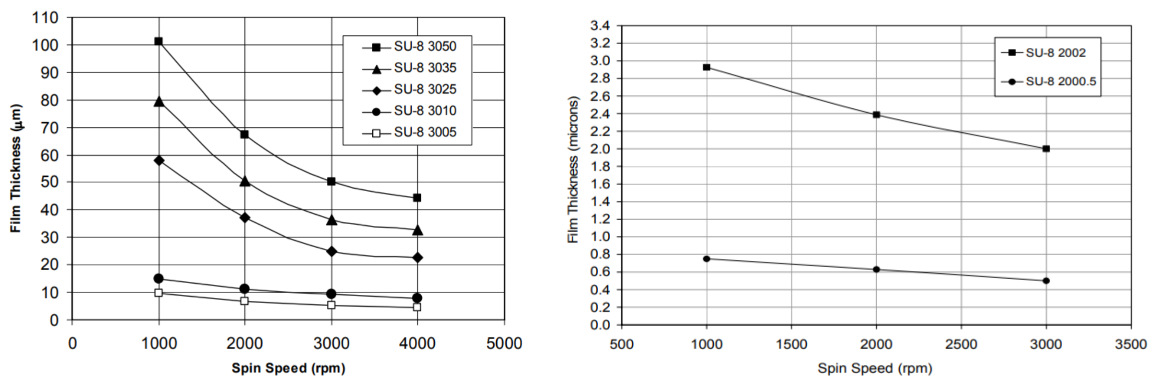

Figure 3-8 Film thickness curves for SU-8 3000 series (left)[118] and 2000 series (right)[119]

The SU-8 solutions are characterized by their %solid composition, with the solid material diluted in cyclopentane. From the 2000 series, the 2005 resist contains 45% solid, with the 2000.5 resist containing 14.3%. Using this as a baseline to form a 500 nm film, SU-8 3005 series resist was purchased and diluted from 50% solid to 14% solid, and a spin speed curve for the resulting resist was created. More details on the SU-8 procedure are presented in the appendix.

The SU-8 layout was chosen to contain the liquid to a region of interest around the electrodes and the window and isolate the traces which lead to the contact pads. The layout is such that when the small sealing chip of 2x2 mm dimension is centered above the window, all 4 corners are supported by the isolation layer, and electrolyte solution may be flown between the chips. The contact pads are left exposed as well for electrical contact with the holder electrodes.

Figure 3-9 Mask design for isolation layer, dimensions in mm. (left) close up of the design, where purple structures are opaque and the majority of the wafer is transparent. (centre) mask outline showing grid of isolation layer structures. Each row of chips has an additonal opaque strip the width of the cutting kerf, to prevent SU-8 deposition along the cutting path, which is easier seen in the closeup of the right image.

3.2.5 Wafer Cleaving

In the process flow shown above, a single wafer contains 56 individual chips which must be separated. In the background section various approaches to wafer cleaving without destroying the membranes was discussed. Briefly, as a proper laser cutting system is not available, mechanical saws were found to break the membranes, and physical cleaving is highly unreliable due to local stress concentrations near the windows.

As described in the background, a laser system which is available in Dr. Leyla Soleymani's lab, McMaster University, is the Universal Laser Cutter VLS 2.3, Universal Lasers Inc., Scottsdale AZ, USA, with a 30 W continuous CO_2 laser at 10.6 μm wavelength. The laser was operated at maximum power and minimum scan speed (1%, linear speeds not given by software) with the High Power Density Focusing Optics lens installed, after warming up for at least 10 minutes of operation. Laser alignments were performed using the in line visible red laser sight, and all laser cutting operations were performed behind a IR opaque glass casing with pumped venting to a fume hood.

As an alternative to laser cutting, physical cleaving was performed using a guided diamond scribe aligned to a micrometer stage with vacuum chuck and microscope, to allow high precision scribe markings on the wafer, provided by the CEDT. The scribed marking was surrounded by four microscope slides, two above and two below the wafer, and the wafer was snapped by hand with the slides used to evenly distribute the force along the cleave plane. The results and discussion will address how these parameters were optimized to obtain a semi-reliable cutting method.

3.2.6 Final process flow

It is worth concluding this section with the complete process flow in order, after exploring the many possible fabrication methods. The process can be simply broken up into 5 fabrications steps, labeled A-E in Figure 3-10. Included are cross sectional cartoons of the assembly of the chips.

A: The Si wafers are deposited with 50 nm films of LPCVD stoichiometric Si_3N_4. The surfaces are cleaned with organic solvents and plasma ashing prior to use. **B**: Photolithography combined with dry RIE is used to open a hole in the back-side SiN_x. **C**: KOH wet chemical etch opens a via though the bulk Si, forming the viewing membrane. **D**: A conformal layer of Cr and Au are applied to the wafer surface. Photolithography is used to protect the surface from a wet chemical etch, forming the Au electrodes. Note that for multiple electrode materials, this step will be repeated several times. **E**: SU-8 is patterned to the surface, forming the isolation layer for the electrodes, followed by dicing of the wafer into individual chips for use.

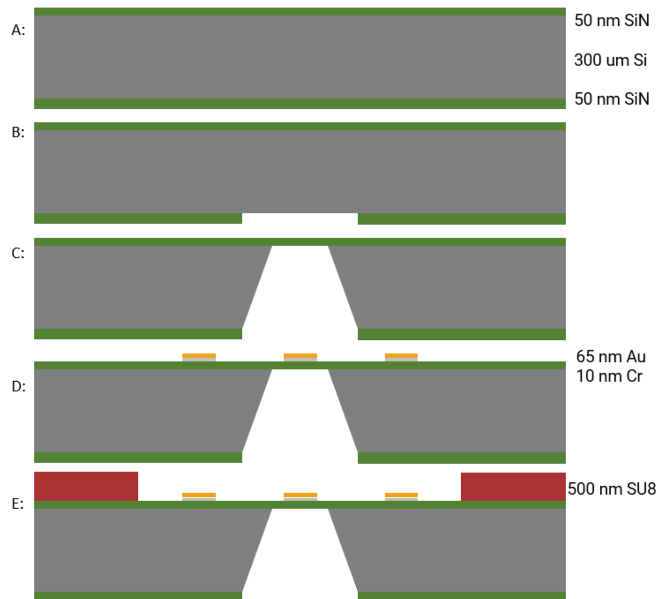

Figure 3-10 Complete fabrication process flow. See text for annotations for A-E

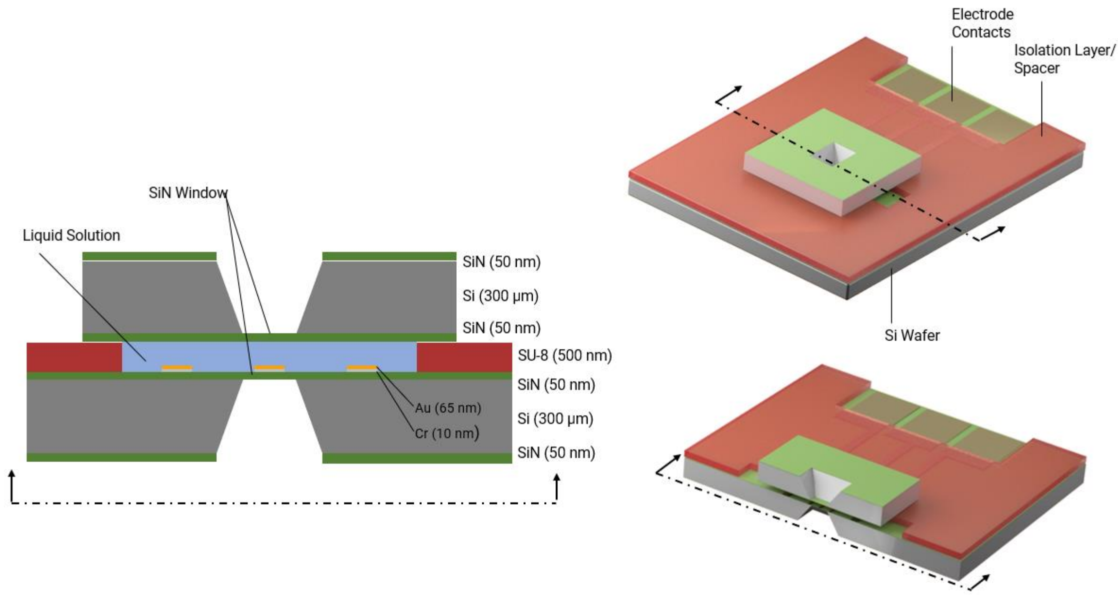

Figure 3-11 (A) Cross section view of the fabricated device, including top sealing chip and liquid. (B) Isometric draft of chip assembly. (C) Isometric draft of a cross section of the assembly. No dimensions are to scale. 3-D models constructed with the help of Patricia Nguyen (pennguyen.com)

3.2.7 Microfabrication characterization methods

Microfabricated structures were characterized for quality using a variety of different methods. Completeness of the RIE step was optically determined, as the SiN_x thin film has a unique olive brown colour, and the underlying Si is grey. Additionally, if the etch was incomplete the following KOH step would simply fail to etch through holes. The window and etch quality was determined qualitatively using an optical microscope with top illumination. Looking at the front side of the wafer, it was very easily determined if the window was broken, or if any crystal Si structures remained to be etched away.

The membrane strength was tested, as all chips are, in a leak test vacuum to ensure integrity of the SiN_x windows prior to loading into the microscope. The test is simply done by loading the custom chips into the liquid cell holder along with water, in a flowing or static configuration, and loading into a test chamber to be pumped to 10^{-6} torr. In the case of a broken or cracked membrane, the chamber pressure will not fall below 10^{-2} torr and a bubble will be seen on the sandwich through the viewing port in the test chamber.

Lithography steps, including SU-8, were characterized using both optical observation and a Tencor Alpha Step 200 with vertical sensitivity of 50 Å and maximum vertical step range of 160 µm. The alpha step was used to characterize the thickness of the PR film, and the depth of any surface non-

uniformities that developed during growth. Optically, the PR films were inspected for surface defects, delamination, edge and corner resolution, correct pattern size, etc. PR film undercutting could not be characterized without SEM cross sectional imaging, and for most fabrication steps it was unimportant and not investigated.

Metal film deposition height was measured using a crystal monitor within the sputtering system, as well as with the Alpha Step surface profiler. On some samples optical and SEM imaging was used to ensure quality of electrode sidewalls and surface coverage. A handheld Fluke Multimeter was used to test resistance between electrode traces to ensure complete etching of the gold and chromium layer.

Electrode quality was determined electrochemically using a Gamry Reference 600+ potentiometer to record the CV of the reversible redox system of 2 mM hexaammineruthenium(III) chloride ($Ru(NH_3)_6Cl_3$ in 100 mM potassium chloride (KCl) solution. Using commercially available liquid cell chips as calibration, the redox signal was characterized using Ag|AgCl RE and platinum CE in an external cell, and using the on-chip 3-gold-electrode system inside the holder for both static and flowing configurations, all at multiple scan rates. Using the Randle-Sevcik equation, peak currents versus scans rates are plotted to ensure a linear relationship, as expected from a reversible redox system with ideal electrodes. The custom chips were characterized under the same conditions.

Electrode cleaning of the custom chips was performed through the electrochemical oxidation and reduction of the gold surface in a 1 M H_2SO_4 solution, applying 80 CV cycles to the electrode.

3.3 *In situ* experiments

3.3.1 FIB samples

As discussed in the background, a small (~1 μm) hole was formed through the membrane, creating a imaging location with has no background noise contribution from the membrane materials, allowing for higher spatial resolution imaging. The hole was milled from the membrane using a Zeiss NVision 40 dual-beam FIB-SEM (Focused Ion Beam – Scanning Electron Microscope) available at the Canadian Centre of Electron Microscopy (CCEM) at McMaster University. Protochips Inc. chips were loaded and aligned using SEM for focusing. FIB exposure was minimized to prevent Ga^{+} deposition into the electrodes and sputtering of the isolation layer.

Samples were both concentric and linear electrode E-chips, with gold counter, reference, and working electrodes. One sample with a carbon WE was tested, and the Ga^+ beam ion implantation and contamination was found to damage the carbon electrode beyond use. The E-chips were prepared by removing the protective photoresist coating in an acetone bath followed by methanol bath for 2 minutes each, followed by compressed air drying and Plasma cleaning for 2 minutes in a mixture of O_2, H_2 and Ar at 30 W using a Solarus Plasma cleaner. After FIB milling, the samples were again cleaned following the same procedure to remove carbon contamination before electrodeposition and *in situ* experiments. One additional sample was tested using a pre-deposited 50 nm, sputter deposited Cu film as a protective measure against Ga^+ implantation.

FIB hole geometries varied, and included the following:0.5 μm radius hole, centered on the electrode; 1.5 μm radius holes, centered on the electrode; three 0.5 μm radius holes, located along each edge and the tip of the electrode; and a 1x3 μm oval hole, along the edge of the electrode

Samples were imaged using the SEM dual beam, with the milled holes measured under tilt-correction. The various sample geometries' effectiveness for showing the desired features will be discussed in the results section.

3.3.2 Electrodeposition of Pd structures

Palladium dendrites were grown from an 5 mM aqueous solution of H_2PdCl_4 by electrodeposition, analogous to Chronoamperometry (CA). All chemicals were purchased from Sigma-Aldrich, Saint Louis, MO, USA. 0.1 M stock solution was formed by mixing 177.33 mg of Palladium (II) chloride (≥ 99.9%), 2 mL of 1 M HCl (purchased as ACS reagent grade, 37%) and 7.956 mL Milli-Q water, followed by two hours of sonication to form a clear, dark brown liquid. Before use, the solution was bubbled for 20 mins in N_2 gas to remove dissolved oxygen.

Palladium structures were electrodeposited on the gold electrodes using a CHI 660 potentiostat from CH Instruments, Austin TX, USA at -0.2 V vs Ag|AgCl reference electrode with a platinum wire counter electrode. Deposition time was varied between 15-60 s.

3.3.3 Beam induced etching of Pd

Beam induced etching was achieved by loading the chips that had pre-deposited palladium dendrites into the Protochips Poseidon liquid cell under Milli-Q water, controlled using a syringe pump (Harvard 11 Elite standard infuse only syringe pump, Harvard Apparatus Inc., Holliston MA,

USA) at 300 μL/hr. The liquid cell was assembled with spacers between 50-500 nm, plus the 500 nm isolation layer thickness, forming 550 nm-1 μm liquid layer, not including bulging effects. The liquid cell holder was loaded into an FEI Titan 80-300 keV LB microscope, operated at 200-300 keV in STEM mode, available at the CCEM, McMaster University.

The samples were imaged under water to ensure a vacuum seal of the system and take preliminarily images of the palladium structures. The water syringe was then replaced with 1-10 mM HCl solution and flushed for approximately 10 minutes before imaging commenced. The palladium structures were imaged periodically for up to 2 hours to study native etching effects, with the beam blanked between each image. To investigate the electron beam effect, the beam was left scanning in STEM mode at a specific location, with images saved periodically for up to 1 hour.

Electrochemical oxidation was studied by applying an oxidative potential of 800 mV versus the on-chip gold reference electrode for up to 10 second intervals, with video recording of the continuous STEM scans. Secondary locations on the electrode were imaged before and after the CA to compare structural changes under oxidizing potentials with and without the electron beam. Several subsequent CA steps were applied, with the beam focused at various locations on the electrode. Electron beam currents were not recorded due to calibration challenges with the microscope. Palladium dendrite structures were imaged using a JEOL JSM-7000F SEM before and after the LCEM experiments.

3.3.4 Imaging of gold nanoparticles

The chips fabricated in this work were tested *in situ* by simple imaging of 12 nm gold nanoparticles in aqueous solution. The particles were prepared following a well developed procedure first presented in 1995[120]. All beakers and magnetic stir rods were cleaned in dilute aqua regia before use, and all chemicals were purchased from Sigma-Aldrich. 1 mM gold chloride solution was prepared by mixing 300 mL DI water with 208 μL gold chloride solution and brought to 100^0 C on a hotplate while string at 1200 rpm. 0.5 g of trisodium citrate dihydrate was mixed with 30 mL of DI water, and added to the gold chloride solution once the temperature was 100^0 C. Upon adding the sodium citrate mixture, the solution turned dark blue, followed by raspberry red within the first few minutes. After 10 minutes of heating and agitation, the solution was removed from the heat, placed in an ice bath, and continued to mix for an additional 15 mins. Nanoparticle size was confirmed via drop casting for TEM imaging using a Philips CM12 operated at 120 kV in TEM

mode, along with characterization of the optical absorption spectra, with a peak absorbance at 520 nm. 2 μL of the gold nanoparticle solution was pipetted into the liquid cell in static configuration. The system was loaded into a JEOL 2010 F TEM/STEM microscope for imaging and recording of nanoparticle motion, with no additional spacers.

3.4 Chapter conclusions

In this chapter, a process flow for the fabrication of the *in situ* liquid cells has been presented. The chosen fabrication is designed to minimize the risk of breaking the free supported membranes, and several experimental complications are addressed. Following this, the experimental details for characterization of the devices and for *in* situ studies has been stated. The protocols presented here were applied directly to generate the results to be presented in chapter 4. Any experimental details which were not included in this chapter can be found in the appendix.

4 Results and discussion

4.1 Custom liquid cell fabrication

In this section we present the results from the microfabrication to create the custom liquid cell. Chapters 2 and 3 outlined the background technology requirements and underlying physics of the microfabrication, while discussing why certain design choices were made. In this section, proof of both failed approaches and successful fabrication are presented, followed by characterization of each structure. The section concludes with a practical application of the custom chips, where they are used to image gold nanoparticles within a liquid layer, inside the liquid cell TEM.

4.1.1 Microfabrication

SiN_x etching: In Figure 4-1 we can see the very clear removal of the SiN_x (bright rectangle). The underlying Si contains several brown artifacts, and there are several faint purple streaks along the wafer surface, specifically above and to the left of the etched hole. The specs within the hole are un-etched SiN_x, which cause local masking during the following wet etch. A longer 2 min RIE over etch does not result in these marks, but no image was available. The purple lines on the surface are caused by PR which was not fully removed by chemical cleaning, which is not a concern because the following KOH readily dissolves the PR.

KOH etching: For the KOH etch, it was important to characterize the change in etch rate over time due to water evaporation, and reduced diffusion of the solvent and byproducts to the exposed Si surface from the shrinking geometry of the small holes. Preparing a 30 wt% KOH solution, the total etch depth of 7 different samples was measured once every 30 mins, with the results shown in Figure 4-2. Using the etch rate of the first sample at 1.4 µm/min, the total expected etch time is 3 hr 34 min, whereas integrating the etch rate over time using the logarithmic fit found through linear regression analysis yields a through etch time of 3 hr 46 min. Based on these calculations, the uncertainty on wafer thickness (±25 µm) plays a larger role in the etch time uncertainty than the non-uniform etch rates, which is partially attributed to the stirring of the solution and the reflux system implemented. It is worth noting the etch solution final volume was equal to the initial volume, within a small tolerance due to poor markings on the beakers.

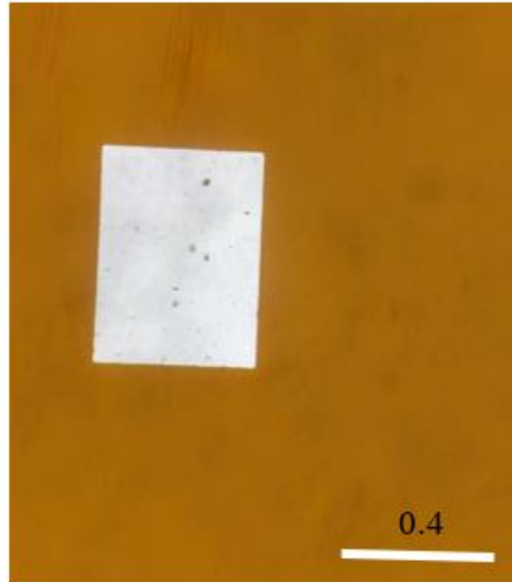

Figure 4-1 Light microscopy image of SiN wafer after 1 min RIE and removal of masking PR to open holes for membranes. Olive-brown – SiN. Grey – Si. Before KOH etching of the Si.

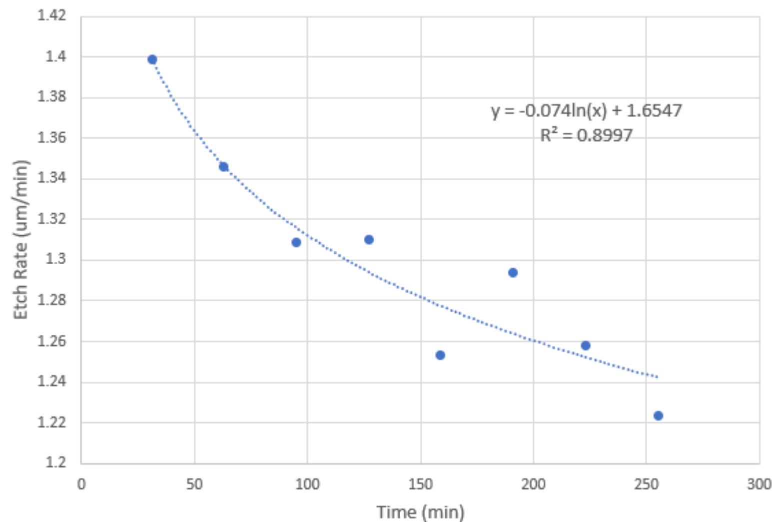

Figure 4-2 KOH etch rate over time. Each data point is a unique sample, all within the same solution. Etch depths measured using Alpha-Step Surface profiler, with ≤1 µm error.

The typical KOH etch shown in Figure 4-3 was found to etch 60 ± 3 µm within the first hour in solution, as characterized by a surface profiler. By testing several samples in individually made solutions, a total etch time of 4 hr 45 min ± 20 mins was found, with some outliers due to incomplete RIE removal of the nitride layer. Optimization of careful handling and drying yielded a consistent 55 of 57 unbroken windows, with less than 10 under-etched holes. The under etched holes contain geometry shown in Figure 4-3-D, which are useable with slight blocking of the viewing area.

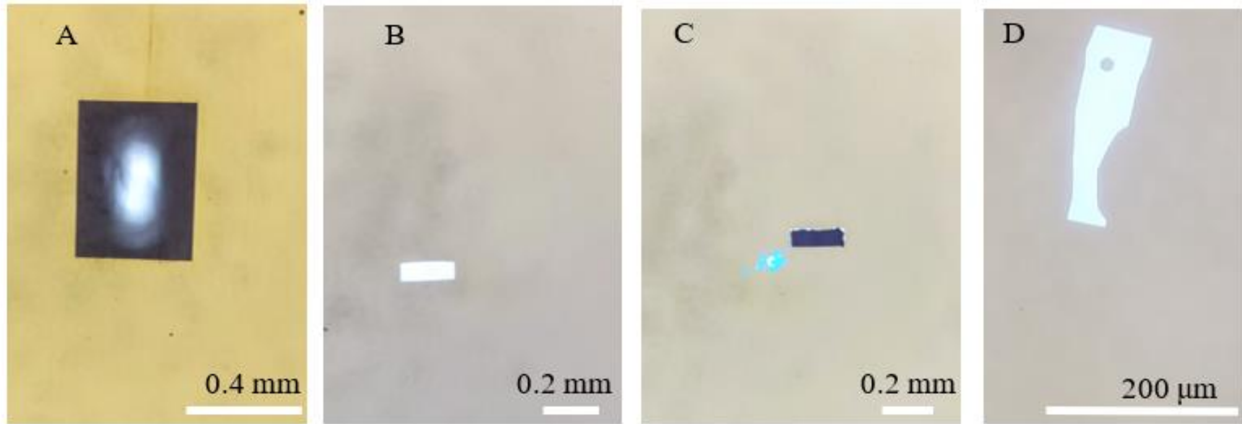

Figure 4-3 Post- KOH etching of several SiN windows. A: Back side view after etching, showing through etch into the wafer. B: Front side view of fabricated window, illumination due to optical transparency. C: Front side view of broken SiN membrane, as noted by the rough window edges and lack of reflectivity. D: Incomplete etch, as noted by the crystal structures blocking transmission of light through the window in select locations.

Electrodes: Spin coating of the window chips resulted in instant breaking of all windows above the vacuum chuck, sacrificing ~5-10 chips on each device. The broken windows became large surface defects resulting in comet-shaped structures in the PR and destroying nearby chips as well, as shown in Figure 4-4-I. Using the vinyl or Ecoflex method described previously, spin coating and lithographic patterning yielded up to 100% window survival rate on a single wafer; however, each handling step introduces a human error and a chance of catastrophic failure. Although it was possible to lithographically pattern without breaking any windows on a single wafer, in many cases an entire wafer would be destroyed. Figure 4-4 shows the result of the gold deposition followed by PR patterning under several conditions, followed by metal etching to form the electrodes.

From Figure 4-4 over etching of the metal film has a more significant impact on electrode quality than the PR deposition technique. In figures A, C and G, PR residue is seen on the bulk surface which induces localized masking effects as exaggerated by the large gold artifact in B. O_2 plasma ashing in H has shown to remove the excess undeveloped PR without thinning the masking PR sufficiently to prevent an etch out, effectively improving the etch out method. Similar ashing was applied during the PR removal after metal etching to ensure a clean electrode surface.

Using a handheld Fluke multimeter, the resistance between electrode contacts was found to be infinite, which, along with the SiN_x characteristic olive brown colour, proves complete removal of the Cr and Au between electrodes. The electrode spacing along with the insulating SiN_x is sufficient to prevent electrical cross talk between electrodes through the underlying Si. Electrode height was

confirmed using the surface profiler to be 75 ± 3 nm. Note that the samples in Figure 4-4, excluding parts I and K, do not contain windows to simplify the lithography process.

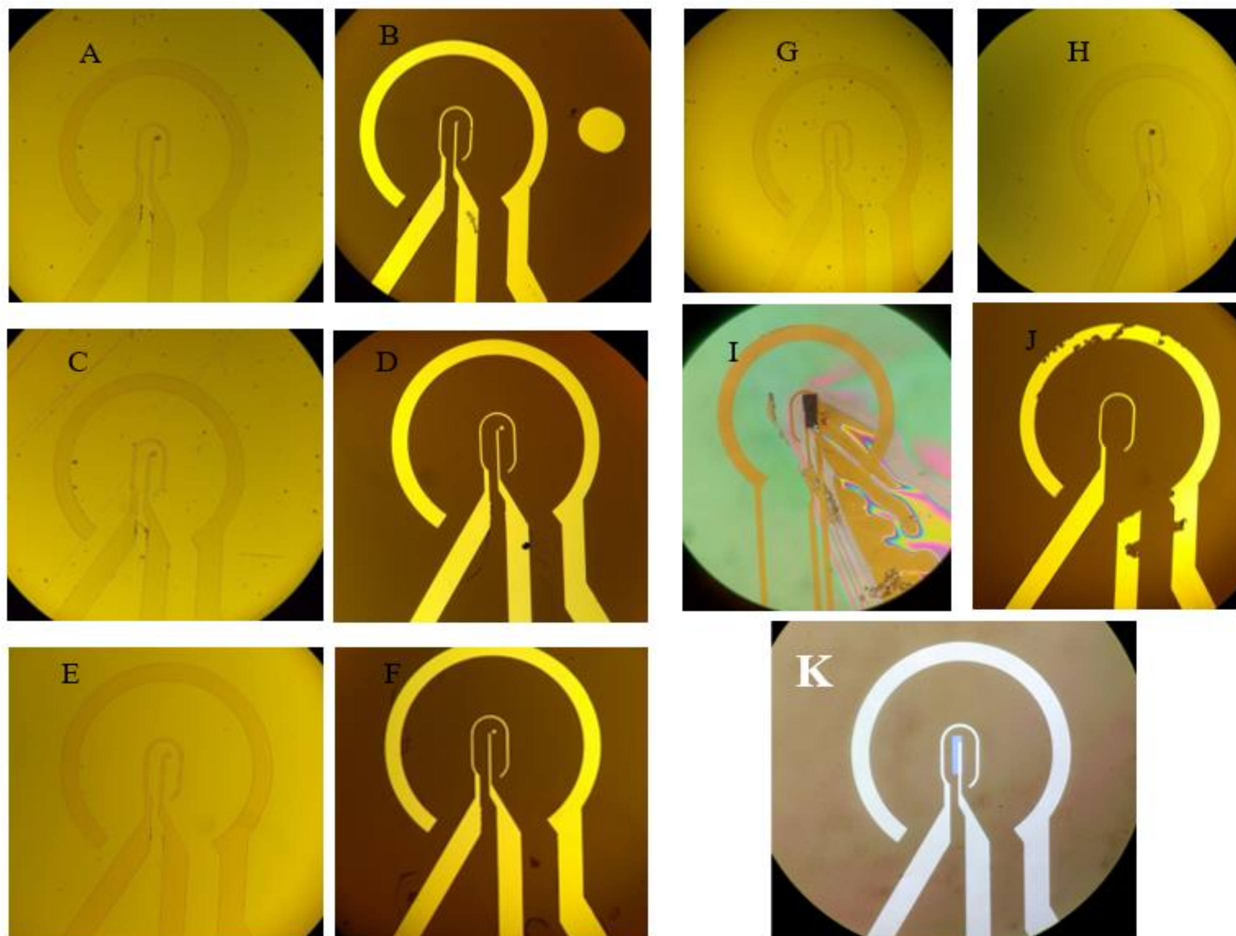

Figure 4-4 Lithographic patterning and etching of electrodes. Samples have 10nm Cr followed by 65 nm Au sputter deposited, and were masked using Microposit 1808. See chapter 3 for recipies. In figures A,C,E,G,H, PR is located on the electrodes as a hard mask, with the remainder uncoated. A-F: before/after metal etching using various PR application processing. A,B: HDMS primer used for adhesion. C,D: No primer, doubled development time. E,F: 2 mins toluene soak before hard bake. G,H: Before/after 45 s O_2 plasma ashing de-scum of excess PR. I: comet-shaped trail effects due to broken windows, no metal deposition. J: 2 mins Au and Cr overetch. K: Alignment of electrodes with the membrane, as seen by the light rectangle around the working electrode.

Isolation layer: Initial work with a SiO_2 isolation layer showed that liftoff patterning left redeposited oxide film on the wafer surface, and complete removal could not be achieved without the use of sonication. Several attempts were made to use SU-8 2000.5 series resist as the isolation layer, however the resist showed very poor adhesion to SiN_x, regardless of surface treatments. In the best case, SU-8 2000.5 formed a very patchy film approximately 100 nm thick on a 25 nm thick SiO_2 patterned substrate, with the following surface preparations: pre-bake to 120^0 C, O_2 plasma

ash for 5 mins, soft bake at 20^0 C higher than recommended temperature (90^0 C). Once an initial layer was applied with sufficient adhesion, multiple coatings of PR were able to obtain a net film thickness of ~600 nm; however, the film quality was patchy, and this technique still required the patterning of SiO_2 on the surface.

It was found that the SU-8 3005 series resist has much higher adhesion to the nitride. Using the diluted resist as explained in chapter 3, Figure 4-5 shows the film thickness changes with respect to spin coating parameters. On the films there are many 'spots' and film defects which are attributed to several factors. First, the dilute resist has low solid content and is 'spread too thin' after solvent removal, yielding a patchy film. Second, although not on these samples specifically, pin holes in the SiN_x layer which have been expanded due to KOH etching produce non-uniform surfaces, and pitting locations in the resist. Third, these samples were cleaved with a diamond blade prior to SU-8 deposition, resulting in Si debris back sputtering to the surface. This is evident by a lower density of defects near the centre of the chips. Fourth, bubbles and gasses which exist within the resist are violently evaporated during the soft or hard bake. Finally, defects in the transparency of the mask cause local under exposure of the resist, yielding local pitting during development.

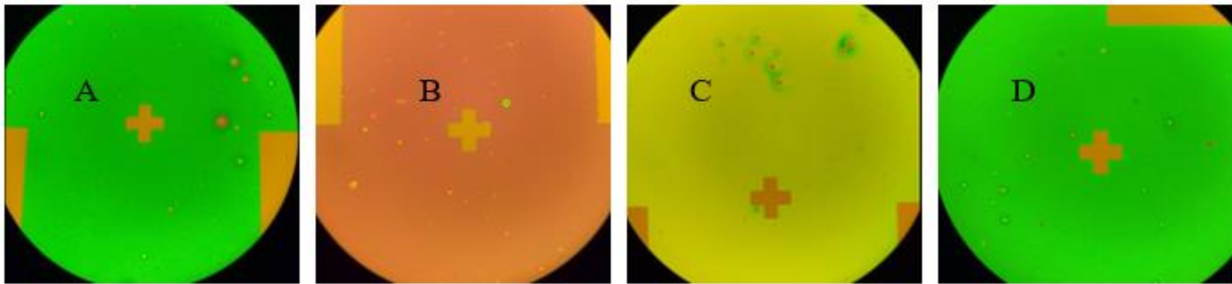

Figure 4-5 Diulted SU-8 3005 resist as an isolation layer. A: 3000 rpm for 60 s, 465 nm film. B: 4000 rpm for 60 s, 410 nm film. C: 2500 rpm for 60 s, 510 nm film. D: 3000 rpm for 30 sec, 460 nm film.

The first two issues cannot be controlled, however small defect concentrations are not problematic if the other sources can be mitigated. The third issue is not a problem for wafer-scale fabrication as the cutting will occur after deposition of the isolation layer. The fourth issue was approached by modifying the baking procedures. Rather than immediately placing wafers on the 90^0 C and 110^0 C hot plates for soft and hard bake respectively, they were first heated to 60^0 C for 1 min, followed by the regular length bake at the desired temperature. The gradual temperature increase allows less violent ejection of gasses and allows diffusion of the film to partially refill any holes formed. To minimize defects from the mask, a chrome mask or higher quality mask can be used. In this work,

emphasis was placed on cleaning the mask before and after each use to minimize any contamination. The result of these modifications is shown in Figure 4-6, with minimal film defects.

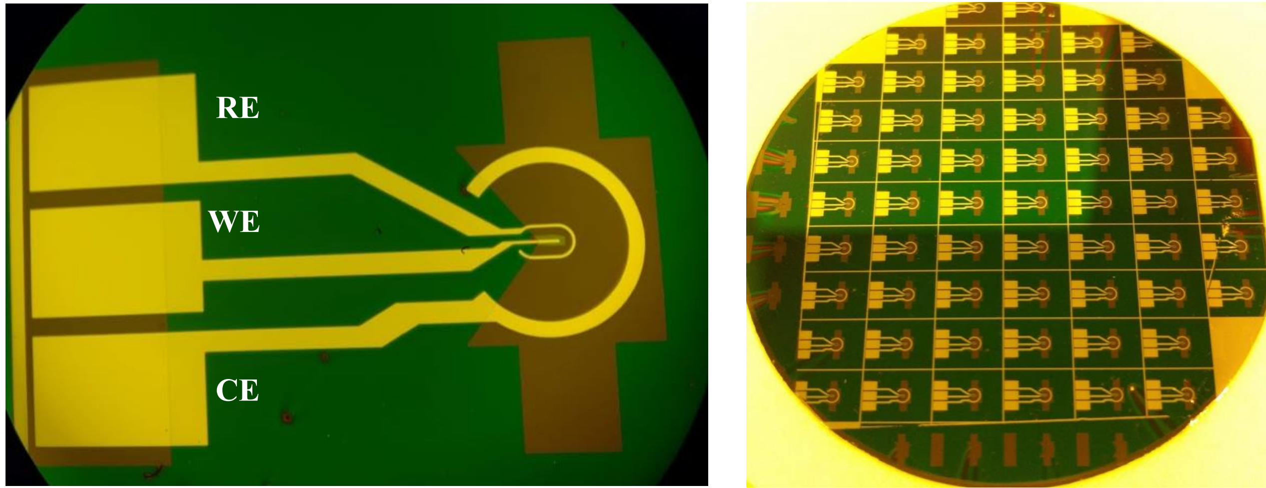

Figure 4-6 Fabrication of isolation layer from SU-8. (Left) significantly reduced surface defects in the film realtive to previous fabrication. (Right) Full-scale wafer view. The alignment structures along the edge show film defects as expected, however all internal chips show clean fabrication.

Wafer cleaving: With the complete fabrication of a wafer of chips, the challenging part became successful cleaving of the wafer without breaking the windows. It was mentioned that wire cutting and saw cutting resulted in significant vibrations which breaks all windows. Cleaving the wafer using a diamond scribe was very inaccurate over the long cleave lines, in most cases the cleave propagation would deviate to the row of windows. Using the laser, as described previously, proved to be an efficient way to cut long lines along the wafer, separating a ‘row’ of chips.

The laser cutting path is very rough, with a large kerf of damage to the surrounding areas. This damage is far from the active liquid area in the centre of this chip and would not be a problem except for one aspect: to prevent surface damage to the wafers before their use, a layer of PR was spin coated to the surface and left untreated. The protective layer is burnt by the heat from the laser, pyrolyzing into a thick carbon film nearby the cutting path and forming an insulating film over the electrode contact pads. From Figure 4-7–(Left), the bottom cut was performed using a dicing technique which does not have any noticeable local surface damage aside from Si dust deposited on the protective PR layer, motivating the combined use of both techniques to cleave the wafers. Laser cutting is therefore used to separate long strips of the chips, lengthwise, from the wafer, such that the laser cutting path does not approach any electrode contacts and any damage is limited to outside the active liquid area. Because these strips of chips are 4.5 mm wide, the cleaved distance

is across their width and is significantly shorter than the distance to the nearest window, allowing easy cleaving with a diamond scribe without fear of the cleaving line deviating to windows or any damage to electrode contact pads.

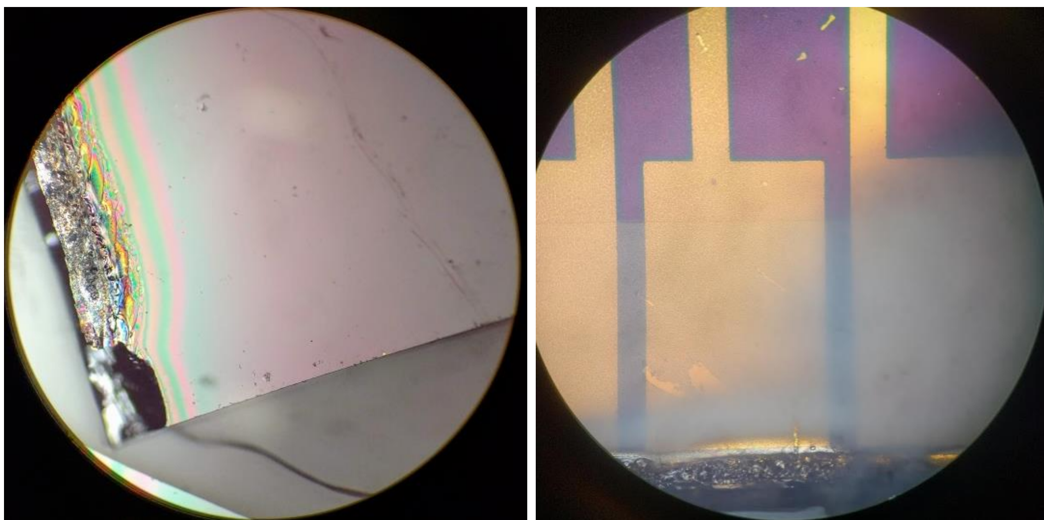

Figure 4-7 Laser and physical cleaving of individual chips from the bulk wafer. (Left) Leftmost cleave plane was performed via laser cutting, with the bottom cut performed by diamond scribe cleaving. (Right) Pyrolization of protective PR film forming an insulating coating over the nearby electrode contact pads.

With these results documented, the mask design shown in Figure 3-6 has several additional features of interest. Along the length of the chips, there is a significant gap between electrode traces which is also not covered by SU-8, shown in Figure 3-9. This creates a clear path for laser dicing the length of the chips, with no surface back reflection into the laser cavity from the lack of gold, and reduced polymers to pyrolyze from the laser heat. The width of the chips is covered in SU-8 as this does not affect the ability to cleave with a diamond scribe, and the bottom edge of the electrodes is used as a cutting guide.

In Figure 4-8 the fabrication of a carbon working electrode is shown. Parts A and B show the fabrication using a negative resist and liftoff technique forming a well-defined carbon electrode. The electrode itself is not shown after liftoff due to poor contrast on the light microscope causing it to be nearly invisible, so instead alignment markings are shown. The carbon layer was measured to be 17±5 nm thick. This process was not performed on samples with windows or gold electrode traces; however, lift off was done without use of a sonicator so it should be compatible. Figure 4-8C,D shows the result of plasma ashing the carbon for an etch out approach. To test the complete removal of the carbon after ashing, palladium was electrodeposited to the working electrode. Any carbon that was not fully removed will be in electrical contact and show palladium growth,

allowing easy visualization of the etch completeness. Figure 4-8D show that the plasma ashing did not fully remove the carbon layer from the surface, causing an electrical short between electrodes and resulting in dendritic growth over the entire sample. This is also evidenced by the blue background in Figure 4-8C rather than the characteristic olive brown of SiN_x.

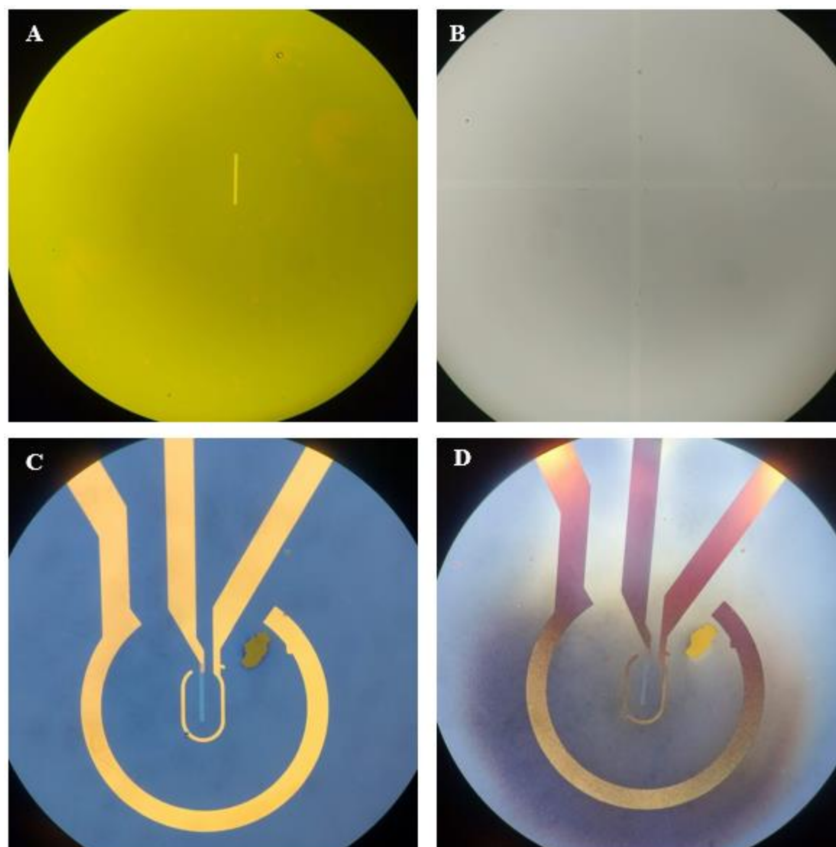

Figure 4-8 Light microscope images of fabrication of a carbon working electrodes by 2 different methods. A: Negative PR patterning and liftoff, before lift off and after deposition. B: After liftoff showing 17±5 nm carbon film. C: Carbon ashing under photoresist protection, after 20 min in O_2 ashing. D: Palladium dendrite growth on the central electrode.

These results show that the soft fabrication using plasma ashing for carbon liftoff is not a good approach to forming the carbon electrodes. The deposited carbon is electrically conductive however the electrochemically active or effective surface area was not investigated through CV. The physical lift off method appears to form a sufficient carbon electrode and more work is required to test its compatibility for high throughput fabrication with membrane devices.

4.1.2 Characterization

The first and most important structure to characterize is the window membrane quality, and the ability to resist the high pressure differences of the vacuum. This was first tested using a custom-built test vacuum within the CCEM, which contains a port for the TEM holder assembly and is

slowly pumped to 10^{-6} mbar. Several custom chips were loaded into the Protochips Poseidon holder and tested in this vacuum chamber with a water solution in static configuration, and all chips achieved a chamber pressure at or below $8.6x10^{-6}$ mbar.

Transparency of the window membranes was shown by imaging of a 12 nm gold nanoparticle solution, as fabricated in chapter 3, in static configuration using a JEOL 2010F TEM/STEM microscope, operated in TEM Mode at 200 keV. The large chips' isolation layer was 450 nm, and the small chip was a commercial Protochips sample, with no additional spacer. From the images and videos recorded, some nanoparticles are seen to be attached to the sides of the cell as a heterogeneous layer, and others are seen to be moving within the bulk, likely driven by radiolytically generated species such as gas bubbles introducing local fluid flow.

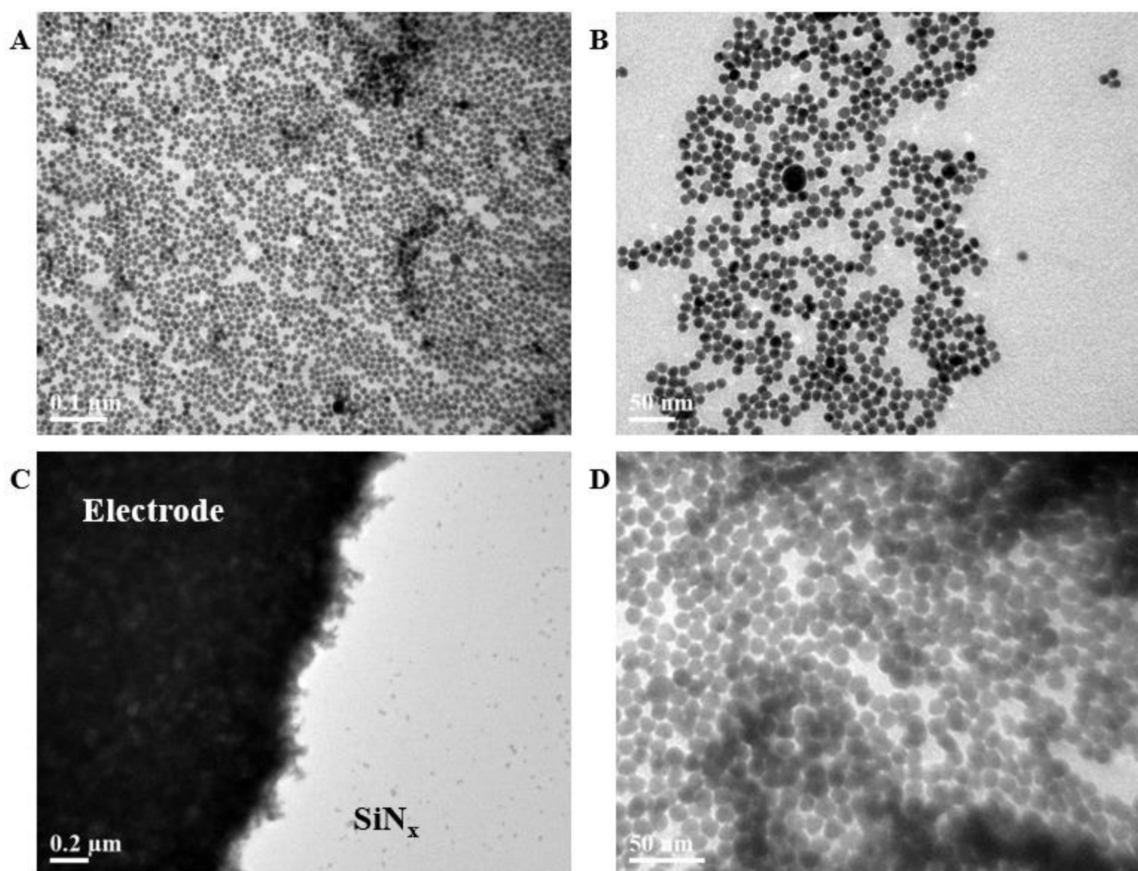

Figure 4-9 *In situ* TEM images of 12 nm gold nanoparticles imaged using custom liquid cell chips. Liquid layer Thickness of 450 nm, not including bulging. A: Low mag overview of nanoparticles. B: High magnification of nanoparticles, imaged inside a bubble or thin liquid layer. C: Edge of the gold electrode, with gold nanoparticles adhering to the surface. D: Imaging through a thick liquid layer, in focus particles are attached to the membranes, out of focus particles are floating in solution.

In Figure 4-10 we see the propagation of a 'wave' of debris within the solution pushing a cluster of nanoparticles, which is likely driven by the motion of an internal bubble. The nanoparticle motion is a further proof of the custom liquid cell viability to hold the vacuum pressures, and the imaging shows sufficient spatial resolution.

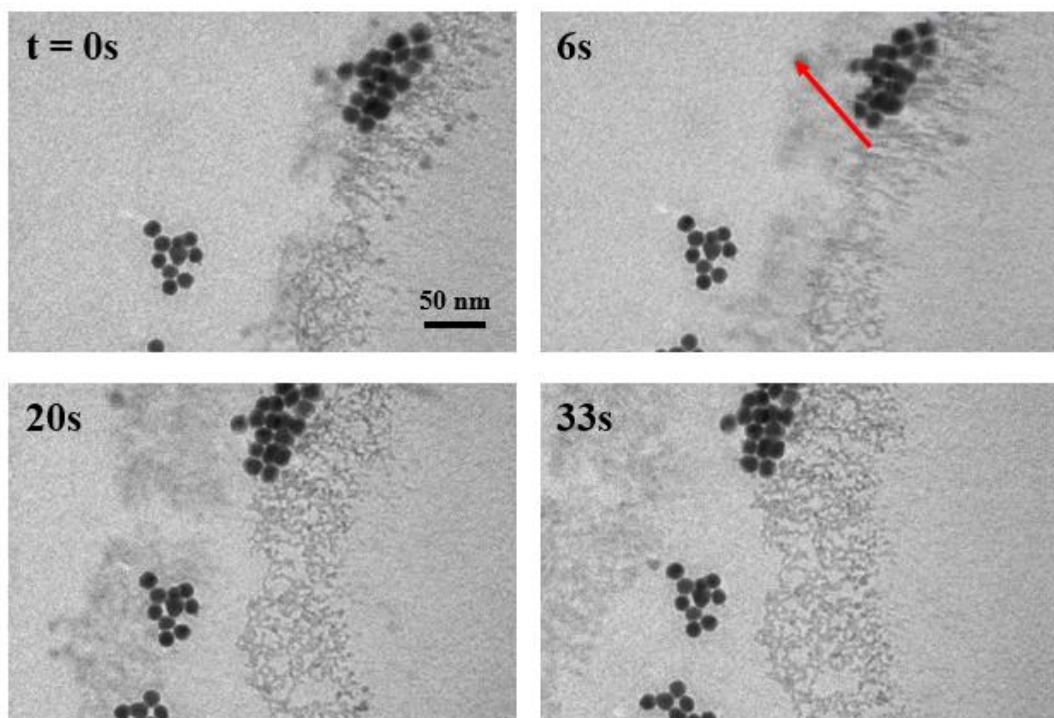

Figure 4-10 Time tracking showing the motion of particles. The vertical row of very small particles shows a bubble edge which pushed the top cluster of nanoparticles while under beam illumination.

It was mentioned extensively that utilization of gold as a reference electrode is very poor compared to a Ag|AgCl electrode. This is illustrated in Figure 4-11 with various CV scans of 2mM hexaammineruthenium(III) chloride (RuHex) and 100mM KCl. Scans are performed with both carbon and gold working electrodes, gold, platinum and Ag|AgCl reference electrodes, and both *ex situ* and *in situ* in static and flowing conditions. Scans using the gold reference electrode show a cross over effect at high scans rates, indicating drifting of the reference potential. Additionally, shown in figures C and F, the inclusion of liquid flow causes a reduced peak separation and additional overlap of the forward and reverse scan.

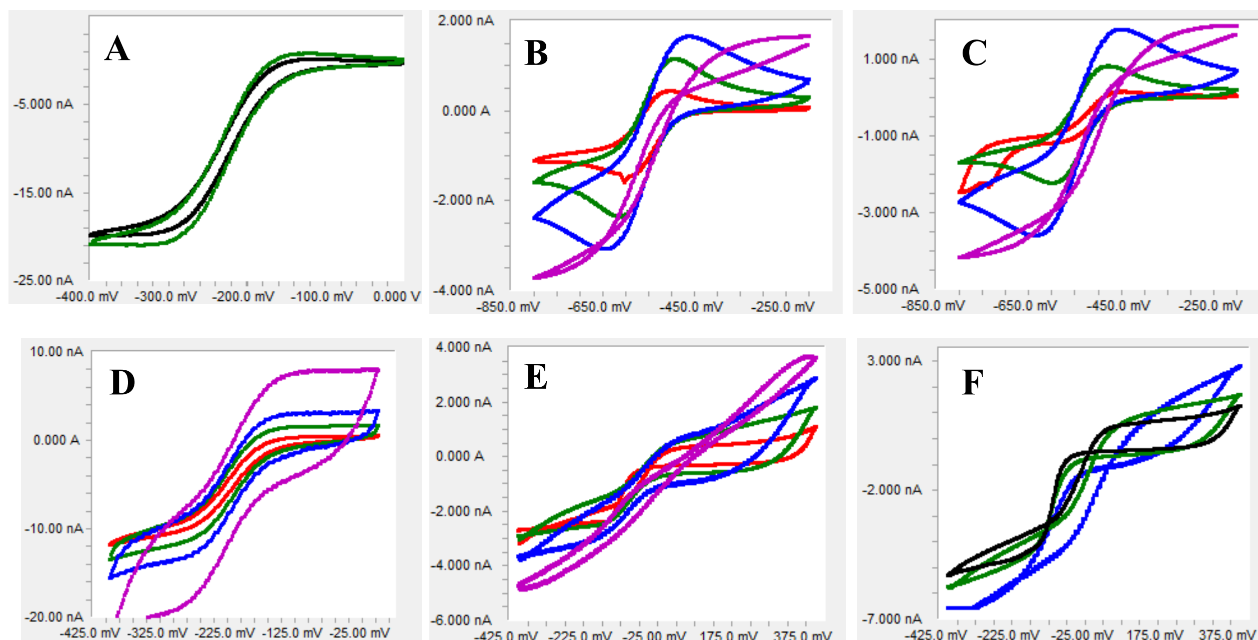

Figure 4-11 CV scans in 2mM RuHex solution and 100mM KCl for commercially available electrodes on in situ chips. Scans A-C employ a carbon working electrode. Scans D-F use a gold electrode. Scans A,D are *ex situ* vs Ag|AgCl reference electrode with platinum counter electrode. B: *in situ* vs platinum reference and counter electrodes, static solution. C: same as B with flowing solution. E: *in situ* vs Au reference and counter electrodes, static solution. F: same as E with flowing solution. Scan rates are (in mV/s) Red: 10, Black: 20, Green: 40, Blue: 100, Violet: 400.

Other interesting factors are the peak shapes comparing *ex situ* to *in situ* environments. The *ex situ* setup, employing an external Ag|AglCl RE and platinum CE in a high-volume solution, shows low current peaks indicating high diffusion properties characteristic to a microelectrode. The *in situ* experiments show a large current peak indicating low diffusion likely caused by the small solution volume and electrode spacing. Comparing the peak currents to scan rates as per the Randles-Sivcik equation in Figure 4-12 shows that at low scan rates there is a linear relationship between the peak currents and square root of the scan rate, indicating proper electrode function; however, as the scan rate increases the linearity is lost indicating loss of consistent concentration gradients throughout the system and minimal mass transport through the cell, even under flowing conditions.

These results show that even commercially available electrodes perform poorly in the micro environment of the liquid cell and great care is needed for *in situ* electrochemical experiments to replicate the *ex situ* environment. The fabrication of on surface Ag|AgCl reference electrodes will aid in reducing these errors, but has not yet been performed.

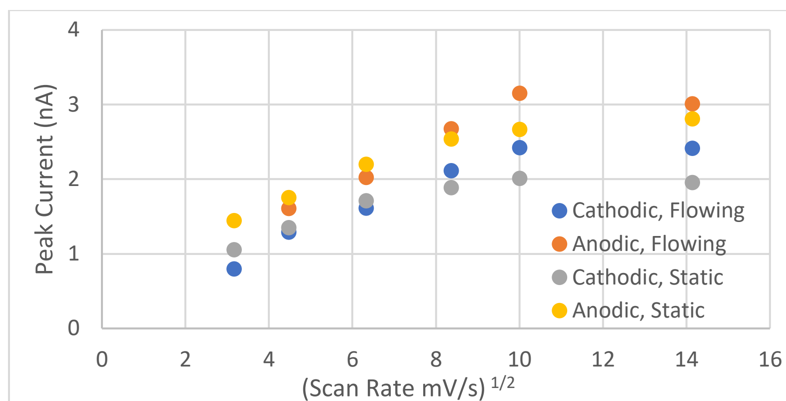

Figure 4-12 Peak currents vs scan rate for *in situ* CV using carbon working electrodes and platinum reference/counter electrodes.

The custom gold electrodes were also investigated for electrochemical activity, as shown in Figure 4-13. The electrodes were tested before and after electrochemical cleaning in sulfuric acid and physical cleaning of the contact pads. It was mentioned during the cleaving discussion that the laser heat would char photoresist to the electrode contact pads, which is evidenced in Figure 4-13B pre-cleaning with no electrical contact to the electrode. The peak currents are significantly larger than those seen on commercial samples because here the CE, with significantly larger surface area, was used to record the CVs due to poor contacts with the WEs from the laser cutting. In all scans, at ~ -400 mV vs Ag|AgCl there appears to be the start of a negative current spike which is attributed to the exposed chromium adhesion layer reducing in the solution. It is important for future work to reduce the height of the adhesion layer to minimize the signal contamination.

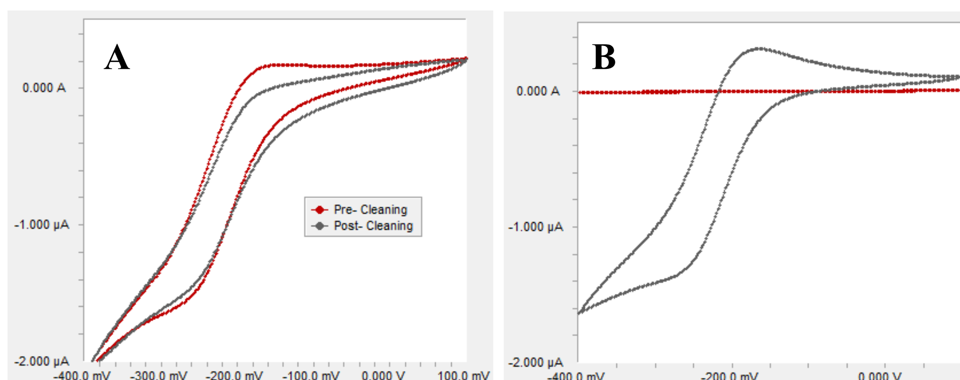

Figure 4-13 Custom electrodes shown pre- and post- electrochemical cleaning in sulfuric acid, and contact pad cleaning. Recorded *ex situ* vs Ag|AgCl reference and platinum couter electrode, in 2mM RuHex solution and 100mM KCl at 40 mV/s. See experimental section for further details.

4.2 Resolution improvement via *in situ* study of oxidative palladium etching

To test the resolution enhancement properties of the FIB hole, the beam induced oxidation of palladium nanostructures was studied *in situ*. Performing *ex situ* dendritic growth, we can see in

Figure 4-14 that the largest dendrites are grown around the edges of the electrodes, with small clusters growth near the centre, as expected from the over potential caused by higher concentration of electric field lines[49]. To showcase resolution enhancement, the FIB holes were placed along the edges of the electrodes, allowing the large dendrites to cross the hole. Using a surface profiler, the 15 s electrodeposited growth has a net height of 380 nm, including the electrode, and the 60 s growth is 770 nm tall. The dendrites from the 15 s growth protrude ~1 μm from the electrode edge, motivating these growth conditions for *in situ* characterization.

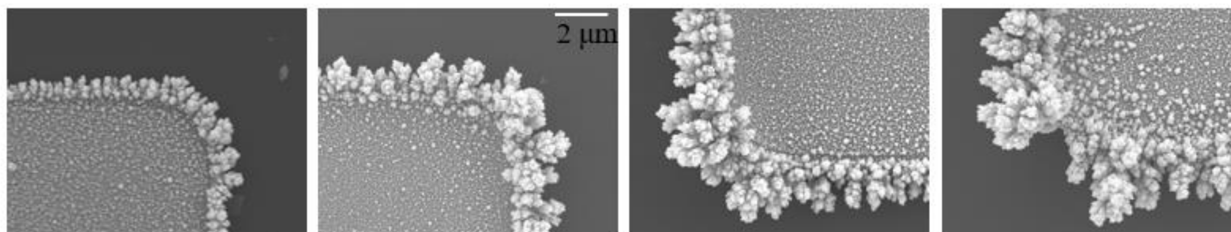

Figure 4-14 SEM images of palladium dendrites electrodeposited *ex situ* on gold electrodes. From left to right, deposition time varries from 15 s, 30 s, 45 s, 60 s. Scale bar applies to all images. SE image at 10 kV and 4.7 mm WD, taken at on the JEOL 7000F SEM, McMaster.

The FIB milled holes were tested for vacuum compatibility prior to combining them with the palladium dendrites. Several holes geometries were tested, as shown in Figure 4-15. The liquid cell was assembled with a 0-150 nm spacer under flowing DI water at a rate of 300 μL/hr, along with the built-in 500 nm liquid spacer for the electrode chips. All hole geometries showed vacuum levels below 10^{-6} mbar in the test vacuum system and showed no pressure rise measured by the octagon pump inside the Titan TEM when compared to non-hole *in situ* chips, excluding the geometry which has no electrode present.

An interesting phenomenon that may be seen in Figure 4-15-D is that around the milled hole is a rectangular section-off coloured from the rest of the electrode. This section of the carbon electrode was FIB imaged for focusing prior to milling, resulting in sputtering and Ga^{+} implantation to the electrode, damaging its structure and preventing growth of palladium dendrites during future steps. This effect was not noticed on any gold electrodes due to their higher density yielding reduced sputtering and extreme care to limit electrode exposure to the ion beam.

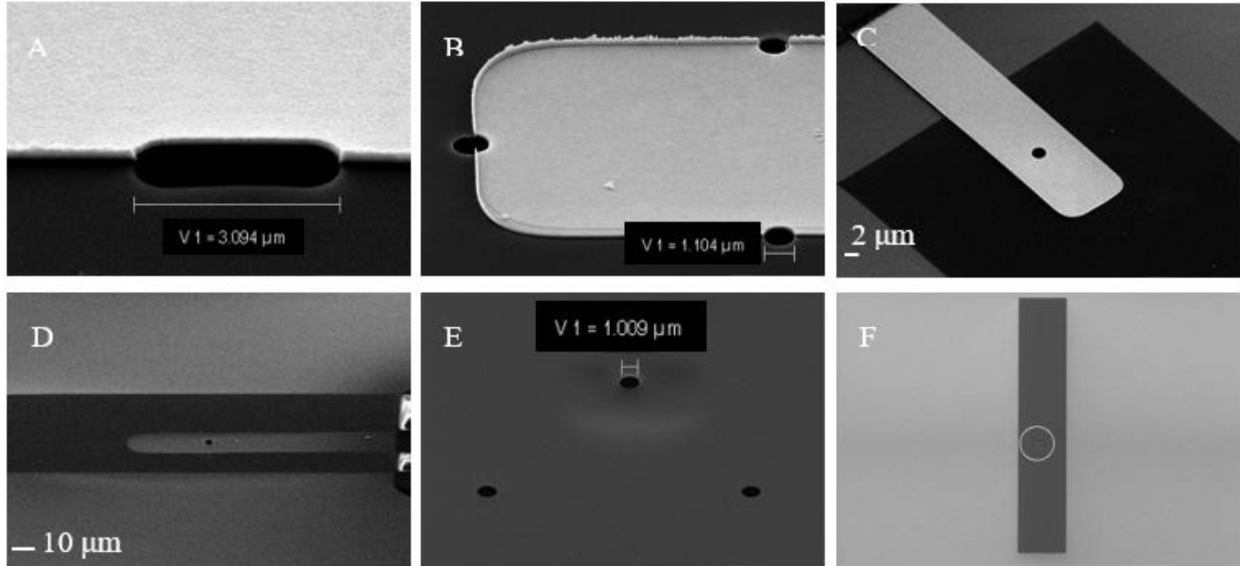

Figure 4-15 FIB hole geometries. A: Oblong hole along gold electrode edge. B: 3 holes, each 1 µm diameter around electrode edge. Note the raised sidewalls along the upper edge due to poor liftoff. C: Central hole measured to be 2.22 µm diameter, in a gold electrode. D: Central hole in carbon electrode, measured to be 3.0 µm. E: Insert of the circled region in F. No electrode present, three small holes, aproximately 10 µm spacing between holes. Secondary-electron images taken at 5kV in the SEM beam of the FIB Dual beam system. Parts A,B,C,E tilited to 54^0, with tilit corrected dimentions

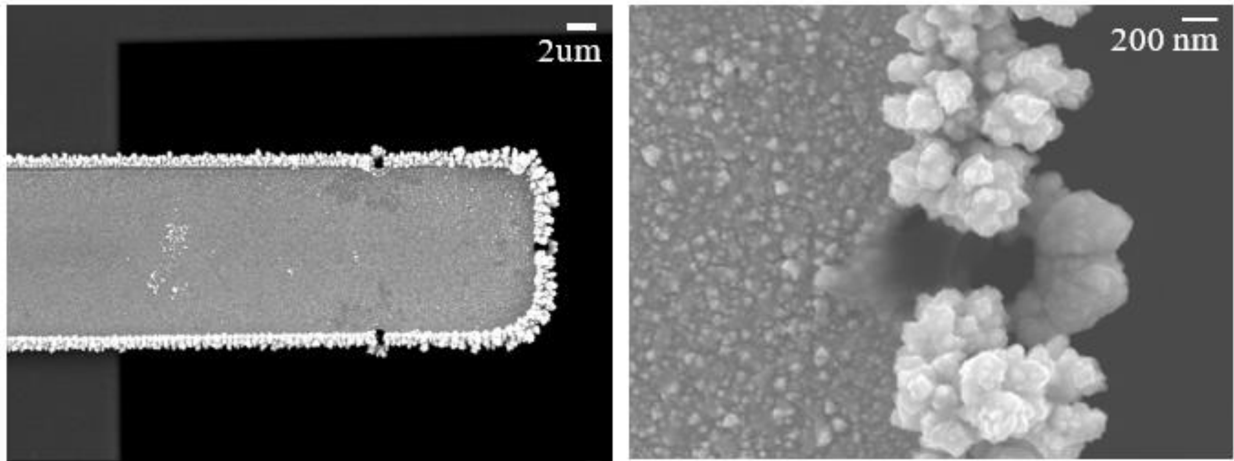

Figure 4-16 SEM Images of palladium dendrites around the FIB milled holes in Figure 4-15-D. (Left) Overview of electrode, showing large palladium growth around the edges. (Right) High magnification of the 'centre' hole at the electrode tip.

Growing Pd dendrites around the hole shows the familiar large growth on the hole edges, and additional dendrite growth along the non-electrode edge of the hole, likely caused by dendritic growth along the hole perimeter using the SiN_x as a structural support. It is interesting and unfortunate that the dendrites do not grow in the similar large cauliflower shapes around the electrode edge of the hole, likely due to the lack of a SiN_x support for growth. Longer growth conditions may form dendrites which fully cross the hole, at the cost of larger dendrites requiring thicker liquid layers and higher difficulty for *in situ* imaging.

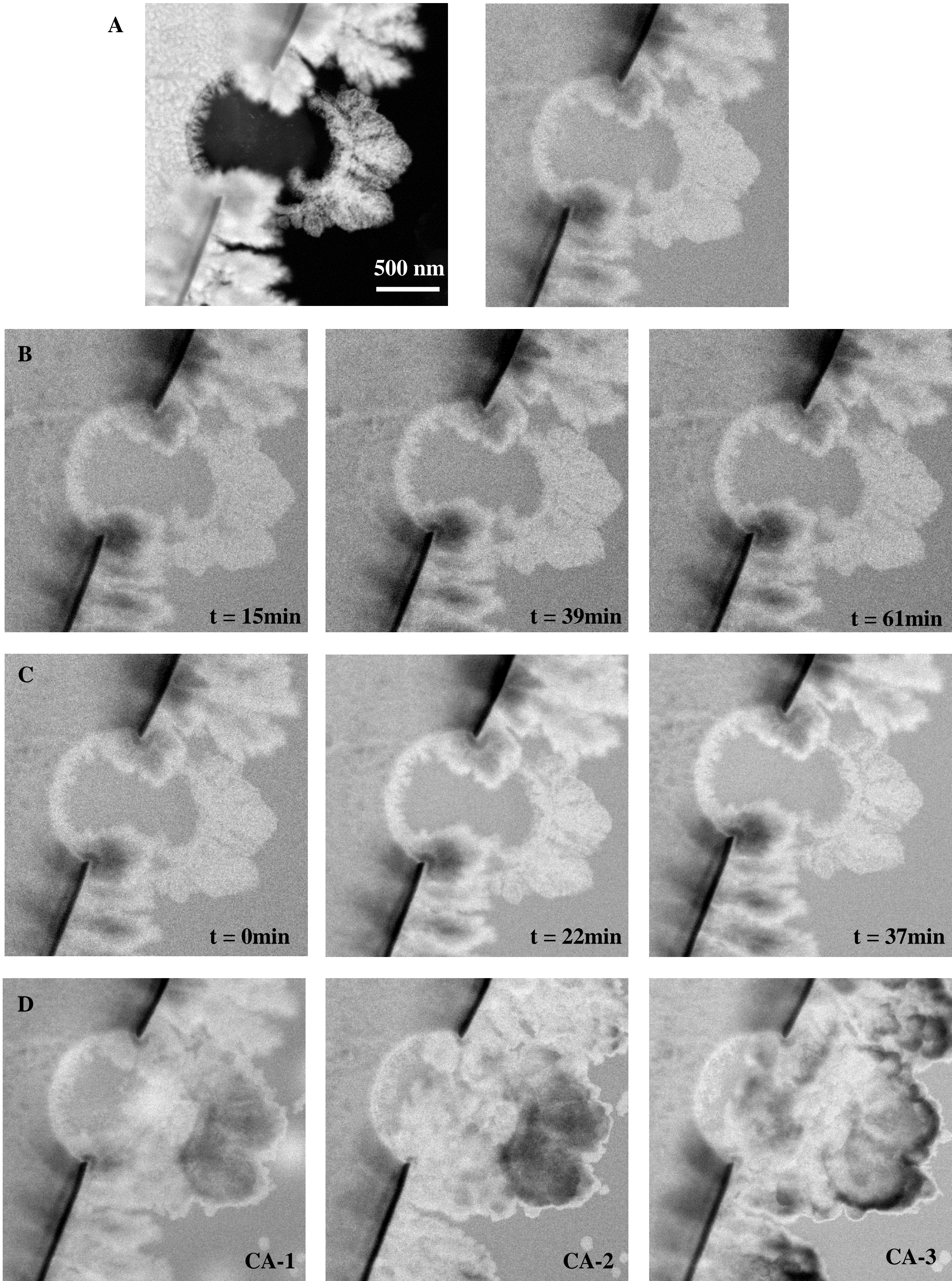
A
500 nm
B
t = 15min
t = 39min
t = 61min
C
t = 0min
t = 22min
t = 37min
D
CA-1
CA-2
CA-3

Figure 4-17 *In situ* STEM imaging and oxidative etching of palladium dendrites. Scale bar applies to all images. Row A: Dry initial image (Left) and initial image under flowing DI water (Right). Row B: Native HCl etching without presense of oxidative species, electron beam blanked between images, with one scan taken every ~10mins. Row C: HCl etching under continuous STEM beam exposure. Row D: Images after each consecuative 60 s CA scan, under continuous beam illumination for each scan.

The first conclusion from the images in Figure 4-17 is the obvious resolution loss from the inclusion of ~1 μm thick water layer (500 nm spacer, 500 nm SU8, bulging effect, subtract ~75 nm for electrode and ~300 nm for palladium dendrites), as shown in Figure 4-17 row A (left image: no liquid, right image: under flowing DI water). Many fine structures along the electrode surface and within the shape of the dendrites is lost, and the bulk water and membrane scattering yields a high noise background and lower image contrast. The resolution in the images of Figure 4-17 row A may be studied in several locations, above the electrode surface, above the SiN_x membrane, along the edges of the holes, both electrode and non-electrode side, and in the centre of the hole.

The area above the electrode surface shows the worst resolution, as expected, with dendrites nearly indistinguishable due to the high gold scattering even in the dry cell. In areas where the dendrites protrude over the SiN_x membrane the resolution is improved, but still worse than the dendrites which have grown on the SiN_x membrane, near the outer edge of the hole. Recalling chapter 2, objects deeper in the sample bulk show reduced resolution in STEM mode compared to objects near the top layer, where the electron beam first meets the sample. Additionally, the depth of focus in STEM mode is much smaller than the bulk thickness of the cell. The cell is oriented with the electrodes at the top of the cell, with the beam focused on the upper surface. The 3D dendrites protrude 'down' into the solution approximately 400 nm, becoming out of focus and allowing further beam broadening to reduce image resolution.

Comparing the resolution effect inside the hole is much more complex, as the structures which protrude over the hole have significantly different geometries than those which protrude over the SiN_x. As shown in Figure 2-5, the maximum resolution obtainable for liquid layers greater than 1 μm has negligible dependence on the 50 nm SiN_x membrane. These two factors conclude that under these experimental conditions it is not possible to quantify the resolution enhancement from holes, however the holes have been proved to function under the vacuum of the microscope. The future work in chapter 5 will address experiment modifications which will enable easier resolution quantification methods, and show the resolution enhancement to a greater degree.

We next look at the oxidative etching conditions of the dendrites. Shown in Figure 4-17 row B is the native etching over time in HCl, which over an hour of imaging does not appear to show any

significant etching as seen by the lack of contrast change or change to dendrite shapes. This is expected as no oxygen or other oxidizing species are present in the degassed, unilluminated solution. Under continuous beam illumination, shown in Figure 4-17 row C, there is clear contrast change to the dendritic structures showing etching of the palladium. Without the presence of scavengers, the electron beam generates the oxidative species H_2O_2, OH•, HO_2•, and O, with H_2O_2 followed by OH• as the most prominent, along with the reducing agents e^-_{aq}, H^+, and other OH complexes. The acidic environment reduces the aqueous electron concertation while raising the H^+ concentration. The oxidizing agents facilitate oxidative etching, forming chlorine complexes including $[PdCl_4]^{-2}$ which are soluble in solution and etch the palladium. We are confident that the 'brightening' effect is due to etching and not thinning of the liquid layer because the background contrast seen above the SiN_x membrane and gold surface remain unchanged. The brightening is caused by the palladium etching reducing the total volume of the palladium, reducing the number of electrons absorbed or scattered to very high angles, and increasing the relative number of electrons on the detectors.

Finally, the structural change was recorded during the application of an oxidative potential of +800 mV vs Au for 60 seconds seen in Figure 4-17 row D. To determine an oxidative potential vs the gold quasi-reference electrode, the Pd oxidation peak was measured to be ~250 mV vs a platinum reference using CV in HCl. RuHex CV scans were recorded using the same Pt and gold reference electrodes, measuring a 450 mV potential shift between the 2 electrodes, and shifting the Pd oxidation peak to ~700 mV vs Au. Comparing the scans after each 60 s current application while under the same beam scanning as previously shows what appears to be significant dendritic growth around the hole. Video recording was not applied during the initial scans however it is noted that most of the structural change occurred within the first 10 seconds of current application in each CA scan, with minimal change seen thereafter. The labels CA-1, CA-2 and CA-3 refer to images taken after the first, second, and third CA scans, respectively. Figure 4-18 shows post-situ SEM images further understand these changes observed.

Comparing the *post situ* images to the initial SEMs shows significant damage to the vertical dendritic structures, but what also appears to be growth of the structures along the SiN_x surface. The dendrites along the electrode edge but beside the holes have 'collapsed' over the hole forming a bridge, as seen in the TEM images as well. Figure 4-18 has three other interesting points which

yield clarification: point 1 shows exposed gold electrode, with the characteristic vertical edge from poor liftoff; point 2 shows a valley between the dendrite and the electrode edge; point 3 shows both horizontal and vertical spreading of the dendrites which lie on the SiN_x membrane. One additional observation is the decreased 'roughness' of all the dendrites, with fewer faceted edges.

From these observations, the dendrites were partially selectively etched by the HCl with preference to high aspect ratio vertices and edges, as commonly found in etching of Pd nanocubes. The current application at an over potential caused increased etching of the palladium resulting in a structural collapse of the dendrites, with several falling to the SiN_x, several to the gold electrode, and several over the electrode hole. Finally, the dendrites which reside on the SiN_x which appear to have grown, may be caused by the dissolved aqueous palladium chloride complexes reducing to solid palladium and depositing on the structure via electron beam induced nucleation and growth.

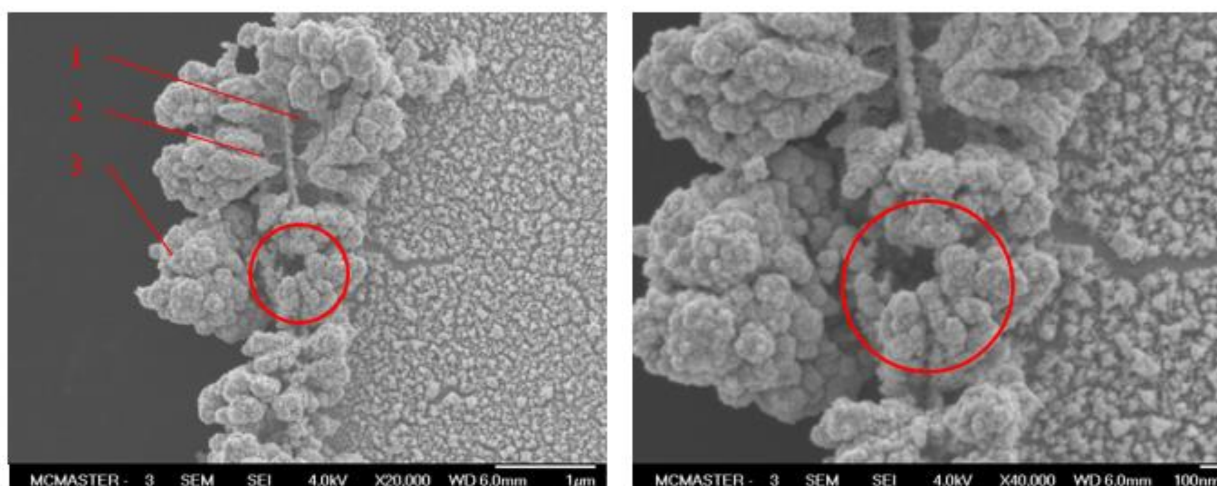

Figure 4-18 Post-situ SEM images of the palladium dendrites. Red circle marks approximate hole location. See text for descriptions of points 1, 2 and 3.

This experiment showed the effectiveness of the *in situ* technique to separate the oxidative etching parameters of aqueous oxygen, electrochemical bias, and the native chlorine etching to study the palladium evolution. In the end, the dendritic structure proved too large and required large liquid spacers, preventing very high resolution *in situ* imaging. The electric current application caused excessive structural damage preventing direct comparison of a single dendrite for pre- and post-situ analysis. Chapter 5 future work will discuss experimental modifications which will greatly improve the conclusions which may be gained from this approach.

4.3 Chapter Conclusions

In this chapter, the complete fabrication of the custom liquid cell chips was performed. It was presented that through the optimized fabrication it is possible to make ~50 devices simultaneously. The devices were tested for *in situ* compatibility by imaging aqueous gold nanoparticles inside the liquid cell TEM holder, and were found to have no complications during regular operation, in comparison to commercially available devices. The electrode characterization showed that the fabricated gold electrodes perform well after electrochemical cleaning, and that due to the micro environment and lack of a sufficient reference electrode, even the commercially available systems struggle to replicate the native operating conditions of the *ex situ* electrochemical cell.

The liquid cells were then modified by using a FIB to mill holes in the membranes. It was found that the holes are small enough to not compromise the vacuum of the microscope. Due to the experimental conditions present, it was inconclusive if the removal of the membrane scattering to the background noise was sufficient for improved spatial resolution imaging.

Finally, the oxidative etching of palladium dendrites was investigated. It was found that without the presence of oxidative species, HCl does not noticeably etch the palladium. Using the electron beam to radiolytically generate oxidizing species caused etching of the dendrites; however, the spatial resolution was not sufficient to study planar etching or blocking mechanisms. Application of an electrical bias caused a structural collapse of the dendrites, along with evidence of palladium regrowth from the dissolved species being reduced by the electron beam.

5 Conclusions

This chapter addresses the conclusions from this work, and places the achievements in the scope of the field of electron microscopy and the initial objectives of the thesis. Finally, future work which has been enabled by this research and for the improvement of these results is addressed.

5.1 Thesis summary

The initial objectives of this work were: to develop a custom *in situ* liquid cell electron microscopy platform for customization of the fabrication parameters; improve the resolution of the LCEM technique; and to apply the liquid cell to study the oxidative etching of palladium dendrites *in situ*.

Using common microfabrication techniques and facilities available at McMaster University, an optimized fabrication process flow was developed and performed for the construction of the liquid cells. The optimized flow was to construct the electron transparent membranes from SiN_x, pre-deposited on a bulk Si wafer, allowing the nitride layer to act as both a masking material to open the windows and as the windows themselves. Electrode traces and isolation layers were fabricated through the use of photolithography and wet chemical etching, with special processes developed to minimize damage and risk of breaking the fragile membranes. The micromanufacturing processes were optimized to provide high throughput and minimal risk processing at all steps. Finally, the process was developed to allow bulk manufacture of up to 57 *in situ* chips on a single Si wafer, with optimized cleaving methods to separate the devices with minimal breakages.

Investigating previous work in the field, it has been shown that the limiting resolution for liquid cell microscopy in thin liquid layers is the presence of the ideally electron transparent membrane materials. Work from the literature presented initially for SEM and ToF-SIMS (2.4.4) has shown that placing a small 3 μm or smaller hole in the membrane does not compromise the vacuum compatibility of the liquid containment, and has inspired placing an similar hole in the membranes of a TEM *in situ* LCEM system. Using a FIB to mill various geometries of apertures into the membrane, it was confirmed that the system remains vacuum compatible and liquid cell experiments may still be performed, even with volatile solvents. Experimental conditions were not optimized to highlight the resolution enhancement, which will be further addressed in the future work section.

Finally, the oxidative etching of palladium dendrites was investigated by separating the oxidative etching conditions to pre-deposited structures. Palladium dendrites were investigated in a pure HCl solution with no presence of the growth salts, and no presence of oxygen or other oxidative species. Electron beam induced radiolysis and electrochemical potentials were applied to study how altering the solution chemistry or electrical potential influences the etching conditions of the palladium, with the intent to investigate the growth/etching blocking mechanisms from the palladium chloride complexes that may form.

5.2 Thesis conclusion

In chapter 4, evidence of the complete fabrication of the liquid cells was presented. Microfabrication was optimized for increased yield of devices through the following: use of a single material for etch masking and formation of the membrane material; fabrication of a reflux system for controlled bulk Si etching; development of a soft lithography procedure to avoid breaking fragile structures; and optimization of wafer cleaving to separate devices after bulk fabrication. Through LCEM imaging of gold nanoparticles, the standard operation was found to be comparable to that of commercially available systems. The electrochemical operation was compared to that of commercially available systems through the cyclic voltammetry study of a reversible redox reaction, and it was found that further electrode cleaning is required for the gold working electrodes to function as intended. The fabrication of a carbon working electrode with gold traces and counter and reference electrodes has been attempted, and an approach for forming the carbon layer has been realized through liftoff and physical sputtering.

The resolution improvement technique of placing localized apertures through the membrane material was shown to successfully maintain the vacuum conditions of the microscope and be compatible with LCEM imaging. The experimental conditions employed large palladium dendrites which required thick liquid layers, and the resolution enhancement effect of the holes was inconclusive due to the large background noise in the system.

Through *in situ* studies followed by post-situ SEM imaging, it was noted that HCl without the presence of oxidative species shows no native etching of the palladium. Application of an electron beam generates radiolytic complexes which act as oxidative agents and allow the formation of palladium-chloride complexes, etching the palladium structures. Application of an overpotential

electric current caused catastrophic damage to the dendrites, as also seen in *post situ* SEM imaging, limiting the conclusions that may be made.

5.3 Contribution to the field

The work from this thesis has added contribution to many fields of study, most notably liquid cell microscopy as a technique, but also to micromanufacturing, electrochemical characterization and the investigation of palladium nanostructures as a catalytic material.

The custom fabrication of the liquid cell chips has shown how many 'homemade' modifications to the process flow allow high throughput fabrication. The fabrication flow showed the ease of customization to the liquid cells, including window dimensions, spacers in the sandwich setup, and variations of the electrode materials. The 'homemade' techniques developed to preserve the fragile structures may be applied in other MEMS projects with similar free-standing membranes. The custom fabrication will ideally reduce the cost of LCEM as a technique to future researchers allowing for continued research.

The inclusion of a hole in the SiN_x membrane offers an alternative design to 2D materials to approach very high resolution liquid cell imaging. As the background discussed in detail, 2D materials as membranes still suffer significant challenges to form large viewing areas and controllable liquid layer dimensions, with no work yet presented combining 2D materials with flowing solutions. The incorporation of holes in SiN_x membranes provides a very easy alternative to improving liquid cell resolution which is fully compatible with existing LCEM technologies and offers high control of liquid layers and electrical bias.

Finally, the experimental work showing the etching of palladium nanostructures demonstrates the ability to separate experimental conditions within the liquid cell to isolate specific electrochemical conditions, and demonstrates a new platform for the investigation of dendritic evolution with high spatial and temporal resolution.

5.4 Future work

This concluding section addresses the work which has been made available due to the conclusions of this thesis, and offers experimental protocols which may further improve and demonstrate the objectives of this thesis.

The most obvious future work is the continued development of the custom made liquid cell. As shown in the results section, the electrode characteristics are not ideal for a three electrode electrochemical system, especially with the existence of a gold reference electrode and working electrode. Through further micromanufacturing processes presented in the background, the reference electrode may be replaced with a quasi-silver silver chloride reference electrode for improved control over electrochemical dynamics. The gold electrode can be replaced with a carbon electrode, which is much less dense than gold, allowing for improved imaging through the electrode. Optimizing the process of replacing electrode materials will allow for the inclusion of any working electrode, including metals and custom alloys, and allowing LCEM to become a common place characterization technique in many fields of materials research. Evidence was presented for a viable process of forming carbon electrodes, which may be continued for compatibility with the complete process flow. Additionally, the final mask presented for the electrode fabrication allows for bulk electrochemical treatment of the working and reference electrodes, which was not tested for functionality.

Improving the method for cleaving the Si wafer into individual devices should also be improved. Although the process mentioned has high throughput, the precision and quality are not on par with current MEMS standards. Utilizing laser cutting systems designed for cutting silicon or further experimentation with diamond saws will improve the cleaving quality and simplify the process.

The holey membranes presented in this work were not quantified to have improved resolution over the regular system. To this end, it is worth investigating their use in an environment which better emphasises the background noise generated by the membrane materials. Taking a very thin system of study, with liquid layers less than 100 nm for the investigation of structures with features smaller than the current resolution of a few nanometers, the resolution enhancement may be better quantified. The improved spatial resolution achieved may help with all fields of study.

Aside from providing atomic level resolution in the liquid cell, an interesting application being investigated by other members in the research group is the study of surface plasmon resonance for surfaces in contact with a water layer after the fabrication of custom plasmonic structures. For this application, the existence of membrane materials will interfere with the plasmon resonance, complicating the EELS processing.

6 References

1. Williamson, M. J., Tromp, R. M., Vereecken, P. M., Hull, R. & Ross, F. M. Dynamic microscopy of nanoscale cluster growth at the solid–liquid interface. *Nat. Mater.* **2**, 532–536 (2003).
2. Borisenko, N., Zein El Abedin, S. & Endres, F. In Situ STM Investigation of Gold Reconstruction and of Silicon Electrodeposition on Au(111) in the Room Temperature Ionic Liquid 1-Butyl-1-methylpyrrolidinium Bis(trifluoromethylsulfonyl)imide. *J. Phys. Chem. B* **110**, 6250–6256 (2006).
3. Kibler, L. ., Cuesta, A., Kleinert, M. & Kolb, D. . In-situ STM characterisation of the surface morphology of platinum single crystal electrodes as a function of their preparation. *J. Electroanal. Chem.* **484**, 73–82 (2000).
4. Zheng, J., Li, X., Gu, R. & Lu, T. Comparison of the Surface Properties of the Assembled Silver Nanoparticle Electrode and Roughened Silver Electrode. *J. Phys. Chem. B* **106**, 1019–1023 (2002).
5. Auletta, T. New Tools for Nanotechnology: From Single Molecule Chemistry to Surface Patterning. (University of Twente, 2003).
6. Eaton, P. *Frequently Asked Questions about Atomic Force Microscopy*. (2010).
7. Wagner, J. B., Cavalca, F., Damsgaard, C. D., Duchstein, L. D. L. & Hansen, T. W. Exploring the environmental transmission electron microscope. *Micron* **43**, 1169–1175 (2012).
8. Liu, K.-L. *et al.* Novel microchip for in situ TEM imaging of living organisms and bio-reactions in aqueous conditions. *Lab. Chip* **8**, 1915 (2008).
9. Radisic, A., Vereecken, P. M., Hannon, J. B., Searson, P. C. & Ross, F. M. Quantifying Electrochemical Nucleation and Growth of Nanoscale Clusters Using Real-Time Kinetic Data. *Nano Lett.* **6**, 238–242 (2006).
10. Radisic, A., Ross, F. M. & Searson, P. C. In Situ Study of the Growth Kinetics of Individual Island Electrodeposition of Copper. *J. Phys. Chem. B* **110**, 7862–7868 (2006).
11. Zheng, H. *et al.* Observation of Single Colloidal Platinum Nanocrystal Growth Trajectories. *Science* **324**, 1309–1312 (2009).
12. Peckys, D. B., Veith, G. M., Joy, D. C. & de Jonge, N. Nanoscale Imaging of Whole Cells Using a Liquid Enclosure and a Scanning Transmission Electron Microscope. *PLoS ONE* **4**, e8214 (2009).
13. Donev, E. U. & Hastings, J. T. Electron-Beam-Induced Deposition of Platinum from a Liquid Precursor. *Nano Lett.* **9**, 2715–2718 (2009).
14. Jonge, N. d., Peckys, D. B., Kremers, G. J. & Piston, D. W. Electron microscopy of whole cells in liquid with nanometer resolution. *Proc. Natl. Acad. Sci.* **106**, 2159–2164 (2009).
15. FEI Company. *All you need to know about electron microscopy*. (FEI Company, 10/06).
16. ZEISS. *Education in Microscopy and Digital Imaging*.
17. Russell, S. D. Principles and Techniques of Transmission Electron Microscopy. (2018).

18. de Jonge, N. Theory of the spatial resolution of (scanning) transmission electron microscopy in liquid water or ice layers. *Ultramicroscopy* **187**, 113–125 (2018).

19. de Jonge, N., Poirier-Demers, N., Demers, H., Peckys, D. B. & Drouin, D. Nanometer-resolution electron microscopy through micrometers-thick water layers. *Ultramicroscopy* **110**, 1114–1119 (2010).

20. Rose, A. Television Pickup Tubes and the Problem of Vision. in *Advances in Electronics and Electron Physics* **1**, 131–166 (Elsevier, 1948).

21. *Vision Human and Electronic.* (Springer Verlag, 2013).

22. Giesel, F. Ueber Radium und radioactive Stoffe. *Berichte Dtsch. Chem. Ges.* **35**, 3608–3611 (1902).

23. Le Caër, S. Water Radiolysis: Influence of Oxide Surfaces on H2 Production under Ionizing Radiation. *Water* **3**, 235–253 (2011).

24. Woehl, T. J. & Abellan, P. Defining the radiation chemistry during liquid cell electron microscopy to enable visualization of nanomaterial growth and degradation dynamics: DEFINING THE RADIATION CHEMISTRY DURING LCEM. *J. Microsc.* **265**, 135–147 (2017).

25. Abellan, P. *et al.* Factors influencing quantitative liquid (scanning) transmission electron microscopy. *Chem Commun* **50**, 4873–4880 (2014).

26. Woehl, T. J., Evans, J. E., Arslan, I., Ristenpart, W. D. & Browning, N. D. Direct *in Situ* Determination of the Mechanisms Controlling Nanoparticle Nucleation and Growth. *ACS Nano* **6**, 8599–8610 (2012).

27. Yuk, J. M. *et al.* High-Resolution EM of Colloidal Nanocrystal Growth Using Graphene Liquid Cells. *Science* **336**, 61–64 (2012).

28. Park, J. *et al. Liquid cell electron microscopy: Chapter 19: High Resolution in the Graphene Liquid Cell*. (2017).

29. Cameron Varano, A. *et al.* Visualizing virus particle mobility in liquid at the nanoscale. *Chem. Commun.* **51**, 16176–16179 (2015).

30. Adiga, V., Dunn, G., Zettl, Alex & Alivisatos, A. P. Liquid flow cells having graphene on nitride for microscopy.

31. Jensen, E., Burrows, A. & Mølhave, K. Monolithic Chip System with a Microfluidic Channel for In Situ Electron Microscopy of Liquids. *Microsc. Microanal.* **20**, 445–451 (2014).

32. Jensen, E. & Mølhave, K. Encapsulated Liquid Cells for Transmission Electron Microscopy. in *Liquid Cell Electron Microscopy* (ed. Ross, F. M.) 35–55 (Cambridge University Press, 2016). doi:10.1017/9781316337455.003

33. Ross, F. M. Opportunities and challenges in liquid cell electron microscopy. *Science* **350**, aaa9886–aaa9886 (2015).

34. Yang, J. In situ Transmission Electron Microscopy Characterization of Dynamic Processes Involving Nanoscale Materials. (McMaster University, 2018).

35. Zhu, G.-Z. *et al.* In Situ Liquid Cell TEM Study of Morphological Evolution and Degradation of Pt–Fe Nanocatalysts During Potential Cycling. *J. Phys. Chem. C* **118**, 22111–22119 (2014).

36. Gu, M. *et al.* Demonstration of an Electrochemical Liquid Cell for Operando Transmission Electron Microscopy Observation of the Lithiation/Delithiation Behavior of Si Nanowire Battery Anodes. *Nano Lett.* **13**, 6106–6112 (2013).

37. Chee, S. W., Duquette, D. J., Ross, F. M. & Hull, R. Metastable Structures in Al Thin Films Before the Onset of Corrosion Pitting as Observed using Liquid Cell Transmission Electron Microscopy. *Microsc. Microanal.* **20**, 462–468 (2014).

38. Abellan, P. *et al.* Probing the Degradation Mechanisms in Electrolyte Solutions for Li-Ion Batteries by in Situ Transmission Electron Microscopy. *Nano Lett.* **14**, 1293–1299 (2014).

39. White, E. R., Mecklenburg, M., Singer, S. B., Aloni, S. & Regan, B. C. Imaging Nanobubbles in Water with Scanning Transmission Electron Microscopy. *Appl. Phys. Express* **4**, 055201 (2011).

40. Yang, J., Andrei, C. M., Botton, G. A. & Soleymani, L. In Liquid Observation and Quantification of Nucleation and Growth of Gold Nanostructures Using in Situ Transmission Electron Microscopy. *J. Phys. Chem. C* **121**, 7435–7441 (2017).

41. Park, J. H. *et al.* Control of Electron Beam-Induced Au Nanocrystal Growth Kinetics through Solution Chemistry. *Nano Lett.* **15**, 5314–5320 (2015).

42. Alloyeau, D. *et al.* Unravelling Kinetic and Thermodynamic Effects on the Growth of Gold Nanoplates by Liquid Transmission Electron Microscopy. *Nano Lett.* **15**, 2574–2581 (2015).

43. Grdeń, M., Łukaszewski, M., Jerkiewicz, G. & Czerwiński, A. Electrochemical behaviour of palladium electrode: Oxidation, electrodissolution and ionic adsorption. *Electrochimica Acta* **53**, 7583–7598 (2008).

44. Gimeno, Y. *et al.* Electrochemical Formation of Palladium Islands on HOPG: Kinetics, Morphology, and Growth Mechanisms. *J. Phys. Chem. B* **106**, 4232–4244 (2002).

45. Wojnicki, M. & Fitzner, K. Kinetic modeling of the adsorption process of Pd(II) complex ions onto activated carbon. *React. Kinet. Mech. Catal.* **124**, 453–468 (2018).

46. Zalineeva, A., Baranton, S., Coutanceau, C. & Jerkiewicz, G. Octahedral palladium nanoparticles as excellent hosts for electrochemically adsorbed and absorbed hydrogen. *Sci. Adv.* **3**, e1600542 (2017).

47. Jiang, Y. *et al.* In situ Study of Oxidative Etching of Palladium Nanocrystals by Liquid Cell Electron Microscopy. *Nano Lett.* **14**, 3761–3765 (2014).

48. Zhang, J. *et al.* Shape-Controlled Synthesis of Palladium Single-Crystalline Nanoparticles: The Effect of HCl Oxidative Etching and Facet-Dependent Catalytic Properties. *Chem. Mater.* **26**, 1213–1218 (2014).

49. Yang, J. Electron Microscopy. (McMaster University, 2018).

50. Liu, B. *et al.* In situ chemical probing of the electrode–electrolyte interface by ToF-SIMS. *Lab Chip* **14**, 855–859 (2014).

51. Yang, L., Yu, X.-Y., Zhu, Z., Iedema, M. J. & Cowin, J. P. Probing liquid surfaces under vacuum using SEM and ToF-SIMS. *Lab. Chip* **11**, 2481 (2011).

52. Yang, L., Yu, X.-Y., Zhu, Z., Thevuthasan, T. & Cowin, J. P. Making a hybrid microfluidic platform compatible for *in situ* imaging by vacuum-based techniques. *J. Vac. Sci. Technol. Vac. Surf. Films* **29**, 061101 (2011).

53. Nave, C. Surface Tension. *Hyperphysics* (2017).

54. Davis, E. J. A history and state-of-the-art of accommodation coefficients. *Atmospheric Res.* **82**, 561–578 (2006).

55. Rottlander, H., Umrath, W. & Voss, G. *Fundamentals of leak detection*. (Leybold GmbH, 2016).

56. Kersevan, R. Tutorial on Gas Flow, Conductance, Pressure Profiles. (2017).

57. Engineering ToolBox. *Speed of sound - online calculator*.

58. Varian, Inc. *Vacuum Solutions for Electron Microscopy Applications*. (Agilent Technologies, 2005).

59. Heinemann, K. & Poppa, H. An ultrahigh vacuum multipurpose specimen chamber with sample introduction system for *i n s i t u* transmission electron microscopy investigations. *J. Vac. Sci. Technol. Vac. Surf. Films* **4**, 127–136 (1986).

60. Atkins, P. W., De Paula, J. & Keeler, J. *Atkins' Physical chemistry*. (Oxford University Press, 2018).

61. Andrus, J. & Bond, L. W. Photoengraving in Transistor Fabrication. *C Van Nostrand* **3**, (1958).

62. *Handbook of silicon wafer cleaning technology*. (William Andrew, 2008).

63. Williams, K. R., Gupta, K. & Wasilik, M. Etch rates for micromachining processing-part II. *J. Microelectromechanical Syst.* **12**, 761–778 (2003).

64. Wafer Pro. How Silicon Wafers are cleaned. *Silicon Wafers* (2017).

65. Mack, C. A. *Fundamental principles of optical lithography: the science of microfabrication*. (Wiley, 2007).

66. *Baking Steps in Photoresists Processing*. (MicroChemicals, 2013).

67. Dammel, R. *Diazonaphthoquinone-based resists*. (SPIE Optical Engineering Press, 1993).

68. Microchemicals. *HMDS*. (Microchemicals).

69. Parija, B. & Panigrahi, S. Fundamental understanding and modeling of spin coating process : A review. **83**, 493–502 (2009).

70. Stevens, J., Olgado, D., Ko, A. & Mok, Y.-F. E. Edge bead removal/spin rine dry (EBR/SRD) module.

71. Barron, A. R. *Composition and Photochemical Mechanisms of Photoresists*. (Rice University, 2009).

72. Javey, A. Microfabrication Technology; Section 2: Lithography. (2008).

73. Johnson, P. & Christy, R. Optical constants of transition metals: Ti, V, Cr, Mn, Fe, Co, Ni, and Pd. *Phys. Rev. B* **9**, 5056–5070 (1974).

74. *Lithography Trouble Shooter*. 22 (MicroChemicals, 2012).

75. *Microposit 351 Developer*. (Rohm and Haas Electronic Materials, 2004).

76. *Hardbake of Photoresist Structures*. (MicroChemicals, 2013).

77. Ostling, M. Lecture 7: Etching. (2013).

78. Javey, Ali. Microfabrication Technology; Section 3: Etching. (2008).

79. Pace, M. *KOH etch rate calculator*. (2013).

80. Thong, J. T. L., Choi, W. K. & Chong, C. W. TMAH etching of silicon and the interaction of etching parameters. *Sens. Actuators Phys.* **63**, 243–249 (1997).

81. *Silicon Etching in TMAH*. (Micronova, 2015).

82. Wu, X.-P., Wu, Q.-H. & Ko, W. H. A study on deep etching of silicon using ethylene-diamine-pyrocatechol-water. *Sens. Actuators* **9**, 333–343 (1986).

83. Cui, B. Chapter 10: Etching. (2010).

84. Monteiro, T., Kastytis, P., Gonçalves, L., Minas, G. & Cardoso, S. Dynamic Wet Etching of Silicon through Isopropanol Alcohol Evaporation. *Micromachines* **6**, 1534–1545 (2015).

85. Seidel, H. Anisotropic Etching of Crystalline Silicon in Alkaline Solutions. *J. Electrochem. Soc.* **137**, 3612 (1990).

86. Merlos, A., Acero, M., Bao, M. H., Bausells, J. & Esteve, J. TMAH/IPA anisotropic etching characteristics. *Sens. Actuators Phys.* **37–38**, 737–743 (1993).

87. Cheung, N. Etching. (2010).

88. Shikida, M., Sato, K., Tokoro, K. & Uchikawa, D. Differences in anisotropic etching properties of KOH and TMAH solutions. *Sens. Actuators Phys.* **80**, 179–188 (2000).

89. Alvi, P. . *et al.* A STUDY ON ANISOTROPIC ETCHING OF (100) SILICON IN AQUEOUS KOH SOLUTION. *Int. J. Chem. Sci.* **6**, 1168–1176 (2008).

90. Zubel, I. & Kramkowska, M. Etch rates and morphology of silicon (h k l) surfaces etched in KOH and KOH saturated with isopropanol solutions. *Sens. Actuators Phys.* **115**, 549–556 (2004).

91. Dutta, S. *et al.* Comparison of etch characteristics of KOH, TMAH and EDP for bulk micromachining of silicon (110). *Microsyst. Technol.* **17**, 1621–1628 (2011).

92. Nojiri, K. Mechanism of Dry Etching. in *Dry Etching Technology for Semiconductors* 11–30 (Springer International Publishing, 2015). doi:10.1007/978-3-319-10295-5_2

93. Veselov, D. S., Bakun, A. D. & Voronov, Y. A. Reactive ion etching of silicon using low-power plasma etcher. *J. Phys. Conf. Ser.* **748**, 012017 (2016).

94. Laermer, F. & Schilp, A. Method of anisotropically etching silicon.

95. Etching, B. & Structures, D. A Deep Silicon RIE Primer Bosch Etching of Deep Structures in Silicon. *Power* (2009).

96. Yeom, J., Wu, Y., Selby, J. C. & Shannon, M. A. Maximum achievable aspect ratio in deep reactive ion etching of silicon due to aspect ratio dependent transport and the microloading effect. *J. Vac. Sci. Technol. B Microelectron. Nanometer Struct.* **23**, 2319 (2005).

97. de Almeida, F. R., Yamamoto, R. K. & Maciel, H. S. Reactive ion etching of PECVD silicon nitride in SF6 plasma. *J. Nucl. Mater.* **200**, 371–374 (1993).

98. Kastenmeier, B. E. E., Matsuo, P. J., Beulens, J. J. & Oehrlein, G. S. Chemical dry etching of silicon nitride and silicon dioxide using $CF_4/O_2/N_2$ gas mixtures. *J. Vac. Sci. Technol. Vac. Surf. Films* **14**, 2802–2813 (1996).

99. Lindström, J. L. Reactive Ion Etching of Silicon Nitride Deposited by Different Methods in CF[sub 4]/H[sub 2] Plasmas. *J. Electrochem. Soc.* **139**, 317 (1992).

100. Li, Y. X. Selective reactive ion etching of silicon nitride over silicon using CHF3 with N2 addition. *J. Vac. Sci. Technol. B Microelectron. Nanometer Struct.* **13**, 2008 (1995).

101. Kuo, Y. Reactive Ion Etching of PECVD Amorphous Silicon and Silicon Nitride Thin Films with Fluorocarbon Gases. *J. Electrochem. Soc.* **137**, 1235 (1990).

102. Plummer, J. D., Deal, M. D. & Griffin, P. B. *Silicon VLSI technology: fundamentals, practice, and modeling*. (Prentice Hall, 2000).

103. Kelly, P. . & Arnell, R. . Magnetron sputtering: a review of recent developments and applications. *Vacuum* **56**, 159–172 (2000).

104. *Advances in laser materials processing: technology, research and applications*. (CRC Press, 2010).

105. agar scientific. *Diamond wafering blades*.

106. Kuhn, K. *Laser engineering*. (Prentice Hall, 1998).

107. Honsbreg, C. & Bowden, S. Optical Properties of Si. *PV Education* (2018).

108. Rajput, N. S. & Luo, X. FIB Micro-/Nano-fabrication. in *Micromanufacturing Engineering and Technology* 61–80 (Elsevier, 2015). doi:10.1016/B978-0-323-31149-6.00003-7

109. Reyntjens, S. & Puers, R. A review of focused ion beam applications in microsystem technology. *J. Micromech Michroeng* **11**, 287–300 (2001).

110. Bard, A. J. & Faulkner, L. R. *Electrochemical methods: fundamentals and applications*. (Wiley, 2001).

111. Compton, R. G. & Banks, C. E. *Understanding voltammetry*. (Imperial College Press, 2011).

112. Elgrishi, N. *et al.* A Practical Beginner's Guide to Cyclic Voltammetry. *J. Chem. Educ.* **95**, 197–206 (2018).

113. Benck, J. D., Pinaud, B. A., Gorlin, Y. & Jaramillo, T. F. Substrate selection for fundamental studies of electrocatalysts and photoelectrodes: inert potential windows in acidic, neutral, and basic electrolyte. *PloS One* **9**, e107942 (2014).

114. Ranganathan, S., Kuo, T.-C. & McCreery, R. L. Facile Preparation of Active Glassy Carbon Electrodes with Activated Carbon and Organic Solvents. *Anal. Chem.* **71**, 3574–3580 (1999).

115. Shinwari, M. W. *et al.* Microfabricated Reference Electrodes and their Biosensing Applications. *Sensors* **10**, 1679–1715 (2010).

116. *Semiconductor materials and process technology handbook: for very large scale integration (VLSI) and ultra large scale integration (ULSI)*. (Noyes Publications, 1988).

117. Engineering ToolBox. *Evaporation from a Water Surface*. (2004).

118. Microchemicals. *SU-8 3000 Permanent Epoxy Negative Photoresist Processing Guidelines*.

119. Microchemicals. *SU-8 2000 Permanent Epoxy Negative Photoresist Processing Guidelines*.

120. Grabar, K. C., Freeman, R. G., Hommer, M. B. & Natan, M. J. Preparation and Characterization of Au Colloid Monolayers. *Anal. Chem.* **67**, 735–743 (1995).

7 Appendix: MEMS Processing

Photolithography:

Surface Preparation

- Remove organic contaminants: 2 mins in acetone followed by 2 mins in isopropanol. Do not allow wafer drying during transfer between baths. Once done, rise under running DI for 5mins, blow dry with N_2 gun, and place of hot plate at 110^0C or higher for 5-10mins to dry.
- SiN surfaces: surfaces must be hydrophilic through use of plasma ashing. Place in plasma asher under 60W power for ~3mins. For best results, plasma clean while heated from dehydration bake, and spin coat film within 30s of plasma ashing. HDMS primer must be used. Spin coat at 3000rpm for 30s before PR, and while wafer is still hot. If PR is being used for RIE step, place vinyl sticker on the wafer reverse side to prevent scratching of the SiN during spin coating.
- Gold surfaces: No specific surface treatments necessary. Primer may be used. For best results, apply primer/ PR directly after removal from dehydration bake to prevent condensing of water to the surface. The heated substrate also provides improved adhesion.
- SiO_2: no surface treatment necessary. Adhesion is very high.
- Other: If comet structures are visible in resists, surfaces may be cleaned in HCl and H_2O_2 etch. Do not use if gold or other metals are on the surface, they will be attacked.

Spin Coating

- See technical data sheet of each photoresist for spin-speed curves. General parameters used here are listed below.
- Positive Microposit 18XY: Film thickness in microns is given by X.Y for 30s at 3000rpm. 60s coating does not drastically thin the film but may provide improved uniformity. For RIE and electrode etch out, Microposit 1808 was used and a 1um-1.2um film was formed.
- SU-8: 2000.5 series – spin speed varied from 2000-6000 rpm, for 60s. 2005 – Spin speed of 6000 rpm for 60s produced a 1um film. Custom film – 3000rpm for 60s produced a 450nm film. Se spin speed curve in text for details.
- Negative NR-9 1500P resist – 1.1-3.1 µm
- After spin coating, allow wafer to sit for ~3mins before soft bake, to allow evaporation of solvents and prevent cracking

Soft bake

- Microposit 1808: 110 ^{0}C for 1-2min
- SU-8: 60 ^{0}C for 1min, 90 ^{0}C for 1min
- Negative NR-9: 150 ^{0}C, 1-2 mins
- For SiN substrate, higher soft bake temperatures were found to improve adhesion, but resulted in more bubbles and higher surface roughness of the resist. Other substrates did not require specific soft bake parameters

Exposure

- Note that all listed exposures here may be incorrect due to persistent (and changing) errors with the mask aligner, and inconsistent optical power monitor. In general, all photoresists were exposed near the values listed on technical data sheets, with modifications.
- SiN substrate: Increase exposure by 2x to compensate for poor back reflection
- Au substrate: Increase exposure by 1.5x for back reflection issues
- Microposit 1808: Increase exposure by 1.4 times due to thicker than expected film
- SU-8: Increase exposure by 1.5x if poor adhesion is persistent, but this will reduce image resolution (smaller structures than expected). The negative resist is EXTREMELY sensitive to cleanliness of the mask, as transparent mask structures remain. Any contamination, including bubbles within the polymer, results in surface defects in the film.

Post Exposure Bake

- After exposure, wait ~5 mins prior to PEB to allow settling of the resist.
- For lift off and any electrode etch out structures: soak wafers in toluene for 6 mins. This causes the surface resist to swell and become more chemically resistant and provides a slight undercut profile to the resist. Blow dry toluene away and proceed with PEB.
- PEB for 2mins at 120 ^{0}C. Allow wafer cooling after bake.
  - 100 ^{0}C for NR9
- If resist cracking occurs, use tiered baking steps. Pre-bake at 60 ^{0}C for 1 min, followed by 120 ^{0}C for 1 min. All SU-8 films require this ramp up baking.
- Allow complete cooling before proceeding.

Developing

- Microposit: The standard treatment is ~30 s in a 5:1 water: developer 351 solution. For resists soaked in toluene, develop until the structures can be seen, then continue for 2x that amount of time. (~90s)
- SU-8: 500 nm films develop almost instantly. Do not develop longer than 30 s, this will begin to cause dark erosion. 15 s is usually good.
- NR9: 10-20 s, this develops very fast as well
- Agitate the solution slightly during development. Use significantly more volume than the wafer. This is important for large wafers where large amounts of PR is removed, as the solution gets saturated and sees lots of redeposition.

Post-PR Cleaning

- I almost always follow developing with ~30-60 s in the plasma asher to ensure complete removal from the substrate. This is even more important if a primer was used, as they may ‘develop’ a few monolayers of the PR.

PR Removal

- After processing, PR can be removed however the data sheet recommends. Acetone often works well, followed by methanol and IPA. Air plasma cleaning and plasma ashing are also recommended.

Au/ Cr etch

- The gold and chromium etchants are very dangerous and should be handled with care. Follow an appropriate SOP, typically using 2 rinse beakers for the samples. Many SOP's are available with a quick search. See chapter 3 for the specific etchants used in this work.
- Both etchants have a rate of ~50-100 nm/s. For this work the films used are <10 nm for Cr, and <70 nm for gold. Over etching shouldn't be an issue due to high selectivities, however pin holes in masking layers and under cutting can occur. I typically do 15-20 s in each bath.
- Be sure to rinse samples for 5 mins in running water after etching, for improved performance.

Sputtering

- Sputtering was done in the CEDT Torr sputtering system. The general procedure is identical to that given during training.
- Ensure the base vacuum is below 10^{-6} mbar for best film deposition rate. Always clean the shutters before deposition to prevent contamination.
- Ar gas flow rate: 6-7 sccm. It may need to be slightly higher to maintain DC plasma.
- AC power for Cr: 60 W
- DC power for Au: ~400V, ~70-80 mA
- Clean surfaces with AMI and plasma ash for best adhesion.

RIE

- RIE was done using the 320PC in the Tandem Accelerator Building.
- For easiest results, find the folder/files named 'EDSiNxx', where xx is 1 for 1 minute, 15 for 1.5 mins, or 2 for 2 mins. The process is set for the following:
- 6 sccm O_2 flow rate, 2.5 sccm CF_4 flow rate, base chamber pressure of 32 mTorr.
- All other gasses are off.
- RF forward power is 120 W.
- Reflected power should be automatically adjusted to 0 W by the Load/ Tune values (set at 50%, measured to be 55% and 61% respectively)
- These settings results in ~50-60 nm/s etching of SiN, with similar but unmeasured rate to PR and Si.
- A 30 s delay is added before/after etching to stabilize the chamber.
- The process may stall in the first few seconds due to the plasma failing to be maintained. In this case bypass the error and the process may continue fine. You may lose several seconds of etching if this happens. Doing a dry run first can help 'warm up' the system.